

COVER LETTER

The Rector
University of Tartu
4 Jakobi St. , Tartu 51004 ESTONIA

June 12, 2013

Dear sir:

Greetings!

I humbly submit my application as Assistant Professor (Docent) of Robotics at the Institute of Technology, University of Tartu. I bring with me an extensive experience in real-time robot force and motion control, dynamics modeling and identification, and kinematic failure tolerance, with a combined experience from both the academe and the industry. I am currently working as a postdoctoral research fellow at Daegu Gyeongbuk Institute of Science and Technology in South Korea.

Previously, I worked as an Asst. Professor at De La Salle University in Manila, Philippines. I have worked with world renowned robotics professors Oussama Khatib of Stanford University and Anthony Maciejewski of Colorado State University.

The highlights of my research work are presented in the videos below.

1. Master's Degree Work at the National University of Singapore

A. Model-based control of a mobile manipulator: Preliminary result is shown here <http://www.youtube.com/watch?v=JNuZGDBfyd8> and the final video is shown here <http://www.youtube.com/watch?v=NHOjqkqslWg> (please go through this video until the end when the polishing tool is turned on).

B. Compliant motion principle of control: <http://www.youtube.com/watch?v=u8HejzS8DVI> (this work was shown in national television in Singapore)

C. Demo visitors: <http://www.youtube.com/watch?v=Fe-IX8liGtU>

2. Ph D Work at Colorado State University

A. Failure-tolerant motion planning: Guaranteeing task completion in the presence of obstacles and possible joint failures <http://www.youtube.com/watch?v=refYMWjqlko>.

3. Adviser to students at De La Salle University in Manila, Philippines

A. Gold thesis award for my students: Virtual roller coaster appearance on television (I appeared at 6:19 part of the video) http://www.youtube.com/watch?v=0PRE_xHWn7Q.

4. Home project:

A. Tactile sensor/actuator: <http://www.youtube.com/watch?v=VEbfRQJFXsM>.

I am looking forward to hearing from you.

Sincerely yours,



Rodrigo S. Jamisola, Jr., Postdoctoral Research Fellow
Daegu-Gyeongbuk Institute of Science and Technology, South Korea

Rodrigo S. Jamisola Jr.

Curriculum Vitae

Department of Robotics
Daegu-Gyeongbuk
Institute of
Science & Technology
Republic of Korea
☎ +8210-8685-4964
☎ +8253-785-6230
✉ rjamisolajr@dgist.ac.kr



Education

- 10-2011 **Post Doc**, *Daegu-Gyeongbuk Institute of Science & Technology*, Daegu, South Korea.
Present
 - *Research*: Rehabilitation Robotics
 - *Advisor*: Prof. Pyung Hun Chang, Graduate School Director
- 05-2008 **Ph.D.**, *De La Salle University - Manila*, Manila, Philippines.
- 12-2009
 - *Dissertation*: "Identifying Mass, Center of Mass, and Moment of Inertia through Natural Oscillations for Full-Dynamics Control of Robot Manipulators"
 - *Advisor*: Prof. Elmer P. Dadios, University Fellow
- 08-2001 **M.Sc.**, *Colorado State University*, Colorado, U.S.A.
- 12-2006
 - *Thesis/Dissertation*: "Failure-Tolerant Path Planning for Kinematically Redundant Robots"
 - *Advisor*: Prof. Anthony A. Maciejewski, IEEE Fellow
- 01-1997 **M.Eng.**, *National University of Singapore*, Singapore.
- 08-2001
 - *Thesis*: "Full-Dynamics Identification and Control of PUMA 560 and Mitsubishi PA-10 Robots"
 - *Advisor*: Prof. Marcelo H. Ang, Jr., Director, Center for Intelligent Products and Manufacturing Systems
- 06-1988 **B.Sc.**, *University of the Philippines, Diliman*, Quezon City, Philippines.
- 10-1993
 - *Full Scholar*: Toyota Motor Philippines Foundation

Research and Teaching Experience

- 10-2011 **Post Doctoral Research Fellow**, *Department of Robotics, Daegu-Gyeongbuk Institute of Science & Technology*, Daegu, South Korea.
present
 - Lead efforts to publish high quality research in high-impact journals on dual-arm robots, humanoids, and surgical and rehabilitation robots
 - Linux-based, real-time C/C++ simultaneous control of two industrial robots, as a dual-arm manipulator
 - SimStudio and RoboticsLab simulation platform in 3D OpenGL, with Matlab and Mathematica
 - Impedance control-based upper limb and fingers rehabilitation, integrated with brain computer interface
 - Successfully derived a non-inverse projection matrix for task prioritization for redundant robots
 - Devised a new method, modified from previous, to control combined manipulators as a single manipulator
 - To propose government-funded project on exoskeleton as elderly aid for walking independently
 - To develop control of 4-arm Cyber Knife for radiation treatment of cancerous organs and tissues
 - Conducts seminars and lectures inside and outside of institute to increase contacts and learning
 - 1 published work, 1 paper with minor revision, 2 papers under review, 1 paper under revision
- 05-2011 **R & D Manager**, *Toyota Motor Philippines*, Sta. Rosa, Laguna, Philippines.
- 10-2011 Pioneered and supervised a Research and Development team to develop in-house mechatronics and robotics systems to support manufacturing processes
 - Created and demonstrated capability of two AUVs for automatic transport of car body parts
 - Prototyped in-house trolley locks, eliminated equipment orders from overseas, resulted to huge savings
 - Developed automatic car body-type inspection by web camera using OpenCV libraries
 - Evaluated design and provided consultation for motorized manipulator arm to assist heavy load lifting
 - Mapped plans to improve existing automation solutions and to develop in-house manipulators and robots
 - Conducted seminars to improve skills of engineers in C/C++ programming and Open Software libraries
- 05-2008 **Asst. Professor**, *De La Salle University - Manila*, Manila, Philippines.
- 05-2011 Established strong collaboration with ERDT, DOST, University of the Philippines in Diliman and leading hospitals for medically-oriented robotics and intelligent systems research
 - Maximized resources for research inside and outside of university in specialized area and interdisciplinary
 - Graduate and undergraduate lectures on engineering mathematics, numerical methods, and programming
 - Supervised research on tactile sensing, exoskeleton, robot-assisted surgery, and virtual reality in ODE
 - Awarded, Best Thesis for supervised undergraduate thesis on virtual reality roller coaster ride
 - Actively participate in technopreneurship programs to advance technological opportunities for the country
 - Restarted Ph D program and successfully finished in 1.5 years with full teaching and research loads
 - Awarded, Best Dissertation in Miroelectronics/Mechatronics by Dept. of Science and Technology
 - Published 4 journal articles and 9 conference papers, 2 completed projects, and 4 on-going proposals

- 05-2006 **Guidance, Control, and Navigation Engineer**, *L-3 Communications*, California, U.S.A..
- 02-2008 Developed, customized, and commissioned control software for dynamic positioning of vessels
- Created C/C++ programs based on Windows to automatically control thrusters with GPS feedback
 - Customized control software based on sensor feedback, and vessel steering and power capability
 - Developed numerical methods to provide feedback based on vessel trim and tank fluid capacity
 - Identified cause of errors during on-board commissioning and directed resolution implementations
 - Lead efforts to establish satellite office and DP training schools in Singapore and in the Philippines
 - Travelled to worldwide site locations around 60% of total working time
- 08-2001 **Ph. D. Student/Research Assistant**, *Colorado State University*, Colorado, U.S.A..
- 05-2006 Developed solutions for kinematic failure tolerance for redundant manipulators
- Received Ph D offer after showing demonstration video of research work in Singapore
 - Joined Purdue University Prof. Anthony Maciejewski to transfer to Colorado State University
 - Solved 16-year-old problem in kinematic failure tolerance with obstacles and optimized workspace
 - Used Matlab, C/C++ with multi-threading, and OpenGL for simulation and control implementation
 - Collaborated with Prof. Rodney Roberts from Florida State University, and was a co-adviser
 - Created physical demonstration of proposed robot capability for laboratory visitors
 - Part I of Dissertation, solved: failure tolerance with obstacles in IEEE Transactions on Robotics
 - Part II of Dissertation, solved: optimum failure-tolerant workspace but cannot prove mathematically
 - Failed in the Final Defence, mainly caused by disagreement on research direction with adviser
 - PA-10 robot video: <http://www.youtube.com/watch?v=refYMWjqIko>
 - Planar robot video: <http://www.youtube.com/watch?v=83AgzToiZyo>
 - Published 2 journal articles and 4 conference papers
- 08-1999 **Robotics Research Engineer**, *Singapore Institute of Manufacturing Technology*, Singapore.
- 08-2001 Lead group of researchers and students in implementing Operational Space Formulation for mobile manipulators at 10 ± 3 N controlled normal force with random disturbance
- Master's Degree work received government funds for further research in SIMTech (formerly Gintic)
 - Synthesized and implemented control strategies in Operational Space Formulation with a research group
 - Prof. Oussama Khatib of Stanford University was a project consultant who visited every 2 months
 - Used analytical techniques to identify and validate dynamics parameters of PUMA and Mitsubishi PA-10
 - Invoked compliant motion for simultaneous control of force and motion of PUMA end-effector
 - Mobile base Nomad XR4000 was moved manually via joystick and was treated as system disturbance
 - Used Matlab, C/C++ with multi-threading, and OpenGL for simulation and control implementation
 - Control runs at 2ms under WindowsNT with RTX real-time kernel and LabWindows GUI
 - Mobile manipulator video: <http://www.youtube.com/watch?v=JNuZGDBfyd8>
 - Compliant motion video: <http://www.youtube.com/watch?v=u8HejzS8DVI>
 - Demo with world-famous professors: <http://www.youtube.com/watch?v=Fe-IX8liGtU>
 - Created machine vision software to identify marks for pipe measuring at Singapore shipyard
 - Published 1 journal article and 2 conference papers
- 08-1997 **Master of Engineering Scholar**, *National University of Singapore*, Singapore.
- 08-1999 Identified dynamics parameters and controlled PUMA 650 and Mitsubishi PA-10 robots
- Finished all Master's degree requirements in two year; plus 1.5 years of external thesis review process
 - Simulated in Matlab and C program to verify the accuracy of full dynamics model
 - Coded Mathematica symbolic program to create lumped dynamics model of two industrial robots
 - Identified lumped dynamics parameters and friction of the PUMA 560 and PA-10 robots
 - Controlled PUMA 560 using QNX real-time OS every 10 ms computation cycle
 - Published 1 conference paper

Honors and Awards

- 2010 **Outstanding Dissertation Award**, *Department of Science and Technology*, Philippines.
- 2005 **General Technical Clarity Award**, *Information Science & Technology Colloquium*, Colorado State University, Colorado, U.S.A..
- 2001,2002,2003 **Listed**, *Marquis Who's Who in Science and Engineering*, U.S.A..
- 2001-2006 **Research Assistantship**, *Colorado State University*, Fort Collins, Colorado, U.S.A..
- 1997-1999 **Full Research Scholarship**, *National University of Singapore*, Singapore.
- 1995 **4th Highest Place Nationwide**, *Registration for Mechanical Engineers*, Professional Regulation Commission, Philippines.
- 1991-1993 **Full Scholar**, *Toyota Motor Philippines Foundation*, University of the Philippines, Diliman, Philippines.

Journal Publications

- 2012 **J. Lee, P. H. Chang, R. S. Jamisola, Jr.**, "*Relative Impedance Control for Dual-Arm Robots Performing Asymmetric Bimanual Tasks*", Accepted for publication on May 11, 2013 to the IEEE Transactions on Industrial Electronics.
- 2010 **R. S. Jamisola, Jr.**, "*Optimization of Failure-Tolerant Workspaces for Redundant Manipulators*", Philippine Science Letters, vol. 3, no. 1, Apr. 2010, pp. 66-75.
- 2010 **R. S. Jamisola, Jr., E. P. Dadios**, "*Experimental Identification of Manipulator Dynamics through the Minimization of its Natural Oscillations*", Journal of Advanced Computational Intelligence and Intelligent Informatics, Jan. 2010, vol. 14, no. 1, pp. 39-45.
- 2009 **R. S. Jamisola, Jr., E. P. Dadios, M. H. Ang, Jr.**, "*Using Metaheuristic Computations to Find the Minimum-Norm-Residual Solution to Linear Systems of Equations*", Philippine Computing Journal, vol. 4, no. 2, Dec. 2009, pp. 1-9.
- 2009 **R. S. Jamisola, Jr., E. P. Dadios, M. H. Ang, Jr.**, "*Dynamics Parameters Identification of Rigid-Body Manipulators through Natural Oscillations*", Philippine Computing Journal, vol. 4, no. 2, Dec. 2009, pp. 10-18.
- 2006 **R. S. Jamisola, Jr., A. A. Maciejewski, R. G. Roberts**, "*Failure-Tolerant Path Planning for Kinematically Redundant Manipulators Anticipating Locked-Joint Failures*", IEEE Transactions on Robotics, vol. 22, no. 4, Aug. 2006, pp. 603-612.
- 2005 **R. S. Jamisola, Jr., D. N. Oetomo, M. H. Ang, Jr., O. Khatib, T. M. Lim, S. Y. Lim**, "*Compliant Motion using a Mobile Manipulator: An Operational Space Formulation Approach to Aircraft Canopy Polishing*", RSJ Advanced Robotics, June 2005, vol. 19, no. 5, pp. 613-634.

Conference Publications

- 2013 **J. Lee, P. H. Chang, R. S. Jamisola, Jr.**, "*Relative Task Prioritization for Dual-Arm Manipulators with Multiple, Conflicting Tasks: Derivation and Experiments*", 2013 IEEE International Conference in Robotics and Automation, 6-10 May 2013, Karlsruhe, Germany.
- 2012 **R. S. Jamisola, Jr., P. H. Chang, J. Lee**, "*Guaranteeing Task Prioritization for Redundant Robots Given Maximum Number of Tasks and Singularities*", 2012 IEEE Region 10 Conference, 19-22 Nov. 2012, Cebu City, Philippines.
- 2011 **R. S. Jamisola, Jr., R. G. Baldovino**, "*A Study on the State of Powered-Exoskeleton Design for Lower Extremities*", 5th International Conference on Humanoid, Nanotechnology, Information Technology, Communication and Control, Environment, and Management 2009 (HNICEM 2009), Mar. 10-12 2011, Manila, Philippines.
- 2011 **Montesines-Nagayo, A. A., R. S. Jamisola, Jr.**, "*A Survey on Current Developments in Tactile Sensing Technology for Robotic Surgery and other Biomedical Applications*", 5th International Conference on Humanoid, Nanotechnology, Information Technology, Communication and Control, Environment, and Management 2009 (HNICEM 2009), Mar. 10-12 2011, Manila, Philippines.
- 2009 **R. S. Jamisola, Jr., E. P. Dadios**, "*A Novel Dynamics Identification Method for Rigid-Body Manipulators*", 13th International Conference on Mechatronics Technology (ICMT 2009), 20-23 Oct. 2009, Cebu City, Philippines.
- 2009 **R. S. Jamisola, Jr., E. P. Dadios**, "*Identifying Moments of Inertia Parameters for Rigid-Body Manipulators*", 13th International Conference on Mechatronics Technology (ICMT 2009), 20-23 Oct. 2009, Cebu City, Philippines.
- 2009 **R. S. Jamisola, Jr., E. P. Dadios**, "*A Probabilistic Computation of Artificial Neural Network and Genetic Algorithm in Finding the Minimum-Norm-Residual Solution to Linear Systems of Equations*", 4th International Conference on Humanoid, Nanotechnology, Information Technology, Communication and Control, Environment, and Management 2009 (HNICEM 2009), Mar. 12-15 2009, Manila, Philippines.
- 2009 **R. S. Jamisola, Jr., E. P. Dadios**, "*Full Dynamics Identification of Multi-Link Inverted Pendulum: Analysis and Implementation*", 4th International Conference on Humanoid, Nanotechnology, Information Technology, Communication and Control, Environment, and Management 2009 (HNICEM 2009), Mar. 12-15 2009, Manila, Philippines.
- 2009 **M. A. S. Briones, L. S. Cruz, Jr., J. S. Go, A. L. S. Mauhay, R. S. Jamisola, Jr.**, "*High Resolution Haptic Sensing System in Virtual Reality*", National Electrical, Electronics, and Computing Conference 2009, 9-11 December 2009, Manila, Philippines.
- 2008 **R. S. Jamisola, Jr., E. P. Dadios, M. H. Ang, Jr.**, "*A Probabilistic Approach in Computing Artificial Neural Network and Genetic Algorithm for Linear Systems of Equations*", 1st AUN/SEED-Net Regional Conference in Manufacturing Engineering, Nov. 24-25, 2008, Manila, Philippines.

- 2008 **R. S. Jamisola, Jr., E. P. Dadios, M. H. Ang, Jr.,** "A Comparison between Probabilistic Artificial Neural Network and Simulated Annealing in Finding the Minimum-Norm Residual Solution to Linear Systems of Equations", 1st AUN/SEED-Net Regional Conference in Manufacturing Engineering, Nov. 24-25, 2008, Manila, Philippines.
- 2007 **R. G. Roberts, R. S. Jamisola, Jr., and A. A. Maciejewski,** "Identifying the Failure-Tolerant Workspace Boundaries of a Kinematically Redundant Manipulator", 2007 IEEE International Conference on Robotics and Automation, Roma, Italy, 10-14 April 2007, pp. 4517-4523.
- 2004 **R. S. Jamisola, Jr., A. A. Maciejewski, R. G. Roberts,** "Failure-Tolerant Path Planning for the PA-10 Robot Operating Amongst Obstacles", IEEE 2004 International Conference on Robotics and Automation (ICRA 2004), April 26 - May 1, 2004, New Orleans, Louisiana, vol. 5, pp. 4995-5000.
- 2004 **R. S. Jamisola, Jr., A. A. Maciejewski, R. G. Roberts,** "A Computational Feasibility Study of Failure-Tolerant Path Planning", Proceedings 10th International Topical Meeting on Robotics and Remote Systems for Hazardous Environments, March 28 - 31, 2004, Gainesville, Florida, pp. 233-239.
- 2003 **R. S. Jamisola, Jr., A. A. Maciejewski, R. G. Roberts,** "A Path Planning Strategy for Kinetically Redundant Manipulators Anticipating Joint Failures in the Presence of Obstacles", 2003 IEEE/RSJ International Conference on Intelligent Robots and Systems (IROS 2003), Oct 27-31, 2003, Las Vegas, Nevada, vol. 1, pp. 142-148.
- 2002 **R. Jamisola, M.H. Ang, Jr., D. Oetomo, O. Khatib, T.M. Lim, S.Y. Lim,** "The Operational Space Formulation Implementation to Canopy Polishing Using a Mobile Manipulator", Proceedings 2002 IEEE International Conference on Robotics and Automation (ICRA 2002), May 11-15, 2002, Washington, D.C., pp. 400-405.
- 2002 **D. Oetomo, M.H. Ang, Jr., R. Jamisola, O. Khatib,** "Integration of Torque Controlled Arm with Velocity Controlled Base for Mobile Manipulation", Fourteenth CISM-IFTOMM Symposium on Robotics RoManSy 2002, Jul. 1-4, 2002, Udine, Italy.
- 1999 **R. Jamisola, M.H. Ang, Jr., T.M. Lim, O. Khatib, S.Y. Lim,** "Dynamics Identification and Control of an Industrial Robot", The 9th International Conference on Advanced Robotics 1999 (1999 ICAR), Oct. 25-27, 1999, Tokyo, Japan, pp. 323-328.

Research Projects

- 2009 **Numerical Computations of Humanoid Robot Dynamics,** *University Research Coordination Office, DLSU - Manila*, Status: Completed Project, Cost: PHP 83k.
- 2010 **Studying the Primitives of Virtual Reality Interactive Environment: Rendering, Tactile Sensing, and Exoskeleton,** *University Research Coordination Office, DLSU - Manila*, Status: Completed Project, Cost: PHP 180k.
- 2010 **Robotics Telesurgery Operation,** *Engineering Research for Development and Technology, Department of Science and Technology*, Status: Final proposal evaluation, Cost: PHP 5.5M.
- 2010 **Using Drones to Build Real-Time Simulated Reconnaissance Map for the Philippine Military,** *Engineering Research for Development and Technology, Department of Science and Technology*, Status: For panel evaluation, Cost: PHP 7.5M.
- 2011 **Exoskeleton to Assist Persons with Walking Disability,** *University of the Philippines Enterprise Program for Technopreneurship*, Status: Business coaching, Cost: To be determined.
- 2011 **Building A Mathematical Model to Diagnose Cyber-Gaming Addiction Among Youngsters,** *University Research Coordination Office, DLSU - Manila*, Status: Approved, Cost: PHP 300k.

Affiliations

IEEE, *Member.*

ASME, *Member.*

Eta Kappa Nu Honor Society, *Member.*

University of the Philippines Epsilon Chi Fraternity, *Alumnus Member.*

Places Lived and Languages Used

Philippines, *by birth, Cebuano (fluent), Filipino (fluent).*

Singapore, *5 years, English (fluent).*

U.S.A., *5 years, English (fluent).*

South Korea, *1 year (currently living), Korean (reading and writing, but minimally spoken).*

References

Anthony A. Maciejewski.

Professor and Department Chair
Department of Electrical and Computer Engineering, Colorado State University, U.S.A.
Email: aam@colostate.edu
Phone: +1-970-491-6600

Marcelo H. Ang, Jr..

Professor and Associate Dean
Department of Mechanical Engineering, National University of Singapore, Singapore
Email: mpeangh@nus.edu.sg
Phone: +65-6516-2555

Oussama Khatib.

Professor
Department of Computer Science, Stanford University, U.S.A.
Email: okhatib@cs.stanford.edu
Phone: +1-650-723-9753

Additional Relevant Information

■ Lectures

No	Semester / Year	Course Name	Hour / Week	Remark
1	1 st Trimester / SY 2008-2009	Computational Numerical Methods	3 Hours / Week	3 Sections Undergraduate
2	1 st Trimester / SY 2008-2009	C Programming (Lecture)	3 Hours / Week	1 Section Undergraduate
3	1 st Trimester / SY 2008-2009	C Programming (Laboratory)	3 Hours / Week	1 Section Undergraduate
4	2 nd Trimester / SY 2008-2009	Discrete Mathematics	3 Hours / Week	2 Sections Undergraduate
5	2 nd Trimester / SY 2008-2009	C Programming (Lecture)	3 Hours / Week	1 Section Undergraduate
6	3 rd Trimester / SY 2008-2009	Discrete Signal Processing	3 Hours / Week	2 Sections Undergraduate
7	3 rd Trimester / SY 2008-2009	Computer Engineering Mathematics	3 Hours / Week	1 Section Undergraduate
8	1 st Trimester / SY 2009-2010	Computational Numerical Methods	3 Hours / Week	2 Sections Undergraduate
9	1 st Trimester / SY 2009-2010	C Programming (Laboratory)	3 Hours / Week	1 Section Undergraduate
10	2 nd Trimester / SY 2009-2010	Discrete Mathematics	3 Hours / Week	2 Sections Undergraduate
11	2 nd Trimester / SY 2009-2010	Introduction to Robotics I	3 Hours / Week	1 Section Masters Degree
12	3 rd Trimester / SY 2009-2010	Vector Analysis	3 Hours / Week	1 Section Undergraduate
13	3 rd Trimester / SY 2009-2010	Introduction to Robotics I	3 Hours / Week	1 Section Masters/ Ph D
14	3 rd Trimester / SY 2009-2010	Introduction to Robotics II	3 Hours / Week	1 Section Masters/ Ph D
15	1 st Trimester / SY 2010-2011	Engineering Economy	3 Hours / Week	2 Sections Undergraduate
16	1 st Trimester / SY 2010-2011	Force and Motion Control of Robot Manipulators	3 Hours / Week	1 Section Masters/ Ph D
17	2 nd Trimester / SY 2010-2011	Computational Numerical Methods	3 Hours / Week	1 Section Undergraduate
18	2 nd Trimester / SY 2010-2011	Computational Optimization	3 Hours / Week	1 Section Masters/ Ph D
19	2 nd Trimester / SY 2010-2011	Computer Graphics for Engineers	3 Hours / Week	1 Section Masters/ Ph D

20	3rd Trimester / SY 2010-2011	Vector Analysis	3 Hours / Week	2 Sections Undergraduate
21	3rd Trimester / SY 2010-2011	Robot Motion Planning	3 Hours / Week	1 Section Masters/ Ph D

■ Student Advisees

1	Gold Thesis Award from De La Salle University – Manila, Undergraduate Thesis “Virtual Reality Roller Coaster” by Paolo Barlis, Terence Go, Alvin Morelos, and Ron Jacob Yambot.
2	Renann Baldovino, “Exoskeleton to Help People with Walking Disability,” Master of Science Thesis
3	Goeffrey Abulencia, “Automation of Rice Production,” Master of Science Thesis
4	Analene Montesines-Nagayo, “Tactile Sensing on Biomedical Applications,” Ph D Dissertation
5	Medi Nasar, “A Mathematical Model to Diagnose Cybergaming Addiction,” Ph D Dissertation

Lecture Plan

Assume 1.5 hours of lecture

5 to 8 minutes: check student attendance

5 minutes review of the previous lesson

I. Overview of the lecture (8 minutes)

- A. How this topic connects with the previous topic**
- B. Why this topic is important to students now and how it will be useful in their future**
- C. Some practical applications of the topic, including technological advances if applicable**

II. How to present the subject matter (1 hour)

- A. Interactive PowerPoint slides**
- B. Professor will highlight important items in the slide by a highlighter or underline in the PowerPoint slide**
- C. Discussion has to be lively, and not monotonous**
- D. Discussion has to be interactive with the Professor asking thought-provoking questions related to the subject matter**
- E. Students are encouraged to participate in the class discussion and interact with the Professor and their fellow students**
- F. Professor has to use the white board to show derivation of very important equations, so students can follow, instead of putting everything in the PowerPoint slides.**
- G. Professor has to write on whiteboard or on the slides to emphasize very important points**
- H. Exercises and seatworks are encouraged once every two weeks for a 3-unit subject.**
- I. Students should be asked frequently during lectures if they have any questions, to encourage them to ask questions.**

III. Summarize the discussion, and discuss plans for the next meeting. (8 minutes)

Relative Impedance Control for Dual-Arm Robots Performing Asymmetric Bimanual Tasks

Jinoh Lee, *Member, IEEE*, Pyung Hun Chang, *Member, IEEE*, and Rodrigo S. Jamisola, Jr., *Member, IEEE*

Abstract—This paper presents a method of implementing impedance control (with inertia, damping, and stiffness terms) on a dual-arm system by using the relative Jacobian technique. The proposed method significantly simplifies the control implementation because the dual-arm is treated as a single manipulator, whose end-effector motion is defined by the relative motion between the two end-effectors. As a result, task description becomes simpler and more intuitive when specifying the desired impedance and the desired trajectories. This is the basis for the relative impedance control. In addition, the use of time-delay estimation enhances ease of implementation of our proposed method to a physical system, which would have been otherwise a very tedious and complicated process.

Index Terms—dual arm, relative Jacobian, impedance control, time-delay estimation, ideal-velocity feedback, asymmetric bimanual task

I. INTRODUCTION

Dual-arm robots provide a platform for implementing humanly intuitive tasks. And possibly, straightforwardly replace humans in performing some of their work. These tasks may involve high technology, e.g., outer-space assembly and repair, or domestic work, e.g., assisting the elderly in the household chores. The biggest challenge in dual arms, however, is the complexity of manipulation. Thus, it is advantageous to adopt a strategy to address this complexity, and at the same time accommodate human intuitiveness in the task requirements.

This work presents a method of implementing impedance control on a dual-arm system that is controlled as a single manipulator. It allows an easier coordination of interaction between the two arms. This single controller was possible via a relative Jacobian [1], [2], which maps the joint velocities of the two arms to the relative motion between their end-effectors. Thus the name relative impedance control. The relative Jacobian is derived by combining the individual Jacobians of each arm. From the control perspective, it creates

an effective single arm with kinematic redundancy, which contributes to the simplification of control strategy. The use of time-delay estimation (TDE) [3]–[6] further simplifies our implementation by estimating the robot dynamics from the imprecise dynamics information of the dual arm.

Dual arms are inherently designed to interact with each other, and in some cases, with their environment. Many studies on such interaction used impedance control [7] that are internal (between manipulators) [8]–[10] and/or external (between manipulator and environment) [8], [10]. In this work, relative impedance control refers to impedance control that is expressed in relative reference frames, which can be internal or external.

Bimanual tasks can be classified as symmetric or asymmetric [11], [12]. In symmetric bimanual tasks, both arms play the same role: in an in-phase manner, e.g., lifting a single object with both arms [9], [10], [13]–[15]; or in an out-of-phase manner, e.g., rope climbing [11]. In asymmetric bimanual tasks (ABTs), each arm performs a different role but each is necessary to achieve a desired task, e.g., dealing cards [11], writing a handy note [16], part-mating or assembly [17], [18], and opening a jar [19]. It has been experimentally shown that bimanual task coordination in humans activates a different part of the brain as compared to unimanual task movements [20], [21]. In this work, the ABT is performed with the right hand writing a circle on a plate attached to the left hand. Recent studies on dual-arm/multiple robots include [22]–[24] and bio-inspired robots and control strategies include [25]–[37].

The difference of our work compared to previous studies of impedance control on dual-arm systems is stated here. The work of [19] used two anthropomorphic dual-arms of Justin to unscrew a can. It used impedance control without the inertia term and did not use a relative Jacobian. In [38], two six degrees-of-freedom (DOFs) Kuka robots that held an egg used adaptive force/motion control and did not use a relative Jacobian. Coordination of n -cooperating manipulators were discussed in [9] with full impedance control but used no relative Jacobian. Full impedance control of two 6-DOFs manipulators were shown in [10] but did not use a relative Jacobian. Two 2-DOFs SCARA robots with full impedance control were used in [8] but the did not use a relative Jacobian. An SCARA and a PUMA 560 robots with full impedance control were used in [39] but no relative Jacobian was used. A previous study that is closest to our work is [40], which used impedance control with relative Jacobian. However, the impedance control used was only a function of stiffness term, without inertia and damping terms. In addition, it did not use any cancellation of the dynamics of the system. There have

Manuscript received September 29, 2012. Accepted for publication May 11, 2013.

Copyright © 2013 IEEE. Personal use of this material is permitted. However, permission to use this material for any other purposes must be obtained from the IEEE by sending a request to pubs-permissions@ieee.org.

J. Lee is with the Department of Advanced Robotics, Istituto Italiano di Tecnologia, Via Morego 30, 16163, Genoa, Italy (e-mail: jinoh.lee@iit.it).

P. H. Chang was with the Division of Mechanical Engineering, Korea Advanced Institute of Science and Technology (KAIST). He is now with the Department of Robotics Engineering, Daegu Gyeongbuk Institute of Science and Technology (DGIST), 50-1 Sang-ri, Hyeonpung-myeon, Dalseong-gun, Daegu, 711-873, South Korea (e-mail: phchang@dgist.ac.kr).

R. S. Jamisola, Jr. is with Department of Robotics Engineering, DGIST, 50-1 Sang-ri, Hyeonpung-myeon, Dalseong-gun, Daegu, 711-873, South Korea (phone: +82-53-785-6230; fax: +82-53-785-6209; e-mail: rjamisola-lajr@dgist.ac.kr).

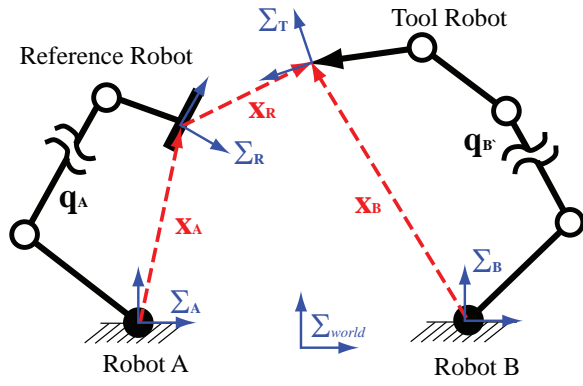


Fig. 1: A schematic diagram of a dual arm with robot A (reference robot) and robot B (tool robot). We used the following notation: \mathbf{q}_A – joint angles of robot A ; \mathbf{q}_B – joint angles of robot B ; \mathbf{x}_R – relative position and orientation vector with respect to Σ_R ; Σ_{world} – world frame; Σ_A – base frame of robot A ; Σ_B – base frame of robot B ; Σ_R – relative reference frame (located at robot A end-effector); and Σ_T – tool frame (located at robot B end-effector). The position and orientation of robot A is \mathbf{x}_A , and for robot B is \mathbf{x}_B .

been comparable dual-arm controls using disturbance observer, which is equivalent to TDE [41]. Studies in dual-arms with disturbance observer and impedance control include [42]–[46]. However, all of these previous studies did not use relative Jacobian.

The contribution of this paper is on the proposition of relative impedance control for dual-arm systems to perform ABTs by simultaneously using relative Jacobian [1], [2] and TDE [3], [4] with ideal-velocity feedback (IVF) [47]. The use of relative Jacobian allows a simpler and more intuitive way of implementing impedance control (with inertia, damping, and stiffness terms) on a dual arm that is controlled as a single manipulator. Through our proposed method, only a single set of desired impedance and desired trajectories is used for the two end-effectors. The use of TDE with IVF provides a convenient way of dynamics cancellation with minimal knowledge of the dynamics parameters of the dual-arm.

This paper proceeds as follows. Section II presents the theoretical foundation of this work, which includes the relative impedance control formulation. Section III shows the description of our experimental setup and experimental results of a bimanual writing task. Section IV presents our conclusion. And lastly, Appendix A discusses the stability analysis of our proposed controller.

II. THEORETICAL FOUNDATIONS

The schematic diagram of our dual-arm robot performing ABT is shown in Fig. 1 with robot A , the reference robot, and robot B , the tool robot. The reference frames are defined as follows: tool frame, Σ_T , located at robot B end-effector; relative reference frame, Σ_R , located at robot A end-effector; robot A base frame, Σ_A ; robot B base frame, Σ_B ; and world frame, Σ_{world} . The relative position and orientation vector,

$\mathbf{x}_R \in \mathbb{R}^{n_R}$, defines the position and orientation of Σ_T with respect to Σ_R . The symbol n_R denotes the task space DOFs. Also shown in the figure are the position and orientation of robot A end-effector, denoted \mathbf{x}_A , and of robot B end-effector, denoted \mathbf{x}_B .

A. The Relative Jacobian

Kinematically, the relative velocity vector, $\dot{\mathbf{x}}_R \in \mathbb{R}^{n_R}$, is derived through the action of the relative Jacobian, $\mathbf{J}_R \in \mathbb{R}^{n_R \times n_T}$, on the joint space vector $\dot{\mathbf{q}} \in \mathbb{R}^{n_T} = [\dot{\mathbf{q}}_A^T \ \dot{\mathbf{q}}_B^T]^T$, that is,

$$\dot{\mathbf{x}}_R = \mathbf{J}_R \dot{\mathbf{q}}. \quad (1)$$

The symbols $\dot{\mathbf{q}}_A \in \mathbb{R}^{n_A}$ and $\dot{\mathbf{q}}_B \in \mathbb{R}^{n_B}$ represent the joint velocities of robots A and B , respectively, and $n_T = n_A + n_B$, where n_A and n_B are the DOFs of the respective robots. (From hereon, the subscripts A and B would refer to robot A and robot B , respectively.) This allows users to directly design the relative trajectory between the two end-effectors so that implementing ABT becomes particularly simple. The expression of \mathbf{J}_R can be derived from the individual Jacobians of each robot, that is,

$$\dot{\mathbf{x}}_R = \dot{\mathbf{x}}_B - \dot{\mathbf{x}}_A, \quad (2)$$

such that,

$$\dot{\mathbf{x}}_R = \begin{bmatrix} -\mathbf{J}_A & \mathbf{J}_B \end{bmatrix} \begin{bmatrix} \dot{\mathbf{q}}_A^T \\ \dot{\mathbf{q}}_B^T \end{bmatrix}^T, \quad (3)$$

such that $\mathbf{J}_R = [-\mathbf{J}_A \ \mathbf{J}_B]$ is the relative Jacobian with respect to the inertial reference frame. Similar to the derivation above is shown in [48]. However, in this paper, the expression of \mathbf{J}_R used is the same as the expression shown in [2], [49].

B. Relative Impedance Control

The relative acceleration vector in the task space, $\ddot{\mathbf{x}}_R$, can be expressed as $\ddot{\mathbf{x}}_R = \mathbf{J}_R \ddot{\mathbf{q}} + \dot{\mathbf{J}}_R \dot{\mathbf{q}}$, where $\dot{\mathbf{J}}_R$ denotes the derivative of \mathbf{J}_R , and $\ddot{\mathbf{q}}$ denotes the joint acceleration. The inverse kinematic solution is [50]

$$\ddot{\mathbf{q}} = \mathbf{J}_R^+ (\ddot{\mathbf{x}}_R - \dot{\mathbf{J}}_R \dot{\mathbf{q}}) + (\mathbf{I} - \mathbf{J}_R^+ \mathbf{J}_R) \boldsymbol{\nu}, \quad (4)$$

where $\mathbf{I} \in \mathbb{R}^{n_T \times n_T}$ is an identity matrix, and $\boldsymbol{\nu} \in \mathbb{R}^{n_T}$ is an arbitrary joint-space acceleration vector. In this paper, we use $\boldsymbol{\nu} = \mathbf{0}$, which means that the solution achieves the minimum norm acceleration.

The complete dynamics of the entire dual-arm system is expressed as a combined dynamics of robot A and robot B , that is,

$$\boldsymbol{\tau} = \mathbf{M}(\mathbf{q}) \ddot{\mathbf{q}} + \mathbf{c}(\mathbf{q}, \dot{\mathbf{q}}) + \mathbf{g}(\mathbf{q}) + \mathbf{f}(\mathbf{q}, \dot{\mathbf{q}}) + \boldsymbol{\tau}_d + \boldsymbol{\tau}_e, \quad (5)$$

where $\boldsymbol{\tau}_u = [\boldsymbol{\tau}_A^T \ \boldsymbol{\tau}_B^T]^T \in \mathbb{R}^{n_T}$ denotes the joint torque vector; $\mathbf{M}(\mathbf{q}) = \text{diag}(\mathbf{M}_A(\mathbf{q}), \mathbf{M}_B(\mathbf{q})) \in \mathbb{R}^{n_T \times n_T}$ denotes the block diagonal of combined inertia matrices; $\mathbf{c}(\mathbf{q}, \dot{\mathbf{q}}) = [\mathbf{c}_A(\mathbf{q}, \dot{\mathbf{q}})^T \ \mathbf{c}_B(\mathbf{q}, \dot{\mathbf{q}})^T]^T \in \mathbb{R}^{n_T}$ denotes combined torques of Coriolis and centrifugal forces; $\mathbf{g}(\mathbf{q}) = [\mathbf{g}_A(\mathbf{q})^T \ \mathbf{g}_B(\mathbf{q})^T]^T \in \mathbb{R}^{n_T}$ denotes combined torques of gravitational forces; $\mathbf{f}(\mathbf{q}, \dot{\mathbf{q}}) = [\mathbf{f}_A(\mathbf{q}, \dot{\mathbf{q}})^T \ \mathbf{f}_B(\mathbf{q}, \dot{\mathbf{q}})^T]^T \in \mathbb{R}^{n_T}$ denotes combined torques of Coulomb and viscous

friction, and stiction; $\tau_d \in \mathbb{R}^{n_T}$ denotes torques due to disturbances; and $\tau_e \in \mathbb{R}^{n_T}$ denotes torques due to environmental contact forces.

The target dynamics of a physical system, such as the above equation, can be achieved through the desired impedance equation [7]. In this work, we modify the desired impedance equation such that it can accommodate the relative motion between the two end-effectors of the dual-arm, the internal impedance between them, and the (external) impedances for each end-effector. The defined relationships are expressed in a formulation corresponding to an equivalent single manipulator,

$$-\mathbf{f}_R = \mathbf{M}_{Rd}(\ddot{\mathbf{x}}_{Rd} - \ddot{\mathbf{x}}_R) + \mathbf{B}_{Rd}(\dot{\mathbf{x}}_{Rd} - \dot{\mathbf{x}}_R) + \mathbf{K}_{Rd}(\mathbf{x}_{Rd} - \mathbf{x}_R), \quad (6)$$

referenced at Σ_R , where $\mathbf{f}_R \in \mathbb{R}^{n_R}$ denotes relative contact forces between two end-effectors, which can be obtained from the virtual work theorem [50] as $\tau_e = \mathbf{J}_R^T \mathbf{f}_R$; $\mathbf{M}_{Rd}, \mathbf{B}_{Rd}, \mathbf{K}_{Rd} \in \mathbb{R}^{n_R \times n_R}$ denote desired mass, damping, and stiffness matrices, respectively; and $\mathbf{x}_{Rd}, \dot{\mathbf{x}}_{Rd}, \ddot{\mathbf{x}}_{Rd} \in \mathbb{R}^{n_R}$ denote the desired position and orientation, velocity, and acceleration vectors, respectively. The formulation (6) is called the *relative impedance control* equation, that allows a single control for the dual arm. As an example, when two 6-DOFs robots are used in a dual-arm system, instead of managing twelve components to perform impedance control for the two arms, the proposed approach uses only six components for the equivalent single manipulator and is therefore easier to manage and implement. Further, the desired motion is specified in terms of the relative motion between the end-effectors with respect to the task frame.

C. Time-Delay Estimation and Ideal-Velocity Feedback

There are two core techniques in this controller: TDE [3], [4] technique and IVF [47]. The TDE is an efficient and effective technique to estimate a robot dynamics without a model. And the IVF, which originated from natural admittance control (NAC) [51], [52], is used for eliminating discontinuous nonlinearities such as Coulomb friction, stiction, and inertial force uncertainties. Note that the former takes care of continuous nonlinearity, whereas the latter, of discontinuous nonlinearity.

To eliminate the two nonlinearities of the system, we use TDE as follows. First, we re-express the robot dynamics as

$$\tau = \bar{\mathbf{M}}\ddot{\mathbf{q}} + \mathbf{h}(\mathbf{q}, \dot{\mathbf{q}}, \ddot{\mathbf{q}}), \quad (7)$$

where $\bar{\mathbf{M}} \in \mathbb{R}^{n_T \times n_T}$ is a constant diagonal matrix, which may assume the nominal value of $\mathbf{M}(\mathbf{q})$, and $\mathbf{h}(\mathbf{q}, \dot{\mathbf{q}}, \ddot{\mathbf{q}}) = (\mathbf{M}(\mathbf{q}) - \bar{\mathbf{M}})\ddot{\mathbf{q}} + \mathbf{c}(\mathbf{q}, \dot{\mathbf{q}}) + \mathbf{g}(\mathbf{q}) + \mathbf{f}(\mathbf{q}, \dot{\mathbf{q}}) + \tau_d + \tau_e$.

Note that $\mathbf{h}(\mathbf{q}, \dot{\mathbf{q}}, \ddot{\mathbf{q}})$ contains all the continuous and discontinuous nonlinearities. In order to estimate it, we use TDE with the assumption that for a given time t , and a sampling period L that is sufficiently small, the following holds $\lim_{L \rightarrow 0} \mathbf{h}(\mathbf{q}, \dot{\mathbf{q}}, \ddot{\mathbf{q}})_{(t-L)} = \mathbf{h}(\mathbf{q}, \dot{\mathbf{q}}, \ddot{\mathbf{q}})$. Let $\hat{\mathbf{h}}(\mathbf{q}, \dot{\mathbf{q}}, \ddot{\mathbf{q}})$ denote the estimate of $\mathbf{h}(\mathbf{q}, \dot{\mathbf{q}}, \ddot{\mathbf{q}})$, then $\hat{\mathbf{h}}(\mathbf{q}, \dot{\mathbf{q}}, \ddot{\mathbf{q}}) = \mathbf{h}(\mathbf{q}, \dot{\mathbf{q}}, \ddot{\mathbf{q}})_{(t-L)}$. From (7) we get,

$$\hat{\mathbf{h}}(\mathbf{q}, \dot{\mathbf{q}}, \ddot{\mathbf{q}}) = \tau_{(t-L)} - \bar{\mathbf{M}}\ddot{\mathbf{q}}_{(t-L)}. \quad (8)$$

The robot dynamics in the operational space can be obtained by substituting (4) to (7) resulting in $\tau = \bar{\mathbf{M}}\mathbf{J}_R^+(\ddot{\mathbf{x}}_R - \dot{\mathbf{J}}_R\dot{\mathbf{q}}) + \mathbf{h}(\mathbf{q}, \dot{\mathbf{q}}, \ddot{\mathbf{q}})$, where from (4), we set ν to zero. From (7) we set $\tau = \tau_u$ where τ_u is the control torque which is designed as follows

$$\tau_u = \bar{\mathbf{M}}\mathbf{J}_R^+(\mathbf{v}_d - \dot{\mathbf{J}}_R\dot{\mathbf{q}}) + \hat{\mathbf{h}}(\mathbf{q}, \dot{\mathbf{q}}, \ddot{\mathbf{q}}). \quad (9)$$

The symbol \mathbf{v}_d is a control law that combines the relative impedance equation with the IVF correction term and is expressed as

$$\mathbf{v}_d = \underbrace{\ddot{\mathbf{x}}_{Rd} + \mathbf{M}_{Rd}^{-1}(\mathbf{B}_{Rd}(\dot{\mathbf{x}}_{Rd} - \dot{\mathbf{x}}_R) + \mathbf{K}_{Rd}(\mathbf{x}_{Rd} - \mathbf{x}_R) + \mathbf{f}_R)}_{\text{injecting relative impedance behaviors}} + \underbrace{\Gamma(\dot{\mathbf{x}}_{R,ideal} - \dot{\mathbf{x}}_R)}_{\text{ideal velocity feedback}}, \quad (10)$$

where $\Gamma \in \mathbb{R}^{n_R \times n_R}$ denotes the IVF gain and is a constant diagonal matrix, and $\dot{\mathbf{x}}_{R,ideal}$, called ideal velocity, is defined as

$$\dot{\mathbf{x}}_{R,ideal} \triangleq \int \{ \ddot{\mathbf{x}}_{Rd} + \mathbf{M}_{Rd}^{-1}[\mathbf{B}_{Rd}(\dot{\mathbf{x}}_{Rd} - \dot{\mathbf{x}}_R) + \mathbf{K}_{Rd}(\mathbf{x}_{Rd} - \mathbf{x}_R) + \mathbf{f}_R] \} dt. \quad (11)$$

Finally, the control torque is obtained as follows:

$$\tau_u = \underbrace{\tau_{u(t-L)} - \bar{\mathbf{M}}\ddot{\mathbf{q}}_{(t-L)}}_{\text{time delay estimation}} + \bar{\mathbf{M}}\mathbf{J}_R^+ \{ \underbrace{\ddot{\mathbf{x}}_{Rd} + \mathbf{M}_{Rd}^{-1}[\mathbf{B}_{Rd}(\dot{\mathbf{x}}_{Rd} - \dot{\mathbf{x}}_R) + \mathbf{K}_{Rd}(\mathbf{x}_{Rd} - \mathbf{x}_R) + \mathbf{f}_R]}_{\text{injecting relative impedance behaviors}} - \dot{\mathbf{J}}_R\dot{\mathbf{q}} + \bar{\mathbf{M}}\mathbf{J}_R^+ \underbrace{\Gamma(\dot{\mathbf{x}}_{R,ideal} - \dot{\mathbf{x}}_R)}_{\text{ideal velocity feedback}} \}. \quad (12)$$

We apply the control torque (12) to the robot dynamics (7), where $\ddot{\mathbf{q}} = \mathbf{J}_R^+(\ddot{\mathbf{x}}_R - \dot{\mathbf{J}}_R\dot{\mathbf{q}})$, and results in

$$\bar{\mathbf{M}}\mathbf{J}_R^+(\ddot{\mathbf{x}}_R - \dot{\mathbf{J}}_R\dot{\mathbf{q}}) + \mathbf{h}(\mathbf{q}, \dot{\mathbf{q}}, \ddot{\mathbf{q}}) = \tau_{u(t-L)} - \bar{\mathbf{M}}\ddot{\mathbf{q}}_{(t-L)} + \bar{\mathbf{M}}\mathbf{J}_R^+ \{ \ddot{\mathbf{x}}_{Rd} + \mathbf{M}_{Rd}^{-1}[\mathbf{B}_{Rd}(\dot{\mathbf{x}}_{Rd} - \dot{\mathbf{x}}_R) + \mathbf{K}_{Rd}(\mathbf{x}_{Rd} - \mathbf{x}_R) + \mathbf{f}_R] - \dot{\mathbf{J}}_R\dot{\mathbf{q}} \} + \bar{\mathbf{M}}\mathbf{J}_R^+ \Gamma(\dot{\mathbf{x}}_{R,ideal} - \dot{\mathbf{x}}_R). \quad (13)$$

Due to discontinuous nonlinearities, the TDE compensation cannot accurately cancel the effects of the robot dynamics, that is,

$$\mathbf{h}(\mathbf{q}, \dot{\mathbf{q}}, \ddot{\mathbf{q}}) \neq \hat{\mathbf{h}}(\mathbf{q}, \dot{\mathbf{q}}, \ddot{\mathbf{q}}) = \tau_{u(t-L)} - \bar{\mathbf{M}}\ddot{\mathbf{q}}_{(t-L)}. \quad (14)$$

(This discussion can be found in [47].) Thus the difference between the TDE compensation and discontinuous nonlinearities results into an ϵ error,

$$\epsilon = \mathbf{J}_R \bar{\mathbf{M}}^{-1}(\tau_{u(t-L)} - \bar{\mathbf{M}}\ddot{\mathbf{q}}_{(t-L)} - \mathbf{h}(\mathbf{q}, \dot{\mathbf{q}}, \ddot{\mathbf{q}})). \quad (15)$$

And by applying (15) to (13) we get,

$$\ddot{\mathbf{x}}_R - \ddot{\mathbf{x}}_{Rd} + \mathbf{M}_{Rd}^{-1}[\mathbf{B}_{Rd}(\dot{\mathbf{x}}_R - \dot{\mathbf{x}}_{Rd}) + \mathbf{K}_{Rd}(\mathbf{x}_R - \mathbf{x}_{Rd}) - \mathbf{f}_R] = \epsilon - \Gamma(\dot{\mathbf{x}}_R - \dot{\mathbf{x}}_{R,ideal}) = \delta \quad (16)$$

where δ represents a very small number. We tune the value of

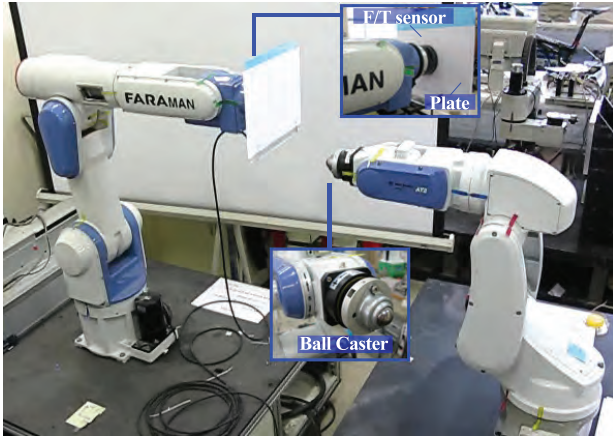


Fig. 2: The experimental setup of dual-arm system: Faraman-AC2 as a reference robot with the acrylic plate (left) and Faraman-AT2 as a tool robot with a ball-caster (right).

Γ by trial and error in order to keep $\epsilon \simeq \Gamma(\dot{\mathbf{x}}_R - \dot{\mathbf{x}}_{R,ideal})$. This results to our target dynamics in (6). The implementation details of this proposed controller are discussed in Subsection III-C.

III. EXPERIMENT

This work will present three sets of experiments to verify the proposed relative impedance control on a dual-arm system performing ABTs, including contact, non-contact, and transition, in an effective and stable manner. For a given task, this work will demonstrate how the desired trajectory and impedance can be specified.

A. Experimental Setup

A dual-arm realtime control platform is developed for the experiments.

1) *Hardware Configuration*: As shown in Fig. 2, the dual arm consists of two 6-DOFs PUMA-type industrial robots manufactured by Samsung Corporation: Faraman-AC2 as a reference robot (left), and Faraman-AT2 as a tool robot (right). At the end-effector of the reference robot, a force-torque sensor is attached, and on top of it, an acrylic plate is securely fixed. This force-torque sensor measures \mathbf{f}_R , that is, the relative contact force with respect to Σ_R . The plate is covered with a sheet of white paper to make the writing more visible. A steel ball-caster with red ink is attached to the end-effector of the tool robot.

The frame assignment of each manipulator is shown in Fig. 3, while Table I is expressed using Denavit-Hartenberg (D-H) parameters in Craig's notation [53]. Gear reduction ratios are $\{207.7, 320.0, 220.0, 272.7, 138.5, 133.3\}$ for Faraman AC2, and $\{120, 120, 120, 100, 80, 50\}$ for Faraman AT2. Voltage to torque ratios are $\{87.09, 68.27, 46.93, 29.09, 7.38, 7.11\}$ Nm/V for Faraman-AC2 and $\{25.45, 25.45, 12.75, 10.62, 4.26, 2.66\}$ Nm/V for Faraman-AT2. Encoder for each joint of the two manipulators has a resolution of 2048 pulses/rev. The ATI Gamma SI-130-10 force-torque sensor has 1/80 N resolution for the forces and 1/3200 Nm resolution for the torques.

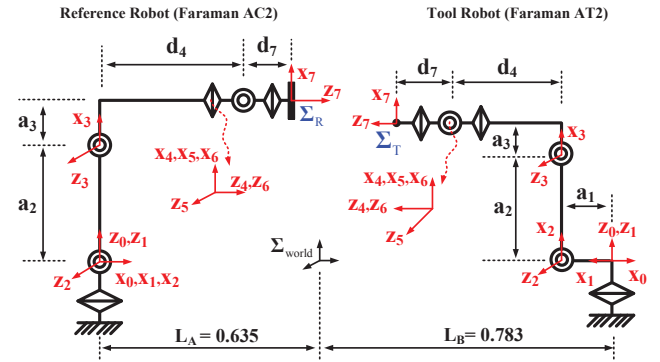


Fig. 3: The assignment of link frames for the dual-arm robot system.

TABLE I: D-H parameters of two industrial robots

(a) Faraman AC2 (reference Robot)				
i	α_{i-1}	a_{i-1}	d_{i-1}	θ_i
1	0	0	0	q_1
2	$\pi/2$	0	0	$q_2 + \pi/2$
3	0	0.42	0	q_3
4	$\pi/2$	0.1	0.5	q_4
5	$-\pi/2$	0	0	q_5
6	$\pi/2$	0	0	q_6
7	$\pi/2$	0	0.179	0

(b) Faraman AT2 (Tool Robot)				
i	α_{i-1}	a_{i-1}	d_{i-1}	θ_i
1	0	0	0	$q_7 + \pi$
2	0	0	0	$q_8 - \pi/2$
3	0	0.255	0	q_9
4	$-\pi/2$	0.096	0.3	q_{10}
5	$\pi/2$	0	0	q_{11}
6	$-\pi/2$	0	0	q_{12}
7	0	0	0.151	0

The controller uses an industrial PC with a 2.4-GHz Pentium 4 where three types of data acquisition boards are placed (as shown in Fig. 4): two Contec DA12-8L boards outputs analog voltages for control inputs, two Sensoray S626 boards read joint angles and output digital signals for joint brakes, and one National Instrument PCI-6034E board obtains the data from the force-torque sensor.

2) *Software Configuration*: The controller is implemented by using C++ running under Linux with Real-Time Application Interface (RTAI) [54]. Sampling period is set to 2 ms. This system uses an open-source Linux driver COMEDI for the real-time data acquisition and an open-source library Newmat 11 for the matrix computation.

3) *Contact Environment*: An acrylic plate (250 mm x 250 mm x 8 mm) of light and stiff material is used¹. The mass of the plate is 0.573 kg, and the stiffness is about 8,000 N/m.

¹It is known that a manipulator's contact task is more difficult to conduct in a stiff environment than in a soft environment [53], [55]

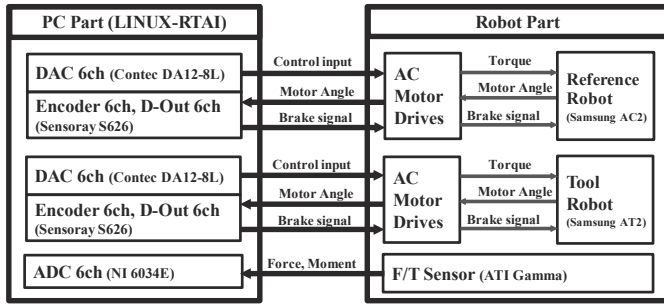


Fig. 4: The schematic diagram of the dual-arm real-time control platform.

B. Description of Experiment

In order to demonstrate ABTs with contact, non-contact, and transition through coordinated action between two 6-DOFs industrial robots, a writing task is conducted. The tool robot writes three letters, ‘J,’ ‘O,’ and ‘Y’ on the plate attached to the end-effector of the reference robot. The details are as follows.

1) *Desired Trajectories of Relative Position and Relative Orientation:* The relative path, $[X_R, Y_R, Z_R]^T$, is shown in Fig. 5. It is designed to write the three-letter-word ‘JOY’ on the X_R - Y_R plane. The displacement in the direction of the Z_R axis is set to exceed the position of the plate in order to maintain contact during the writing. Each trajectory of the relative position is composed of 27 segments (including straight lines and curves), and each segment is formed by the fifth order polynomial trajectory, $[X_R(t), Y_R(t), Z_R(t)]^T$, for the given time intervals as shown in Fig. 6. Throughout the task ($t = 0$ to 66 s), the trajectories of the desired relative orientation are designed to keep the end-effector of the right arm perpendicular to the plate attached to the end-effector of the left arm, which makes the roll-pitch-yaw angles referenced at Σ_R equal to $[\alpha_R, \beta_R, \gamma_R]^T = [\pi, 0, 0]^T$, using Euler angles system II [56]. In this approach, only the desired value of \mathbf{x}_R is necessary, and not the individual desired values of each end-effector.

2) *Desired Relative Impedance:* In the constrained direction, Z_R , of the 6-DOFs task-space, a compliant behavior—high damping and low stiffness—is required to perform ten transitions between the contact state and non-contact state against the stiff plate. To verify that the proposed control along Z_R can achieve the desired relative impedance precisely and robustly, three overdamped impedance dynamics along Z_R is tested with damping ratios $\zeta_{Z_R} = 4, 5, 6$. For the remaining DOFs, a stiff behavior—low damping and high stiffness—is required for accurate writing at critically-damped impedance, $\zeta = 1$. For each overdamped ζ_{Z_R} , corresponding values of desired relative mass matrix, \mathbf{M}_{Rd} , damping matrix, \mathbf{B}_{Rd} , and stiffness matrix, \mathbf{K}_{Rd} , are set. These are shown in Table II. Here, relative impedance with respect to the relative reference frame is specified, and not the absolute impedances of each end-effector. Note that the dual arm is controlled as a single manipulator thus the matrices are of size 6×6 .

C. Implementation of the Proposed Controller

In order to accomplish the desired relative trajectory and relative impedance behavior, the proposed controller, as shown in (12), is used for the experiments. The selection of $\bar{\mathbf{M}}$ has a significant effect on the control performance and thus is worth mentioning. In principle, the best selection of $\bar{\mathbf{M}}$ is perhaps $\mathbf{M}(\mathbf{q})$, the actual inertia matrix. Nevertheless, since $\mathbf{M}(\mathbf{q})$ is difficult to accurately estimate and computationally demanding to implement on real-time basis, $\bar{\mathbf{M}}$ is often tuned by trial and error. More specifically, its diagonal elements are gradually increased from a small positive value within the region of stability, without using system parameters [47]. The elements of the IVF gain, Γ , are set at the highest values where no control chatter occurs. The closed-loop stability analysis due to this control is given in Appendix A.

Incidentally, we take note that the proposed control requires the joint acceleration, $\ddot{\mathbf{q}}_{(t-L)}$, for the TDE. The encoder signal is usually contaminated by noise in the real experiment, and the effect of the noise is amplified due to the calculation of the joint acceleration by numerical differentiation. Fortunately, it was proven in [41] that the noise can be attenuated by *lowering* $\bar{\mathbf{M}}$ without explicitly using an additional low-pass filter, which has the implication of aforementioned tuning process of $\bar{\mathbf{M}}$.

The use of our relative impedance equation, as shown in (6), results in the specification of our desired task that is equivalent to that of a single manipulator. The values of the parameters of the control law are assigned as follows. The gain $\bar{\mathbf{M}} \in \mathbb{R}^{12 \times 12}$ is set to $\text{diag}(6.62, 5.15, 1.90, 0.84, 0.17, 0.14, 0.99, 0.97, 0.45, 0.32, 0.05, 0.02)$ kg-m², where the first six elements correspond to the reference robot, and the remaining six elements correspond to the tool robot. The relative Jacobian $\mathbf{J}_R \in \mathbb{R}^{6 \times 12}$ is computed based on [2]. The parameters $\mathbf{x}_{Rd}, \dot{\mathbf{x}}_{Rd}, \ddot{\mathbf{x}}_{Rd} \in \mathbb{R}^6$ are assigned based on the desired fifth-order polynomial trajectory as shown in Figs. 5 and 6. The values of $\mathbf{M}_{Rd}, \mathbf{B}_{Rd}, \mathbf{K}_{Rd} \in \mathbb{R}^{6 \times 6}$ are based on Table II. The relative position and orientation vector, $\mathbf{x}_R = [X_R, Y_R, Z_R, \alpha_R, \beta_R, \gamma_R]^T \in \mathbb{R}^6$, is computed from forward kinematics based on $\mathbf{q} \in \mathbb{R}^{12}$ feedback. The parameter $\dot{\mathbf{x}}_R \in \mathbb{R}^6 = \mathbf{J}_R \dot{\mathbf{q}}$ where $\dot{\mathbf{q}} \in \mathbb{R}^{12}$ is computed by numerical differentiation of \mathbf{q} . The value of $\mathbf{f}_R \in \mathbb{R}^6$ is measured by the force-torque sensor attached at the end-effector of left arm. The value of $\dot{\mathbf{J}}_R$ is calculated by using a numerical differentiation of \mathbf{J}_R . The gain $\Gamma \in \mathbb{R}^{6 \times 6}$ is set to $\text{diag}(50, 50, 50, 50, 50, 50)$. The value of $\dot{\mathbf{x}}_{R,ideal} \in \mathbb{R}^6$ is based on (11). And finally, the value of $\tau_{u(t-L)} - \bar{\mathbf{M}}\ddot{\mathbf{q}}_{(t-L)}$ is based on the previous computation cycle, where $L = 2$ ms.

D. Experimental Results

1) *Experiment 1– Desired Relative Impedance Set #1:* A dual-arm writing task is conducted with the desired impedance set #1 shown in Table II. The snapshots of the dual-arm performing the desired task is shown in Fig. 7, and the experimental result is shown in Fig. 8. We can see the three-letter-word ‘JOY’ is accurately written on the paper through the grid (10 mm x 10 mm) in the image. Note that the uneven thickness of the word turned out to be the result of irregular supply of ink to the steel ball, not the outcome of control

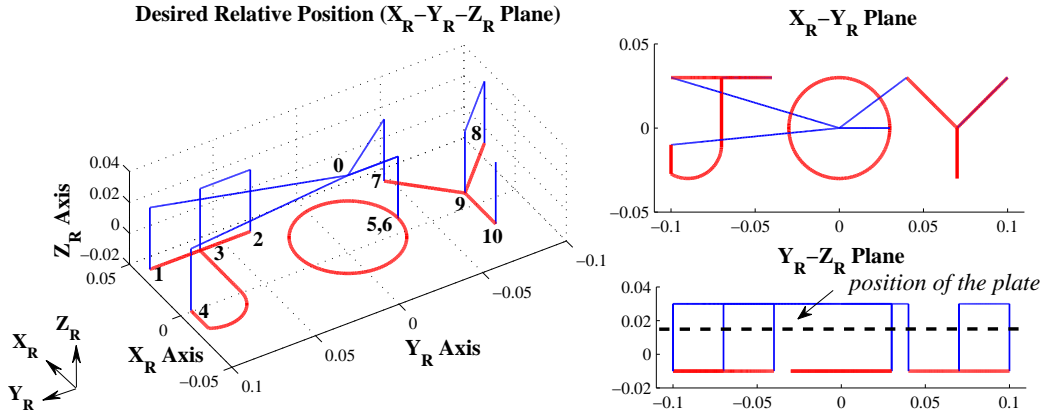


Fig. 5: The figure shows a desired relative position path, $[X_R, Y_R, Z_R]^T$: the blue solid line denotes the path of free motion; the red solid line the path of constrained motion. In the 3D plot, the numbers from 0 to 10 indicate the order of the transition; in the Y_R - Z_R plane plot, the black dotted line indicates the expected position of the plate.

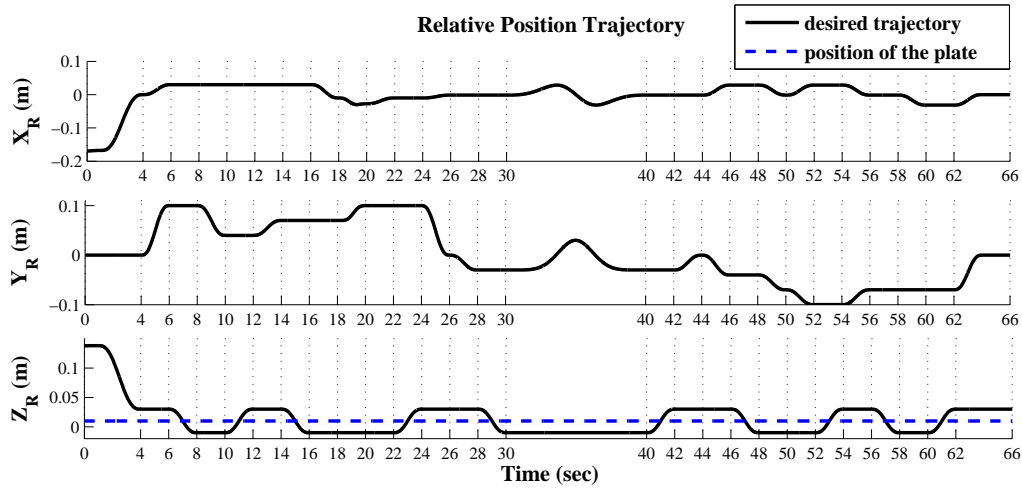


Fig. 6: The figure shows a desired relative position trajectory, $[X_R(t), Y_R(t), Z_R(t)]^T$: the grid of the time axis indicates time intervals of each segment of the trajectory. In the plot of Z_R axis, the dotted line (blue) indicates the expected position of the plate.

TABLE II: Three sets of the 6-DOFs desired relative impedance

	M_{Rd}	B_{Rd}	K_{Rd}	$\zeta_{Z_R}^a$
Set #1	$10 \cdot \mathbf{I}_6^b$	diag(200, 200, 620, 200, 200, 200)	diag(1000, 1000, 600, 1000, 1000, 1000)	4
Set #2	$10 \cdot \mathbf{I}_6$	diag(200, 200, 700, 200, 200, 200)	diag(1000, 1000, 500, 1000, 1000, 1000)	5
Set #3	$10 \cdot \mathbf{I}_6$	diag(200, 200, 760, 200, 200, 200)	diag(1000, 1000, 400, 1000, 1000, 1000)	6

^a ζ_{Z_R} denotes the damping ratio of the Z_R axis. The damping ratios of the other axes are all critically damped, $\zeta = 1$.

^b \mathbf{I}_6 denotes the 6×6 identity matrix.

performance. This was confirmed through the reproduction of writing with the saved data of relative position response in Fig. 9.

The responses of relative position along X_R , Y_R , and Z_R axes in meters and relative orientation in degrees of α_R , β_R , and γ_R angles are shown in Fig. 10. The root mean square (RMS) values of tracking errors are presented in Table III.

Except for the Z_R direction, good tracking accuracy was achieved. The position error along the Z_R direction is necessary in order to maintain contact and achieve the desired relative impedance. This result confirms that the desired relative impedance behavior is achieved well. Throughout the writing task, the value of manipulability measure for the relative Jacobian has the range $\sqrt{\det(\mathbf{J}_R \mathbf{J}_R^T)} = [3.733, 4.456]$.

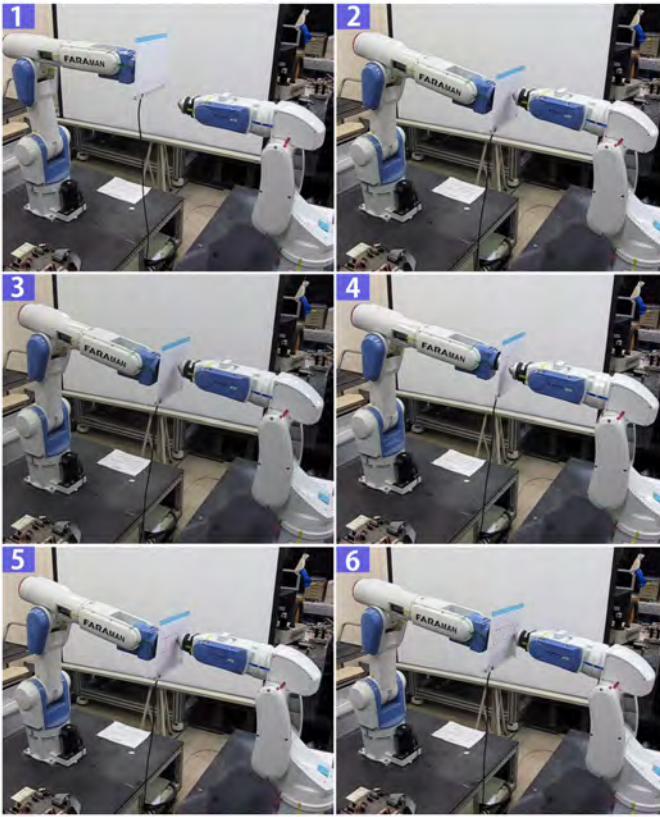


Fig. 7: Snapshots of the dual-arm system performing the writing task: the tool robot writes the word ‘JOY’ on a plate attached to the reference robot.

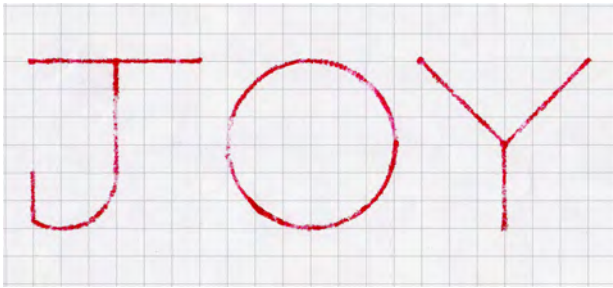


Fig. 8: The scanned image of the result of writing-experiment: the length and width of the grids are 10 mm x 10 mm.

TABLE III: The RMS errors of relative position and orientation responses

	RMS error (m)		RMS error (deg)
X_R	0.0009	α_R	0.0015
Y_R	0.0001	β_R	0.0034
Z_R	0.0160	γ_R	0.0007

In order to investigate the accuracy of the achieved relative impedance more quantitatively, we have considered the following relative impedance error norm [57]:

$$|\sigma_R| \triangleq |(\mathbf{M}_{Rd}\ddot{\mathbf{e}}_R + \mathbf{B}_{Rd}\dot{\mathbf{e}}_R + \mathbf{K}_{Rd}\mathbf{e}_R) - \mathbf{f}_R|, \quad (17)$$

where $\mathbf{e}_R = \mathbf{x}_{Rd} - \mathbf{x}_R$ denotes the error vector of the relative position and orientation, and $\dot{\mathbf{e}}_R$ and $\ddot{\mathbf{e}}_R$ are the corresponding relative velocity and acceleration errors. The relative impedance error norm along the Z_R direction is shown in Fig. 11. Throughout the task, the RMS value of the impedance error is 0.397 N. The peaks in Fig. 11 occurred at the instance of contact with the surface, and thus are construed to come from impact forces.

The correctness of σ_R can be verified by an inspection of the contact force response \mathbf{f}_R along the Z_R axis shown in Fig. 12. As the response reaches the steady-state, the relative impedance behavior, as shown in (6), becomes $\mathbf{f}_R \simeq \mathbf{K}_{Rd}(\mathbf{x}_{Rd} - \mathbf{x}_R)$. Therefore, an inspection of the steady-state ($t = 8-10, 16-22, 30-40, 48-52$ and $58-60$ s) reveals that the relative stiffness is 595.62 N/m, which is within about a 0.73 % error of the desired stiffness of 600 N/m. The peaks in the force response is due to the impact when the two end-effectors come into contact. Note that the fluctuation in the steady-state comes from the dynamic coupling: the force in one direction is affected by the motion of the other directions [57], [58]. From the above results, it may be concluded that the desired relative impedance is realized successfully.

2) *Experiment 2– Desired Relative Impedance Sets #2 and #3:* In order to verify the performance of the proposed controller when various desired impedances are implemented, the same writing task is performed under two additional conditions: the sets #2 and #3 shown in Table II. The presented variation in damping ratio is modified with respect to the damping coefficient, \mathbf{B}_{Rd} , and spring constant, \mathbf{K}_{Rd} . However, we can also change the damping ratio to its desired value by varying the inertia coefficient, \mathbf{M}_{Rd} .

The relative position response along the constrained direction, Z_R , for the three experimental sets are shown in Fig. 13. The changes in the response according to the relative impedance are observed: the smaller the damping ratio, ζ_{Z_R} , of the desired relative impedance becomes, the faster is the settling time, and the smaller the overshoot.

The relative impedance error norms along the constrained direction, Z_R , during the writing task for the three experiments are shown in Fig. 14: the RMS errors for sets #2 and #3 are 0.419 N and 0.441 N, respectively. The relative contact force responses along the constrained direction, \mathbf{f}_R along Z_R , are shown in Fig. 15 with the desired stiffness of the sets #1, #2, and #3. An inspection of the steady-state ($t = 8-10, 16-22, 30-40, 48-52$, and $58-60$ s) reveals that the relative stiffness for Sets #2 and #3 are very close to the desired value: the realized relative stiffnesses are 505.10 N/m and 405.4 N/m, and their deviations from the desired values are 1.02 % and 1.35 %, respectively. From the above results, it can be deduced that the proposed controller achieves the desired relative impedance quite well under different impedance values.

IV. CONCLUSION

This work has proposed a method of implementing impedance control on a dual-arm system, that is treated as a single manipulator, and performing an asymmetric bimanual task. The proposed task is a writing task, where the tool robot

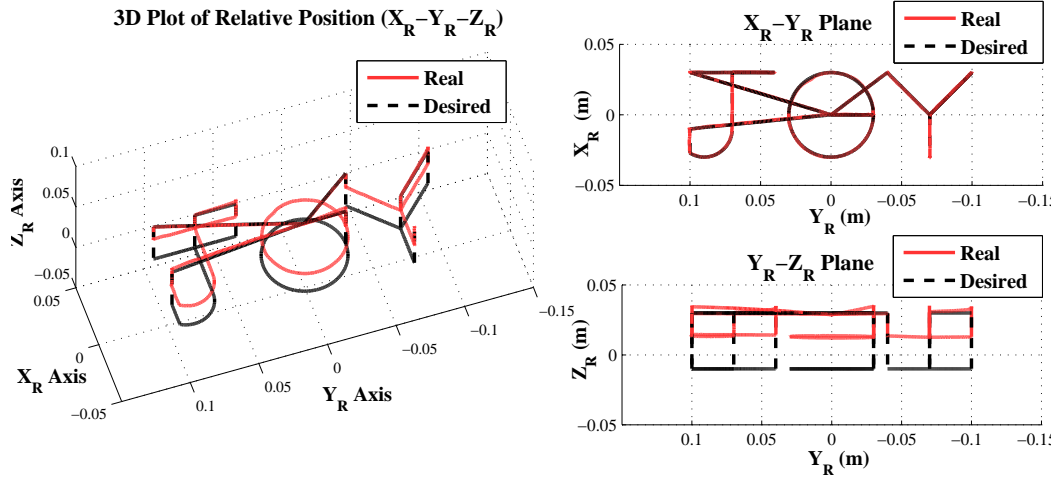


Fig. 9: The response of relative position path, $[X_R, Y_R, Z_R]^T$: the dotted line (black) indicates the desired trajectory; the solid line (red) the real trajectory.

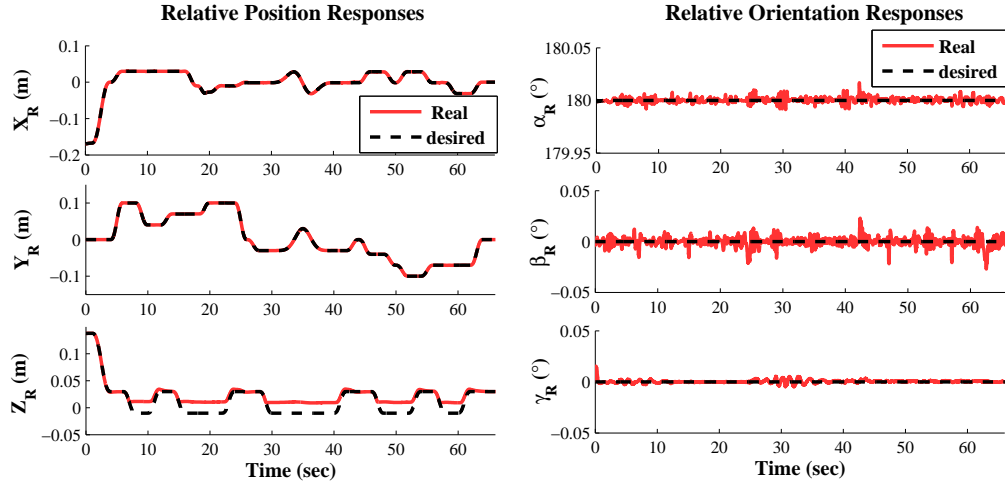


Fig. 10: The responses of relative position and orientation trajectory: the dotted line (black) indicates the desired trajectory; the solid line (red) the real trajectory.

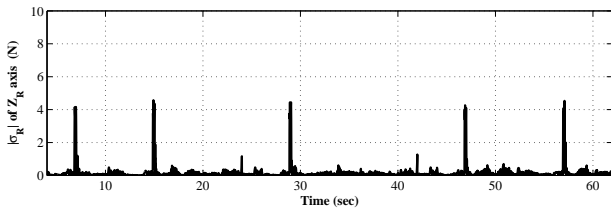


Fig. 11: The relative impedance error norm, as shown in (17), along the constrained direction, Z_R .

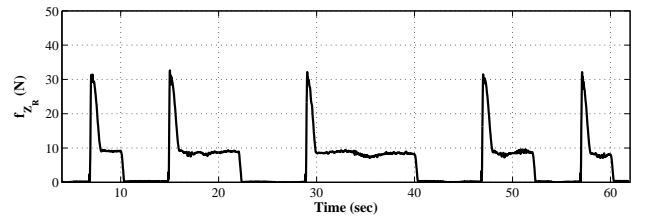


Fig. 12: The contact force response f_R along the constrained direction, Z_R , during the writing.

writes the word 'JOY' on a plate attached to the reference robot. Through the use of a relative Jacobian, the impedance control was reduced to a single controller for both arms, such that the relative motion between the two end-effectors characterized the execution of the desired task. This makes the proposed impedance control simpler and more intuitive when specifying the desired impedance and the desired trajectories. For the writing task implementation, three sets of experiments

were shown at different damping ratios. The relative stiffness assumed a maximum steady state error of 1.35%. The use of time-delay estimation made the proposed controller easier to implement. And lastly, a stability analysis of the proposed controller was presented which showed that the error was ultimately bounded.

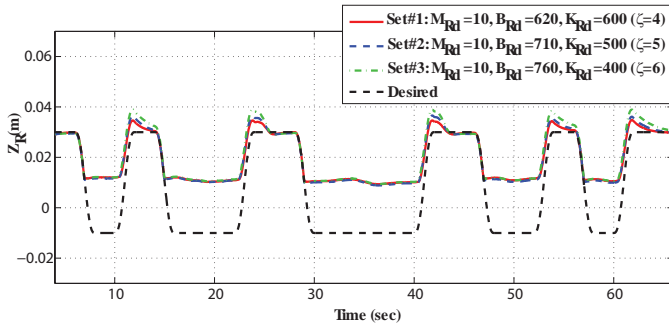


Fig. 13: The relative position response along the constrained direction, Z_R , as the desired relative impedance varies.

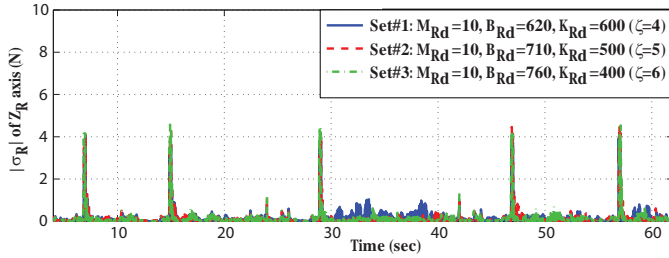


Fig. 14: The relative impedance error norm along the constrained direction, Z_R , during the writing task as the desired relative impedance varies.

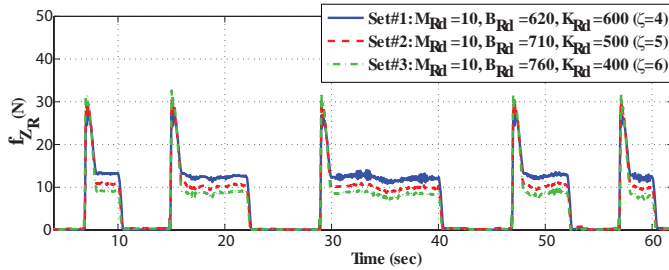


Fig. 15: The relative contact force response along the constrained direction, Z_R , as the desired relative impedance varies.

APPENDIX A STABILITY ANALYSIS IN SECTION III

Here, the stability of the overall system with the control law (12) is presented. By substituting (9) into (7), the closed-loop dynamics due to the proposed control becomes

$$\bar{\mathbf{M}}[\mathbf{J}_R^+(\mathbf{v}_d - \dot{\mathbf{J}}_R \dot{\mathbf{q}}) - \ddot{\mathbf{q}}] = \mathbf{h}(\mathbf{q}, \dot{\mathbf{q}}, \ddot{\mathbf{q}}) - \hat{\mathbf{h}}(\mathbf{q}, \dot{\mathbf{q}}, \ddot{\mathbf{q}}). \quad (18)$$

If \mathbf{J}_R is nonsingular, the closed-loop dynamics shown in (18) can be expressed as

$$\mathbf{v}_d - \ddot{\mathbf{x}}_R = \mathbf{J}_R \boldsymbol{\varepsilon} \quad (19)$$

with the TDE error $\boldsymbol{\varepsilon}$ defined as

$$\boldsymbol{\varepsilon} \triangleq \bar{\mathbf{M}}^{-1}[\mathbf{h}(\mathbf{q}, \dot{\mathbf{q}}, \ddot{\mathbf{q}}) - \hat{\mathbf{h}}(\mathbf{q}, \dot{\mathbf{q}}, \ddot{\mathbf{q}})], \quad (20)$$

or by expressing \mathbf{v}_d from (10),

$$\ddot{\mathbf{x}}_{Rd} - \ddot{\mathbf{x}}_R + \mathbf{M}_{Rd}^{-1}[\mathbf{B}_{Rd}(\dot{\mathbf{x}}_{Rd} - \dot{\mathbf{x}}_R)$$

$$+ \mathbf{K}_{Rd}(\mathbf{x}_{Rd} - \mathbf{x}_R) + \mathbf{f}_{Rd}] + \boldsymbol{\Gamma}(\dot{\mathbf{x}}_{R,ideal} - \dot{\mathbf{x}}_R) = \mathbf{J}_R \boldsymbol{\varepsilon}. \quad (21)$$

Here, by defining the integral sliding surface [59] as

$$\mathbf{s} = \int \{ \ddot{\mathbf{x}}_{Rd} - \ddot{\mathbf{x}}_R + \mathbf{M}_{Rd}^{-1}[\mathbf{B}_{Rd}(\dot{\mathbf{x}}_{Rd} - \dot{\mathbf{x}}_R) + \mathbf{K}_{Rd}(\mathbf{x}_{Rd} - \mathbf{x}_R) + \mathbf{f}_{Rd}] \} dt, \quad (22)$$

and from (11) we get $\mathbf{s} = \dot{\mathbf{x}}_{R,ideal} - \dot{\mathbf{x}}_R$, the closed-loop dynamics can be obtained as follows:

$$\dot{\mathbf{s}} + \boldsymbol{\Gamma} \mathbf{s} = \mathbf{J}_R \boldsymbol{\varepsilon}. \quad (23)$$

If $\mathbf{J}_R \boldsymbol{\varepsilon}$ is asymptotically bounded, then the overall system is bounded-input-bounded-output (BIBO) stable. Therefore, to prove the stability, we investigate the following inequality equation:

$$\|\dot{\mathbf{s}} + \boldsymbol{\Gamma} \mathbf{s}\| = \|\mathbf{J}_R \boldsymbol{\varepsilon}\| \leq \|\mathbf{J}_R\| \|\boldsymbol{\varepsilon}\|. \quad (24)$$

From the definition of the relative Jacobian, $\dot{\mathbf{x}}_R = \mathbf{J}_R \dot{\mathbf{q}}$, it can be inferred that if \mathbf{J}_R is unbounded, then even very small joint displacement cause infinite displacement of relative position (or orientation); however, it will never happen in the physical system. Hence, the relative Jacobian is bounded as

$$\|\mathbf{J}_R\| \leq \alpha, \quad (25)$$

where α is a positive value. To find the boundness of $\boldsymbol{\varepsilon}$, by defining the reference joint acceleration as $\ddot{\mathbf{q}}^* \triangleq \mathbf{J}_R^+(\mathbf{v}_d - \dot{\mathbf{J}}_R \dot{\mathbf{q}})$, (18) can be reformulated as follows:

$$\ddot{\mathbf{q}}^* - \ddot{\mathbf{q}} = \boldsymbol{\varepsilon}. \quad (26)$$

According to the proof provided in [47], [60], if the time delay L is sufficiently small and roots of $[\mathbf{I} - \mathbf{M}^{-1}\bar{\mathbf{M}}]$ reside inside a unit circle, the TDE error $\boldsymbol{\varepsilon}$ is bounded as

$$\|\boldsymbol{\varepsilon}\| \leq \beta, \quad (27)$$

where β is a positive value. From (24), (25), and (27), it can be determined that

$$\|\dot{\mathbf{s}} + \boldsymbol{\Gamma} \mathbf{s}\| = \|\mathbf{J}_R \boldsymbol{\varepsilon}\| \leq \alpha \beta \triangleq \gamma, \quad (28)$$

where γ is a positive value.

Then, Lyapunov-based stability of the overall system can be proved in the same manner as the stability proof in [47]. The Lyapunov function can be taken as $V = 0.5 \mathbf{s}^T \mathbf{s}$; the derivative of V is given by $\dot{V} = -\mathbf{s}^T \boldsymbol{\Gamma} \mathbf{s} + \mathbf{s}^T \mathbf{J}_R \boldsymbol{\varepsilon}$. Then we can obtain $\dot{V} < 0$ under the condition $|\mathbf{s}_i| > |\{\boldsymbol{\Gamma}^{-1} \mathbf{J}_R \boldsymbol{\varepsilon}\}_i|$, where the subscript \bullet_i denotes the i -th element of the vector \bullet . Since $\mathbf{J}_R \boldsymbol{\varepsilon}$ is bounded as (28), the integral sliding surface, \mathbf{s} , is globally uniformly ultimately bounded with the ultimate bound $|\mathbf{s}_i| \leq \gamma \|\boldsymbol{\Gamma}^{-1}\|$.

ACKNOWLEDGEMENT

This work was supported in part by the DGIST R&D Program of the Ministry of Education, Science, and Technology of Korea (11-BD-0402) and in part by the Technology Innovation Program 10040106 of the Ministry of Knowledge Economy, Korea.

REFERENCES

- [1] C. Lewis and A. Maciejewski, "Trajectory generation for cooperating robots," in *Systems Engineering, 1990., IEEE International Conference on*, Aug. 1990, pp. 300–303.
- [2] A. Mohri, M. Yamamoto, and G. Hirano, "Cooperative path planning for two manipulators," in *Robotics and Automation, 1996. Proceedings., 1996 IEEE International Conference on*, vol. 3. IEEE, 1996, pp. 2853–2858.
- [3] T. Hsia, T. Lasky, and Z. Guo, "Robust independent joint controller design for industrial robot manipulators," *Industrial Electronics, IEEE Transactions on*, vol. 38, no. 1, pp. 21–25, Feb. 1991.
- [4] K. Youcef-Toumi and O. Ito, "A time delay controller for systems with unknown dynamics," *Journal of Dynamic Systems, Measurement, and Control*, vol. 112, no. 1, pp. 133–142, 1990.
- [5] Y. Jin, P. Chang, M. Jin, and D. Gweon, "Stability guaranteed time delay control of manipulators using nonlinear damping and terminal sliding mode," *Industrial Electronics, IEEE Transactions on*, vol. PP, no. 99, p. 1, 2012.
- [6] J. Lee, M. Jin, and K. K. Ahn, "Precise tracking control of shape memory alloy actuator systems using hyperbolic tangential sliding mode control with time delay estimation," *Mechatronics*, vol. 23, no. 3, pp. 310–317, 2013.
- [7] N. Hogan, "Impedance control: an approach to manipulation: parts 1, 2, 3," *Journal of Dynamic Systems, Measurement and Control*, vol. 107, pp. 1–24, 1985.
- [8] S. Schneider and R. Cannon Jr, "Object impedance control for cooperative manipulation: Theory and experimental results," *Robotics and Automation, IEEE Transactions on*, vol. 8, no. 3, pp. 383–394, 1992.
- [9] R. Bonitz and T. Hsia, "Internal force-based impedance control for cooperating manipulators," *Robotics and Automation, IEEE Transactions on*, vol. 12, no. 1, pp. 78–89, 1996.
- [10] F. Caccavale, P. Chiacchio, A. Marino, and L. Villani, "Six-dof impedance control of dual-arm cooperative manipulators," *Mechatronics, IEEE/ASME Transactions on*, vol. 13, no. 5, pp. 576–586, 2008.
- [11] Y. Guiard, "Asymmetric division of labor in human skilled bimanual action: the kinematic chain as a model," *Journal of Motor Behavior*, vol. 19, pp. 486–517, 1987.
- [12] R. Zollner, T. Asfour, and R. Dillmann, "Programming by demonstration: dual-arm manipulation tasks for humanoid robots," in *Intelligent Robots and Systems, 2004. (IROS 2004). Proceedings. 2004 IEEE/RSJ International Conference on*, vol. 1, 2004, pp. 479–484 vol.1.
- [13] M. Uchiyama and P. Dauchez, "A symmetric hybrid position/force control scheme for the coordination of two robots," in *Robotics and Automation, 1988. Proceedings., 1988 IEEE International Conference on*. IEEE, 1988, pp. 350–356.
- [14] T. Yoshikawa and X. Zheng, "Coordinated dynamic hybrid position/force control for multiple robot manipulators handling one constrained object," *The International Journal of Robotics Research*, vol. 12, no. 3, pp. 219–230, 1993.
- [15] A. Albu-Schaffer, O. Eiberger, M. Grebenstein, S. Haddadin, C. Ott, T. Wimbock, S. Wolf, and G. Hirzinger, "Soft Robotics," *Robotics & Automation Magazine, IEEE*, vol. 15, no. 3, pp. 20–30, 2008.
- [16] T. Osone, J. Tatsuno, T. Nishida, and H. Kobayashi, "Cooperative motion planning for dual arm robot to demonstrate human arm movements," in *Robot and Human Interactive Communication, 2002. Proceedings. 11th IEEE International Workshop on*. IEEE, 2002, pp. 488–493.
- [17] F. Caccavale, C. Natale, B. Siciliano, and L. Villani, "Control of two industrial robots for parts mating," in *Control Applications, 1998. Proceedings of the 1998 IEEE International Conference on*, vol. 1. IEEE, 1998, pp. 562–566.
- [18] —, "Achieving a cooperative behavior in a dual-arm robot system via a modular control structure," *Journal of Robotic Systems*, vol. 18, no. 12, pp. 691–699, 2001.
- [19] T. Wimböck, C. Ott, and G. Hirzinger, "Impedance behaviors for two-handed manipulation: Design and experiments," in *Robotics and Automation, 2007 IEEE International Conference on*. IEEE, 2007, pp. 4182–4189.
- [20] O. Donchin, A. Gribova, O. Steinberg, H. Bergman, and E. Vaadia, "Primary motor cortex is involved in bimanual coordination," *Nature*, vol. 395, pp. 274–278, Sept 1998.
- [21] F. G. Andres, T. Mima, A. E. Schulman, J. Dichgans, M. Hallett, and C. Gerloff, "Functional coupling of human cortical sensorimotor areas during bimanual skill acquisition," *Brain*, vol. 122, no. 5, pp. 855–870, 1999.
- [22] H. Wu, L. Lou, C.-C. Chen, S. Hirche, and K. Kuhnlenz, "Cloud-based networked visual servo control," *Industrial Electronics, IEEE Transactions on*, vol. 60, no. 2, pp. 554–566, feb. 2013.
- [23] Z. Wang and D. Gu, "Cooperative target tracking control of multiple robots," *Industrial Electronics, IEEE Transactions on*, vol. 59, no. 8, pp. 3232–3240, aug. 2012.
- [24] O. Linda and M. Manic, "Fuzzy force-feedback augmentation for manual control of multirobot system," *Industrial Electronics, IEEE Transactions on*, vol. 58, no. 8, pp. 3213–3220, aug. 2011.
- [25] S. Yang, A. Zhu, G. Yuan, and M. Meng, "A bioinspired neurodynamics-based approach to tracking control of mobile robots," *Industrial Electronics, IEEE Transactions on*, vol. 59, no. 8, pp. 3211–3220, aug. 2012.
- [26] S. Rahman, R. Ikeura, S. Hayakawa, and H. Sawai, "Design and control of a power assist system for lifting objects based on human operator's weight perception and load force characteristics," *Industrial Electronics, IEEE Transactions on*, vol. 58, no. 8, pp. 3141–3150, aug. 2011.
- [27] W. Xu, J.-S. Pap, and J. Bronlund, "Design of a biologically inspired parallel robot for foods chewing," *Industrial Electronics, IEEE Transactions on*, vol. 55, no. 2, pp. 832–841, feb. 2008.
- [28] J. Yuan, G. Liu, and B. Wu, "Power efficiency estimation-based health monitoring and fault detection of modular and reconfigurable robot," *Industrial Electronics, IEEE Transactions on*, vol. 58, no. 10, pp. 4880–4887, Oct. 2011.
- [29] O. Linda and M. Manic, "Self-organizing fuzzy haptic teleoperation of mobile robot using sparse sonar data," *Industrial Electronics, IEEE Transactions on*, vol. 58, no. 8, pp. 3187–3195, 2011.
- [30] T. Shibata and T. Murakami, "Power-assist control of pushing task by repulsive compliance control in electric wheelchair," *Industrial Electronics, IEEE Transactions on*, vol. 59, no. 1, pp. 511–520, 2012.
- [31] B. Cai and Y. Zhang, "Different-level redundancy-resolution and its equivalent relationship analysis for robot manipulators using gradient-descent and zhang's neural-dynamic methods," *Industrial Electronics, IEEE Transactions on*, vol. 59, no. 8, pp. 3146–3155, 2012.
- [32] M. Shahbazi, P. Poure, S. Saadate, and M. Zolghadri, "Fault-tolerant five-leg converter topology with fpga-based reconfigurable control," *Industrial Electronics, IEEE Transactions on*, vol. 60, no. 6, pp. 2284–2294, 2013.
- [33] J. Jin, S. Yuen, Y. Lee, C. Jun, Y. Kim, S. Lee, B.-J. You, and N. Doh, "Minimal grasper: A practical robotic grasper with robust performance for pick-and-place tasks," *Industrial Electronics, IEEE Transactions on*, vol. 60, no. 9, pp. 3796–3805, 2013.
- [34] C. Westermayer, R. Priesner, M. Kozek, and R. Bauer, "High dynamic torque control for industrial engine test beds," *Industrial Electronics, IEEE Transactions on*, vol. 60, no. 9, pp. 3877–3888, 2013.
- [35] Y. Maeda and M. Iwasaki, "Initial friction compensation using rheology-based rolling friction model in fast and precise positioning," *Industrial Electronics, IEEE Transactions on*, vol. 60, no. 9, pp. 3865–3876, 2013.
- [36] J. Lee, S. Han, and J. Lee, "Decoupled dynamic control for pitch and roll axes of the unicycle robot," *Industrial Electronics, IEEE Transactions on*, vol. 60, no. 9, pp. 3814–3822, 2013.
- [37] C. Mitsantisuk, S. Katsura, and K. Ohishi, "Force control of human-robot interaction using twin direct-drive motor system based on modal space design," *Industrial Electronics, IEEE Transactions on*, vol. 57, no. 4, pp. 1383–1392, 2010.
- [38] W.-H. Zhu and J. De Schutter, "Control of two industrial manipulators rigidly holding an egg," *Control Systems, IEEE*, vol. 19, no. 2, pp. 24–30, apr 1999.
- [39] J. Szwedczyk, F. Plumet, and P. Bidaud, "Planning and controlling cooperating robots through distributed impedance," *Journal of Robotic Systems*, vol. 19, no. 6, pp. 283–297, 2002.
- [40] J. D. Choi, "Robot and method of controlling cooperative work thereof," U.S. Patent Publication No: US 2009/0287354 A1, Nov. 19 2009.
- [41] P. Chang, D. Kim, and K. Park, "Robust force/position control of a robot manipulator using time-delay control," *Control Engineering Practice*, vol. 3, no. 9, pp. 1255–1264, 1995.
- [42] A. Ejiri, I. Watanabe, K. Okabayashi, M. Hashima, M. Tatewaki, T. Aoki, and T. Maruyama, "Satellite berthing experiment with a two-armed space robot," in *Robotics and Automation, 1994. Proceedings., 1994 IEEE International Conference on*, may 1994, pp. 3480–3487.
- [43] K. Saiki, A. S. R. Liza, S. Toritani, and K. Nonami, "Force sensorless impedance control of dual-arm manipulator-hand system," *Journal of System Design and Dynamics*, vol. 5, no. 5, pp. 953–965, 2011.
- [44] K.-K. Ahn and S.-Y. Yang, "Robust force control of a 6 link electro-hydraulic manipulator," in *Science and Technology, 2000. KORUS 2000. Proceedings. The 4th Korea-Russia International Symposium on*, vol. 3, 2000, pp. 78–83.

- [45] K. Ahn and S. Yokota, "Robust force control of a 6-link electro-hydraulic manipulator," *JSME International Journal Series C Mechanical Systems, Machine Elements and Manufacturing*, vol. 46, no. 3, pp. 1091–1099, 2003.
- [46] K. K. Ahn and S. Yokota, "Design of a robust force control system for an automatic live-line maintenance robot using a force disturbance observer," *Proceedings of the Institution of Mechanical Engineers, Part I: Journal of Systems and Control Engineering*, vol. 218, no. 7, pp. 545–556, 2004.
- [47] M. Jin, S. Kang, and P. Chang, "Robust compliant motion control of robot with nonlinear friction using time-delay estimation," *Industrial Electronics, IEEE Transactions on*, vol. 55, no. 1, pp. 258–269, 2008.
- [48] B. Cao, G. Dodds, and G. Irwin, "Redundancy resolution and obstacle avoidance for cooperative industrial robots," *Journal of Robotic Systems*, vol. 16, no. 7, pp. 405–417, 1999.
- [49] W. Owen, E. Croft, and B. Benhabib, "Stiffness optimization for two-armed robotic sculpting," *Industrial Robot: An International Journal*, vol. 35, no. 1, pp. 46–57, 2008.
- [50] B. Siciliano, L. Sciacicco, L. Villani, and G. Oriolo, *Robotics: modelling, planning and control*. Springer Verlag, 2008.
- [51] W. Newman, "Stability and performance limits of interaction controllers," *Journal of Dynamic Systems, Measurement, and Control*, vol. 114, pp. 563–570, 1992.
- [52] M. Dohring and W. Newman, "The passivity of natural admittance control implementations," in *Robotics and Automation, 2003. Proceedings. ICRA'03. IEEE International Conference on*, vol. 3. IEEE, 2003, pp. 3710–3715.
- [53] J. Craig, *Introduction to Robotics: Mechanics and Control*, 3rd ed. Pearson Education, 2005.
- [54] L. Dozio and P. Mantegazza, "Real time distributed control systems using RTAI," in *Object-Oriented Real-Time Distributed Computing, 2003. Sixth IEEE International Symposium on*. IEEE, 2003, pp. 11–18.
- [55] S. Eppinger, "Modeling robot dynamic performance for endpoint force control," Ph.D. dissertation, MIT, 1988.
- [56] K. S. Fu, R. C. Gonzalez, and C. S. G. Lee, *Robotics: control, sensing, vision, and intelligence*. McGraw-Hill, 1987.
- [57] S. Kang, M. Jin, and P. Chang, "A solution to the accuracy/robustness dilemma in impedance control," *Mechatronics, IEEE/ASME Transactions on*, vol. 14, no. 3, pp. 282–294, 2009.
- [58] P. Chang, B. Park, and K. Park, "An experimental study on improving hybrid position/force control of a robot using time delay control," *Mechatronics*, vol. 6, no. 8, pp. 915–931, 1996.
- [59] J.-J. Slotine, "Robustness issues in robot control," in *Robotics and Automation. Proceedings. 1985 IEEE International Conference on*, vol. 2, Mar. 1985, pp. 656–661.
- [60] M. Jin, J. Lee, P. Chang, and C. Choi, "Practical nonsingular terminal sliding-mode control of robot manipulators for high-accuracy tracking control," *Industrial Electronics, IEEE Transactions on*, vol. 56, no. 9, pp. 3593–3601, 2009.



Jinoh Lee (S'09–M'13) received his B.S. degree in mechanical engineering from Hanyang University, Seoul, South Korea, in 2003, and M.Sc.–Ph.D. degrees in mechanical engineering from Korea Advanced Institute of Science and Technology (KAIST), Daejeon, South Korea, in 2012.

He is currently a Post doctoral Researcher at Istituto Italiano di Tecnologia, Genoa, Italy, and involved in European project, the FP7 ICT-287513 Safe and Autonomous Physical Human-Aware Robot Interaction (SAPHARI). His research interest includes dual-arm dexterous manipulation, robust control of highly nonlinear systems, and compliant robotic system control for safe human-robot interaction.



Pyung Hun Chang (S'86–M'89) received the M.Sc. and Ph.D. degrees both in mechanical engineering from Massachusetts Institute of Technology (MIT), Cambridge, in 1984 and 1987, respectively. He had been a Professor at Korea Advanced Institute of Science and Technology (KAIST), Daejeon, Korea, for 24 years, and now is a Professor and Head of Robotics Engineering Department of Daegu-Gyeongbuk Institute of Science and Technology (DGIST), Daegu, Korea. His current research interests include the rehabilitation robotics, robust control

of nonlinear systems including kinematically redundant manipulators, and impedance control of dual-arm manipulators. He has authored more than 46 papers in international journals, 22 papers in domestic journals, and 88 papers in conference proceedings. Currently, he serves as the Dean of graduate student of DGIST.



Rodrigo S. Jamisola, Jr. (S'97–M'08) received his B.S. degree in mechanical engineering from the University of the Philippines - Diliman, M.E. degree (research-based) in mechanical engineering from the National University of Singapore in 2001, M.Sc. degree in electrical and computer engineering from Colorado State University in 2006, and Ph.D. degree in electronics and communications engineering from De La Salle University - Manila in 2009. He joined De La Salle University as an Asst. Professor in 2008 and Toyota Motor Philippines as R&D Manager in

2011. He is currently a Post-doctoral Research Fellow at Daegu-Gyeongbuk Institute of Science and Technology in South Korea. His research interest includes control of combined manipulators, development of wearable robots, numerical optimization, and human-machine interfaces.

Failure-Tolerant Path Planning for Kinematically Redundant Manipulators Anticipating Locked-Joint Failures

Rodrigo S. Jamisola, Jr., *Student Member, IEEE*, Anthony A. Maciejewski, *Fellow, IEEE*, and Rodney G. Roberts, *Senior Member, IEEE*

Abstract—This work considers kinematic failure tolerance when obstacles are present in the environment. It addresses the issue of finding a collision-free path such that a redundant robot can successfully move from a start to a goal position and/or orientation in the workspace despite any single locked-joint failure at any time. An algorithm is presented that searches for a simply-connected, obstacle-free surface with no internal local minimum or maximum in the configuration space that guarantees the existence of a solution. The method discussed is based on the following assumptions: a robot is redundant relative to its task, only a single locked-joint failure occurs at any given time, the robot is capable of detecting a joint failure and immediately locks the failed joint, and the environment is static and known. The technique is illustrated on a seven degree-of-freedom commercially available redundant robot. Although developed and illustrated for a single degree of redundancy, it is possible to extend the algorithm to higher degrees of redundancy.

Index Terms—Kinematic failure tolerance, locked-joint failures, path planning, redundant manipulators, self-motion manifolds.

I. INTRODUCTION

FAULT-TOLERANT path planning is a motion planning strategy that gives a robot the ability to gracefully accommodate joint failures. This ability enhances safety and reliability for robots carrying out tasks in remote or hazardous environments, such as in space exploration [1], [2], underwater exploration [3], and nuclear waste disposal [4]–[6]. It allows a robot to immediately complete the task at hand without unnecessary delays due to robot repair. It also avoids the potentially significant danger associated with a robot failure during task execution amongst hazardous materials.

A number of studies have been dedicated to the assessment [6], [7] and analysis [5], [8]–[12] of robot safety and reliability, including robots designed primarily for this purpose [13]–[15]. The earliest work on kinematic failure tolerance [16] used the minimum singular value of the manipulator Jacobian matrix as a local worst-case measure of a robot's tolerance to a joint failure. The nature of joint failures that have been studied

include locked-joint [17]–[19] and free-swinging joint failures [20]. A real-time implementation of local kinematic failure tolerance has been demonstrated in [19]. Other studies related to enhancing a robot's tolerance to failure include work on failure detection [21]–[23], low-level failure avoidance and recoverability [24], [25], layered failure tolerance control [26]–[28], failure tolerance by trajectory planning [29], and kinematic failure recovery [30]. In all of these previous studies on kinematic failure tolerance cited above, workspace obstacles were not considered.

Despite the lack of attention that it has received, the presence of obstacles in the environment greatly affects a kinematic failure tolerance algorithm. To our knowledge, the only work to consider obstacles along with failure tolerance was [31]. Their approach allows one to guarantee that a manipulator can avoid obstacles while the end-effector follows a desired workspace path, even in the presence of an arbitrary single locked-joint failure that occurs at any point along the trajectory. Our work is similar in that it allows a manipulator to avoid obstacles in the presence of joint failures, however, it differs in that the task definition is specified as a desired start and goal location in the workspace, as is typical of pick-and-place tasks. This is significant because constraining the end-effector to a specific path will greatly reduce the likelihood that an obstacle-free, failure-tolerant trajectory exists.

The remainder of this paper is organized as follows. An overview of the proposed approach is presented in Section II. Section III states the conditions that guarantee the existence of a solution to the failure-tolerant path-planning problem and then uses these conditions to form the basis of an algorithm. Section IV illustrates the efficacy of the algorithm on a three degree-of-freedom planar robot. A seven degree-of-freedom example is presented in Section V using the Mitsubishi PA-10 robot. Finally, the summary and conclusions of this work are given in Section VI.

II. OVERVIEW OF THE PROPOSED APPROACH

Consider a kinematically redundant manipulator, operating in a failure-prone environment, that must complete a pick-and-place type task in a workspace filled with obstacles. The goal of our work is to generate a family of joint trajectories, each of which would allow the manipulator to avoid obstacles and tolerate any single locked-joint failure as its end effector travels from the given start workspace location to the desired goal location. To achieve this goal, two fundamental issues need to be

Manuscript received December 13, 2005. This paper was recommended for publication by Associate Editor I. Bonev and Editor K. Lynch upon evaluation of the reviewers' comments.

R. S. Jamisola, Jr., and A. A. Maciejewski are with the Department of Electrical and Computer Engineering, Colorado State University, Fort Collins, CO 80523-1373 USA (e-mail: r.jamisola@colostate.edu; aam@colostate.edu).

R. G. Roberts is with the Department of Electrical and Computer Engineering, Florida A&M—Florida State University, Tallahassee, FL 32310-6046 USA (e-mail: rroberts@eng.fsu.edu).

Digital Object Identifier 10.1109/TRO.2006.878959

failure. This will be accomplished by choosing a surface connecting a suitable θ_s to a γ_g . This surface is chosen so that the manipulator will not encounter obstacles and can remain on the surface even if a joint is locked. The conditions for the existence of such a surface, called a *failure surface*, \mathcal{S} , will be derived in the following section.

III. GUARANTEEING A FAILURE-TOLERANT PATH

A. A Necessary Condition and a Sufficient Condition

In the previous section, we described an approach to guarantee failure tolerance in the presence of obstacles using a surface. In this section we will derive conditions concerning the existence of such a surface. The first condition is a necessary condition to determine the suitability of a start configuration, θ_s , based on the ability of the manipulator to reach the γ_g curve with any single joint locked. While θ_s and γ_g are obstacle free, this condition does not take into account the possibility of encountering obstacles on the way, and is thus only a necessary condition. We will see later that this tends to be a strong indicator of the likelihood that such a surface exists. Fortunately it turns out that this is a relatively fast calculation that can easily eliminate cases where no surface exists. The second condition is used to determine the existence of the solution once a feasible θ_s is identified. The proof of this result will motivate an algorithm for calculating a suitable surface. Such a surface cannot have a local minimum or maximum in any of its θ_i components.

The necessary condition is given in terms of the failure hyperplanes associated with θ_s . Given \mathbf{x}_s and \mathbf{x}_g , the manipulator can reach γ_g when joint i is locked at θ_s provided that the corresponding failure hyperplane of θ_s intersects γ_g , that is, $\mathbf{H}_i(\theta_s) \cap \gamma_g \neq \emptyset$. Physically this means that the resulting failure-induced C-space due to a locked joint i failure at θ_s contains at least a point of γ_g . This indicates the possibility of reaching \mathbf{x}_g despite a locked-joint failure at θ_s . Thus, to guarantee that the robot will reach γ_g from θ_s for any locked-joint failure, it is necessary that each of the n failure hyperplanes, $\mathbf{H}_i(\theta_s)$, intersects the γ_g curve. This motivates the definition of a feasible start configuration θ_s when all of its corresponding failure hyperplanes intersect γ_g . This proposition is formally stated as a necessary condition.

Proposition 1 (Necessary Condition): A necessary condition for a given obstacle-free start configuration, θ_s , to be a feasible start configuration is that all of the corresponding failure hyperplanes of θ_s intersect a continuous, obstacle-free portion of the goal self-motion manifold, γ_g , that is

$$\mathbf{H}_i(\theta_s) \cap \gamma_g \neq \emptyset \quad \text{for all } i = 1, \dots, n. \quad (4)$$

After a feasible θ_s has been identified, its corresponding $\gamma_g(v)$ defines the bounds of a failure hypercuboid, \mathbf{V} . If there were no obstacles in the workspace, then the identification of \mathbf{V} is sufficient to guarantee that a given robot can successfully reach \mathbf{x}_g from θ_s for any single locked-joint failure at any time by keeping its configurations within \mathbf{V} as the given robot approaches \mathbf{x}_g . When obstacles are present in the workspace, some regions of \mathbf{V} may no longer be available. The problem

now becomes that of searching for a solution set within \mathbf{V} that can guarantee successful completion. This will be accomplished by generating an obstacle-free surface connecting θ_s to the γ_g curve in such a way that the manipulator can continue to move along the surface to γ_g in spite of any single locked-joint failure. When a joint is locked the manipulator is constrained to be on a corresponding hyperplane. Therefore, the intersection of that hyperplane with the surface needs to connect with γ_g . The surface must satisfy a monotonicity property in the following sense. Consider locking joint i . As the value at which joint i is locked varies, this determines a contour-like plot in which θ_i is analogous to the height. The different contours represent the manipulator's motion along the surface with its i th joint locked at different fixed values. In order for a manipulator to be able to reach its goal for any locked-joint failure, no closed contours can exist. Therefore, the surface cannot have any local internal minimum or maximum with respect to any θ_i . This monotonicity condition is captured by the following theorem.

Theorem 1 (Sufficient Condition): Let \mathcal{S} be an obstacle-free, two-dimensional, simply-connected surface in \mathbb{R}^n . Suppose $\mathcal{S} = \{\mathbf{S}(u, v) | u, v \in [0, 1]\}$ is the image of a continuous function $\mathbf{S} : [0, 1] \times [0, 1] \rightarrow \mathbb{R}^n$ that is continuously differentiable in its interior and that $\mathbf{S}(u, v)$ has the following properties:

- i) $\mathbf{S}(0, v) = \theta_s$ for all $v \in [0, 1]$;
- ii) $\mathbf{S}(1, v) = \gamma_g(v)$ for all $v \in [0, 1]$ where $\gamma_g(v)$ is a smooth connected curve;
- iii) For a fixed $v \in [0, 1]$ and a fixed integer $i = 1, 2, \dots, n$, the i th component $S_i(u, v)$ of $\mathbf{S}(u, v)$ is either a strictly monotonic function of u such that $\partial S_i / \partial u \neq 0$ for $0 < u < 1$ or, in the case when $\gamma_{gi}(v) = \theta_{si}$, a constant with respect to u .

Furthermore, assume that any point θ on \mathcal{S} satisfies

$$\min_{0 \leq v \leq 1} \gamma_{gi}(v) \leq \theta_i \leq \max_{0 \leq v \leq 1} \gamma_{gi}(v), \quad \text{for } i = 1, 2, \dots, n.$$

Then given any point θ_0 on \mathcal{S} and any integer $i = 1, 2, \dots, n$, there is a curve $\theta : [0, 1] \rightarrow \mathbb{R}^n$ lying entirely on \mathcal{S} that connects θ_0 to a point θ_1 on the curve $\gamma_g(v)$ such that $\theta_i(t) = \theta_{0i}$ for all $t \in [0, 1]$.

Proof: The result will be proven by constructing a suitable curve. Fix $i \in \{1, 2, \dots, n\}$. Given $\theta_0 \in \mathcal{S}$, there is a pair (u_0, v_0) such that $\mathbf{S}(u_0, v_0) = \theta_0$. By assumption (iv), $\gamma_{gi}(v_1) = \theta_{0i}$ for some $v_1 \in [0, 1]$ where we assume v_1 is the closest such value to v_0 . We need to show that there is a curve $\theta : [0, 1] \rightarrow \mathbb{R}^n$ such that $\theta(0) = \theta_0$, $\theta(1) = \mathbf{S}(1, v_1)$, and $\theta_i(t) = \theta_{0i}$ for all $t \in [0, 1]$.

The problem is trivial if θ_0 is on the γ_g curve. Assuming that it is not, we consider three cases. First, suppose that $\theta_0 = \theta_s$. Then $\gamma_{gi}(v_1) = \theta_{si}$ and by assumption (iii) the curve $\theta(t) = \mathbf{S}(t, v_1)$ is a suitable curve. Next, consider the case when $\theta_0 \neq \theta_s$ but $\theta_{0i} = \theta_{si}$. Then $u_0 \neq 0$ but $S_i(u_0, v_0) = S_i(u_0, v_0)$ so that $S_i(u, v_0)$ is not strictly monotonic in u . But, by assumption (iii), this implies that $S_i(u, v_0) = \theta_{si}$ for $0 \leq u \leq 1$. This gives a suitable curve $\theta(t) = \mathbf{S}(u_0(1-t) + t, v_0)$.

Lastly, consider the case when $\theta_{0i} \neq \theta_{si}$. The goal is to determine a trajectory $\mathbf{w}(t) = [u(t) \ v(t)]^T$, $0 \leq t \leq 1$, going from $\mathbf{w}_0 = [u_0 \ v_0]^T$ to $\mathbf{w}_1 = [1 \ v_1]^T$ while keeping $S_i(u(t), v(t)) = \theta_{0i}$ constant. Since the domain is compact, this

can be done by applying an inverse velocity kinematics type algorithm to the system

$$\mathbf{z} = \begin{bmatrix} z_1 \\ z_2 \end{bmatrix} = \mathbf{g}(\mathbf{w}) = \begin{bmatrix} v \\ S_i(u, v) \end{bmatrix} \quad (5)$$

to find a suitable trajectory $(u(t), v(t))$ provided, of course, that the Jacobian of \mathbf{g}

$$\mathbf{G} = \frac{\partial \mathbf{g}}{\partial \mathbf{w}} = \begin{bmatrix} 0 & 1 \\ \frac{\partial S_i}{\partial u} & \frac{\partial S_i}{\partial v} \end{bmatrix} \quad (6)$$

does not become singular along the way. However, by assumption (iii), the determinant of \mathbf{G} , which is equal to $-\partial S_i / \partial u$, is zero only when $S_i(u, v) = \theta_{si}$. This never occurs along the trajectory as $S_i(u(t), v(t)) \neq \theta_{si}$ is fixed. We can therefore generate a trajectory $(u(t), v(t))$ such that

$$\mathbf{z}(t) = \begin{bmatrix} v_0(1-t) + v_1 t \\ \theta_{0i} \end{bmatrix}, \quad 0 \leq t \leq 1. \quad (7)$$

To finish off the proof, we need to show that $u(t)$ stays on the interval $[0, 1]$ throughout the trajectory and ends at 1. We do this by first showing that $u(t)$ cannot be 1 or 0 for $0 \leq t < 1$ and then using an argument concerning the monotonicity of S_i with respect to u to show that $u(1)$ must be 1. The case $u(t) = 0$ for some $0 \leq t < 1$ violates the assumption that $\theta_{0i} \neq \theta_{si}$ while the case $u(t) = 1$ for some $0 \leq t < 1$ violates the assumption that v_1 is the closest v -value to v_0 such that $\gamma_{gi} = \theta_{0i}$. Since $S_i(u(t), v(t)) = \theta_{0i}$ on the trajectory, we have that $S_i(u(1), v_1) = \theta_{0i} = \gamma_{gi}(v_1) = S_i(1, v_1)$ so that by assumption (iii), $u(1) = 1$. We thus have a suitable curve $\boldsymbol{\theta}(t) = \mathbf{S}(u(t), v(t))$. ■

Thus, the monotonicity of paths from $\boldsymbol{\theta}_s$ to $\boldsymbol{\gamma}_g(v)$ guarantees that after a single locked-joint failure, the given robot will not get stuck in the vicinity of an internal local minimum or maximum and will reach a point on $\boldsymbol{\gamma}_g(v)$. By specifying only the start and goal locations for pick and place tasks in the presence of obstacles, the solution being presented provides some flexibility in choosing the obstacle-free, failure-tolerant path towards the goal based on some desired optimization criteria prior to a failure. After a failure, there would exist a finite number of feasible paths. When there is more than one feasible path the shortest path towards the goal, for example, could be chosen.

Theorem 1 motivates the method for identifying a failure surface in the algorithm by generating monotonic paths from $\boldsymbol{\theta}_s$ to $\boldsymbol{\gamma}_g(v)$. Note that this theorem is only a sufficient condition and can only guarantee task completion when the failure surface exists. When the failure surface identification is unsuccessful, a solution may still be present.

B. An Algorithm

The procedure for implementing failure-tolerant path planning with obstacle avoidance is enumerated in the following.

- 1) Determine the start self-motion manifold, \mathcal{M}_s , and goal self-motion manifold, \mathcal{M}_g , from the given start, \mathbf{x}_s , and goal, \mathbf{x}_g , workspace position and/or orientation, respectively.
- 2) Identify an obstacle-free start configuration, $\boldsymbol{\theta}_s$, and an obstacle-free portion of the goal self-motion manifold, $\boldsymbol{\gamma}_g$. Those portions of the self-motion manifold that are outside

the joint limits are treated in the same manner as configurations corresponding to collisions with obstacles. Thus, by obstacle-free configurations we mean those configurations that are not in collision with obstacles and are within the joint limits.

- 3) Check for intersections of the failure hyperplane $\mathbf{H}_i(\boldsymbol{\theta}_s)$ with $\boldsymbol{\gamma}_g$ for $i = 1, \dots, n$. (Note that this step uses the necessary condition in Section III-A.) This check, although in a different form, was also performed in [18] and [31].
- 4) Check for the existence of a failure surface, \mathcal{S} . This is performed by generating monotonic paths from the feasible $\boldsymbol{\theta}_s$ to points on $\boldsymbol{\gamma}_g(v)$ and checking for intersections with obstacles.¹ (This step utilizes the sufficient condition in Section III-A.)

The computational complexity of the proposed algorithm is highly dependent on the method used for computing the start and goal self-motion manifolds, and the method used for collision detection. For $r = 1$, the computational complexity is $O(mn^2) + O(mnp)$ where p is the number of obstacles in the workspace. The first term corresponds to the computation of the self-motion manifolds, while the second term is due to collision detection.

For higher degrees of redundancy, a $\boldsymbol{\gamma}_g$ curve would need to be identified in the corresponding higher dimensional goal self-motion manifold. This is done by first identifying the obstacle-free intersections of the manifold with all of the failure hyperplanes $\mathbf{H}_i(\boldsymbol{\theta}_s)$ for $i = 1, \dots, n$. If the goal self-motion manifold does not intersect each \mathbf{H}_i , then no $\boldsymbol{\gamma}_g$ can exist. The next step is to connect one point from each failure hyperplane intersection. Two failure hyperplane points are connected by generating a path along the self-motion manifold, e.g., by using the null vectors from the Jacobian, along with a term to avoid obstacles. If all intersection points can be connected with such obstacle-free paths that lie in the goal self-motion manifold, then the resulting connected curves represent a suitable $\boldsymbol{\gamma}_g$.

C. Generating Monotonic Surfaces

1) *Monotonic Curves:* Parametric monotonic quadratic polynomials $p(u)$ are used to generate a family of paths from $\boldsymbol{\theta}_s$ to $\boldsymbol{\gamma}_g$. These paths are chosen to form an obstacle-free, continuously differentiable surface \mathcal{S} satisfying the conditions of Theorem 1.

It is easy to see that any quadratic polynomial $p_i(u)$ satisfying the constraints $p_i(0) = \theta_{si}$ and $p_i(1) = \theta_{gi}$ has the form

$$p_i(u) = \theta_{si}(1-u) + \theta_{gi}u + \alpha_i u(1-u) \quad (8)$$

where the parameter α_i can be any real number and θ_{gi} denotes the i th component of $\boldsymbol{\theta}_g$. Although α_i does not affect the values at the end-points, it does completely characterize whether the polynomial is monotonic or not. To see this, note that a polynomial is monotonic on the closed interval $[0, 1]$ if and only if its derivative does not change sign on the open interval $(0, 1)$. Since the derivative of a quadratic polynomial represents the equation of a line, it follows that one only needs to check the endpoints of the interval $[0, 1]$ to determine the set of α_i 's that

¹Note that the obstacles must be grown in order to guarantee that no collision can exist between curves.

makes (8) monotonic on $[0,1]$. Therefore, for (8) to be monotonic on $[0,1]$, $p'_i(0) = \theta_{gi} - \theta_{si} + \alpha_i$ and $p'_i(1) = \theta_{gi} - \theta_{si} - \alpha_i$ should not have opposite signs. This is clearly true if and only if $|\alpha_i| \leq |\theta_{gi} - \theta_{si}|$.

2) *Monotonic Surfaces*: Equation (8) can be used to determine a failure surface \mathcal{S} described by

$$\mathbf{S}(u, v) = \boldsymbol{\theta}_s(1 - u) + \boldsymbol{\theta}_g u + \boldsymbol{\alpha}(v)u(1 - u). \quad (9)$$

Suitable values for $\alpha_i(v)$ are determined for discrete values of $v = k\delta v$ along the $\boldsymbol{\gamma}_g(v)$ curve. These values are then connected so that $\alpha_i(v)$ has first-order continuity. The region between the monotonic paths determined by $\alpha_i(k\delta v)$ can be guaranteed to be collision free if the obstacles are suitably enlarged prior to computing the monotonic quadratic curves. One must also check that the monotonicity condition $|\alpha_i| \leq |\theta_{gi} - \theta_{si}|$ continues to hold in between the discrete values $v = k\delta v$. With this choice of $\alpha_i(v)$, the conditions of Theorem 1 are satisfied so that \mathcal{S} is a suitable failure surface.

3) *Trajectory Generation*: Once a monotonic surface is pre-computed, trajectory generation for the robot is very computationally efficient. Specifically, the robot starts from configuration $\boldsymbol{\theta}_s$ and its trajectory is generated by following a desired path on the surface given by a fixed value of the parameter v by evaluating the quadratic $\mathbf{S}(u, v = v_d)$ for successively increasing values of u . If a failure occurs in joint f at $\mathbf{S}(u_0, v_0)$ while the robot is moving, then, in general, it will no longer be possible to follow the same curve because S_f must remain constant. The trajectory to reach the desired goal workspace location is now computed by solving the quadratic $S_f(u_0, v_0) = S_f(u_0 + \delta u, v)$ for the value of v that will keep the trajectory on the surface. The value of δu is incremented until $u_0 + \delta u = 1$ at which point the robot will be at the desired workspace location.

IV. 3-DOF PLANAR ROBOT EXAMPLE

A 3-DOF planar robot with equal link lengths of 100 units was first used to explore the feasibility of the proposed approach. The workspace contained a number of circular obstacles, each of a diameter of 40 units, where the number of obstacles was varied from zero to twenty in two-obstacle increments. For each number of obstacles, experiments were performed for 1000 randomly generated scenarios, where a scenario consists of a given start workspace location, a given goal workspace location, and the specified locations of the obstacles. In each scenario, the locations for the corresponding number of obstacles are randomly selected from a uniform distribution throughout the entire robot workspace. The start workspace location, \mathbf{x}_s , is randomly selected from a uniform distribution of $[100, 200]$ along the x -axis, that is, at a distance that corresponds to between one and two-link lengths away from the robot base. The goal workspace location, \mathbf{x}_g , is randomly selected to be within a range of $[0, 200]$ units from the range of start workspace locations (while restricting the goal to be within the reachable workspace of the manipulator). Fig. 2 presents an example of the start and goal locations generated for one thousand scenarios.

Five examples from the set of 11 000 scenarios are presented in Fig. 3 where the number of obstacles is varied from 20 to 12

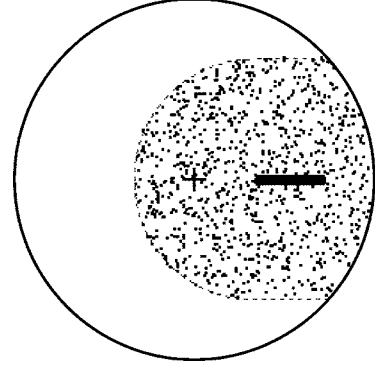


Fig. 2. Workspace of a 3-DOF planar manipulator used for the simulation experiments (all three link lengths are 100 units long). The 1000 start locations, \mathbf{x}_s , are randomly generated within the range $[100, 200]$ units along the x -axis (shown as a thick bold line). The 1000 goal workspace locations, \mathbf{x}_g , (shown as dots) are randomly generated to be within the range $[0, 200]$ units away from the range of start locations (but inside the reachable workspace). The center of the workspace is marked with a bold cross, the workspace boundary with a solid line, and the boundary of the goal locations with a dashed line.

in two-obstacle decrements. In all cases shown, the failure-tolerant, path-planning algorithm was able to identify a failure surface, \mathcal{S} . The manipulator configuration shown in each scenario is the feasible starting configuration, $\boldsymbol{\theta}_s$, that was determined by the algorithm. To illustrate the difficulty of these problem scenarios, the shaded regions identify locations in the workspace where even a single obstacle will prevent the existence of a set of collision-free monotonic curves.

Table I shows the values of the start configuration $\boldsymbol{\theta}_s = [\theta_{s1}, \theta_{s2}, \theta_{s3}]^T$ corresponding to the scenarios in Fig. 3. The failure plane $\mathbf{H}_i(\boldsymbol{\theta}_s)$ intersects the continuous, obstacle-free goal self-motion manifold $\boldsymbol{\gamma}_g$ at $\boldsymbol{\theta}_{Hi} = [\theta_{Hi1}, \theta_{Hi2}, \theta_{Hi3}]^T$ where $i = 1, 2, 3$. Fig. 4 shows projections of the self-motion manifolds in C-space for the scenarios of Fig. 3(a)–(c) where a failure surface exists. The cross on a self-motion manifold denotes the feasible start configuration, $\boldsymbol{\theta}_s$, for the corresponding scenario. The $\boldsymbol{\gamma}_g(v)$ that satisfied the necessary condition is the curve on the self-motion manifold between the points labeled “0” and “1”. The web-like network of paths represents the failure surface for each of the corresponding scenarios. In the following subsections, data gathered from these 11 000 simulation experiments will be presented according to the order in which these steps are performed in the algorithm described in Section III-B. To illustrate the effects of joint limits, an additional 11 000 scenarios were performed with $-135^\circ \leq \theta_1 \leq 135^\circ$, $-90^\circ \leq \theta_2 \leq 90^\circ$, and $-135^\circ \leq \theta_3 \leq 135^\circ$. In all cases the algorithm was executed on a computer with dual Intel Xeon processors running at 2.4 GHz.

A. Computation of Self-Motion Manifolds

The first step in the failure-tolerant, path-planning algorithm is to compute the self-motion manifold(s) for both the start and goal workspace locations. These are computed by identifying a single configuration on each disjoint manifold and then stepping along the manifold (in two degree increments) by integrating the null vector of the manipulator Jacobian matrix (which corresponds to the tangent of the self-motion manifold). The average lengths for the sum of all manifolds corresponding to a

TABLE I
SET OF FEASIBLE, OBSTACLE-FREE START CONFIGURATIONS, θ_s 's, SHOWN IN FIG. 3 WITH THE CORRESPONDING FAILURE PLANES $H_i(\theta_s)$ INTERSECTING A CONTINUOUS, OBSTACLE-FREE PORTION OF THE GOAL SELF-MOTION MANIFOLD, $\gamma_g(v)$, SHOWN IN UNITS OF DEGREES

Fig. 3	Feasible Start Conf., θ_s			Failure Plane $H_i(\theta_s)$ Intersecting $\gamma_g(v)$								
	θ_{s1}	θ_{s2}	θ_{s3}	θ_{H11}	θ_{H12}	θ_{H13}	θ_{H21}	θ_{H22}	θ_{H23}	θ_{H31}	θ_{H32}	θ_{H33}
(a)	-7.3	123.2	-166.5	-6.3	173.8	-128.9	39.3	123.1	-174.2	32.1	155.5	-168.3
(b)	38.0	-126.9	111.5	36.3	-155.6	163.0	26.6	-126.8	171.4	-43.6	62.4	110.3
(c)	-64.7	61.8	75.9	-65.8	60.9	140.7	-71.6	63.6	136.0	102.2	164.4	77.1
(d)	4.5	-90.0	152.3	4.0	66.1	104.1	73.6	-88.3	170.2	47.5	8.5	150.5
(e)	-71.6	75.3	58.5	-69.9	160.5	-2.7	-7.2	76.9	96.0	-40.8	114.9	57.1

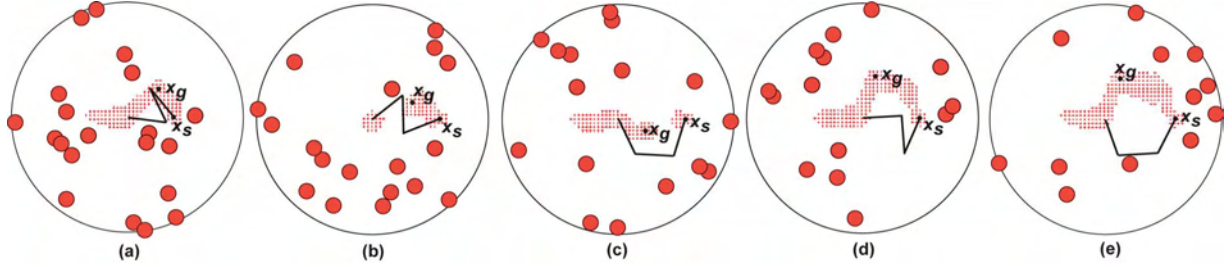


Fig. 3. Five examples selected from the 11 000 scenarios where the failure-tolerant, path-planning algorithm was applied to a 3-DOF planar manipulator. The scenarios correspond to workspaces containing from 20 to 12 obstacles where both the necessary and the sufficient conditions were satisfied. The shaded region in each scenario represents an area where a single obstacle will eliminate any possible monotonic curve connecting a θ_s to its corresponding θ_g . (Color version available online at: <http://ieeexplore.ieee.org>.)

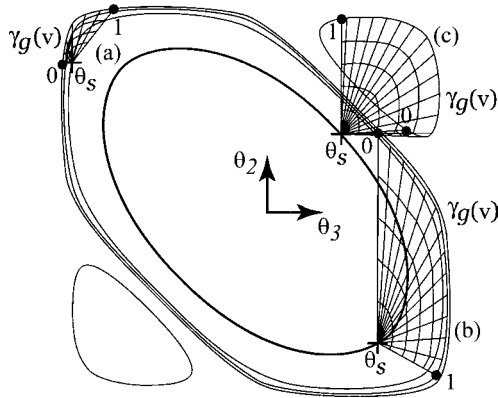


Fig. 4. Projections of the self-motion manifolds on the $\theta_2\theta_3$ -plane for the scenarios of Fig. 3(a)–(c). The failure surface, \mathcal{S} , is shown as a web-like network of paths. The feasible θ_s is shown as a cross on the self-motion manifold while the $\gamma_g(v)$ is the curve on the self-motion manifold between the points labeled “0” and “1”. For the example shown in Fig. 3(c), the goal manifold consists of two disjoint manifolds in the C-space because x_g is less than one link length away from the robot base.

TABLE II
COMPUTATION OF SELF-MOTION MANIFOLDS

	Ave.	Std. Dev.
Length of \mathcal{M}_s (deg)	1043.95	4.97
Length of \mathcal{M}_g (deg)	883.71	8.52
Time to compute $\mathcal{M}_s, \mathcal{M}_g$ (ms)	41.90	5.88

workspace location are given in Table II. The length for the start manifolds are larger than those for the goal manifold because the start workspace locations were intentionally restricted to a region of the workspace where these manifolds are larger, and thus, the locations are more failure tolerant [18]. (A distance of one link length from the base is optimally failure tolerant, i.e.,

Percent of Manifolds that are Reachable and Obstacle Free

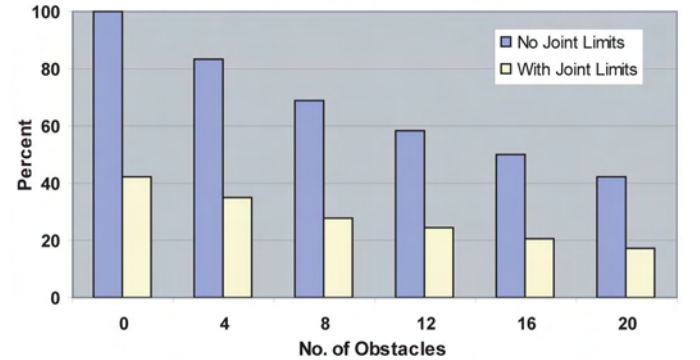


Fig. 5. Percent of the self-motion manifolds that are reachable and obstacle free for a 3-DOF manipulator with and without joint limits. (Color version available online at: <http://ieeexplore.ieee.org>.)

all joints span their entire range of motion, while the locations on the workspace boundary are most failure intolerant, i.e., their self-motion manifolds consist of a single point.) The average computation time over all manifolds was 41.9 ms.

B. Identifying Obstacle-Free Portions of \mathcal{M}_s and \mathcal{M}_g

The next step is to determine the obstacle-free portions of the manifolds. This identifies candidate feasible, obstacle-free start configurations, θ_s , and continuous, obstacle-free portions of the goal self-motion manifold, γ_g , that can possibly satisfy the necessary condition.

Fig. 5 shows the percentage of the start self-motion manifold, \mathcal{M}_s , and goal self-motion manifold, \mathcal{M}_g , that are reachable and obstacle free as a function of the number of obstacles in the workspace. As expected, the percentage of the obstacle-free self-motion manifold decreases as the number of workspace obstacles increases. The time required to determine which portions

TABLE III
COMPUTATION TO CHECK THE NECESSARY CONDITION (N.C.)

No. of Obs.	Time N.C. Sat. (ms)	Time N.C. Not Sat. (ms)	% Cases N.C. Sat.	% \mathcal{M}_s N.C. Sat.
0	0.73	4.39	72.0	25.4
2	0.84	4.59	65.5	20.5
4	1.13	5.03	60.6	16.5
6	1.13	4.86	55.5	15.4
8	1.05	4.57	49.2	12.4
10	1.33	5.13	47.1	10.0
12	1.48	5.35	37.3	7.6
14	1.50	5.43	35.4	6.3
16	1.84	6.15	31.3	5.9
18	1.90	5.56	28.7	4.1
20	2.92	5.53	24.1	3.7

of a manifold are obstacle free is proportional to the number of obstacles by a proportionality constant of 16.5 ms/obstacle.

In many cases, one could avoid most of the computation time associated with checking the entire manifold for collisions with obstacles by performing the necessary condition check first, and then verifying that the start configuration and the corresponding portion of the goal self-motion manifold are collision free.

C. Checking the Necessary Condition

Table III presents the computational data associated with checking the necessary condition. As the number of obstacles in the workspace increases, the percentage of cases that satisfy the necessary condition decreases, reaching a minimum of 24% for the case with twenty obstacles (10% if joint limits are included). For those cases where a θ_s satisfied the necessary condition, we further processed the start manifold to see what percentage of the start manifold would be able to satisfy the necessary condition. (This is not required by the algorithm and the time required to perform this computation was not included in the overall execution time data presented.) Table III shows that this is also a monotonically decreasing function of the number of obstacles in the workspace. Thus, it becomes increasingly more time consuming to identify a θ_s that satisfies the necessary condition as the number of obstacles in the workspace increases. This is illustrated by the fact that the computation time is a monotonically increasing function of the number of obstacles. This is true despite the fact that there is less and less of the start manifold that is obstacle free (see Fig. 5) because an increasingly smaller percentage of the obstacle-free manifold is able to satisfy the necessary condition. In contrast, the time to compute that the necessary condition is not satisfied is relatively independent of the number of obstacles. This at first appears anomalous because one would expect this to be a monotonically decreasing function due to a smaller percentage of the start manifold needing to be checked (because less of it is obstacle free). However, this is offset by the fact that larger and larger manifolds are now failing the necessary condition, thus keeping the computation time relatively constant.

Fig. 6 shows the average length of the $\gamma_g(v)$ from a $\{\theta_s, \gamma_g\}$ pair that satisfies the necessary condition. This generally decreases as the number of obstacles increases due to the fact that it

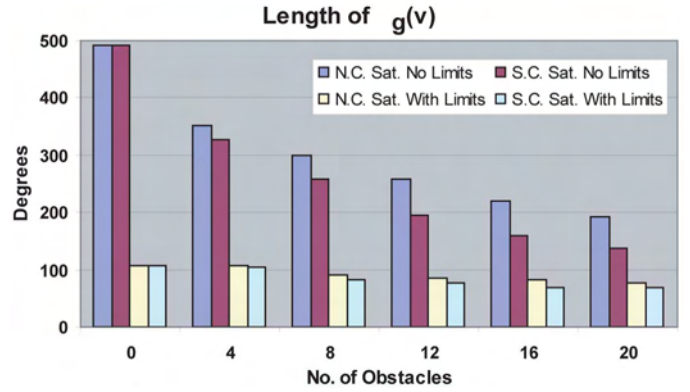


Fig. 6. Average length of a $\gamma_g(v)$ that satisfies the necessary condition (N.C.) and that also satisfies the sufficient condition (S.C.) as a function of the number of obstacles in the workspace. The trends are the same for cases with and without joint limits. (Color version available online at: <http://ieeexplore.ieee.org>.)

is more difficult to have a large $\gamma_g(v)$ because they are required to be obstacle free. The size of a $\gamma_g(v)$ that satisfies the necessary condition is correlated to the distance between the start and goal workspace locations so that, as expected, start and goal locations must be closer together as more and more obstacles are added to the workspace.

D. Computing a Failure Surface

The final step in the algorithm is to check the sufficient condition by attempting to compute a failure surface that guarantees the existence of a solution to the failure-tolerant, path-planning problem. Once a feasible θ_s is found from the previous step, the search for a failure surface begins. A failure surface is identified by generating monotonic paths that connect a feasible θ_s to points on its corresponding $\gamma_g(v)$ that satisfies the necessary condition. (The $\gamma_g(v)$ curve is discretized at a resolution of two degrees.) For each point on $\gamma_g(v)$ the algorithm first attempts to use a straight-line path. If this path is not obstacle free, then it attempts to find a monotonic quadratic path that is obstacle free up to a desired resolution of α_i in (8). If no such path can be found then the algorithm discards this $\{\theta_s, \gamma_g\}$ pair and uses the next $\{\theta_s, \gamma_g\}$ pair that satisfies the necessary condition. If all such pairs are exhausted without completing a failure surface then the algorithm terminates with a message that it was unsuccessful.

It is interesting to note that once the necessary condition is satisfied, it is highly likely that a failure surface will be found, i.e., this occurs 84% of the time. In addition, this percentage is relatively independent of the number of obstacles that are in the workspace as illustrated in Fig. 7 (except, of course, for the case of no obstacles). This is fortuitous, because the construction of failure surfaces is by far the most time consuming portion of the algorithm. The average time for computing a failure surface as a function of the number of obstacles is given in the second column of Table IV. The overall average time was 1.5 s with the maximum time to compute a failure surface over all scenarios was 78.0 s. Similarly, it takes on average 1.8 s to exhaust all possible candidates in cases where a surface cannot be found, with a maximum time of 66.7 s. Thus, the time to evaluate surfaces is seldom wasted, with the majority of the cases where no solution exists being identified in a matter of milliseconds by the necessary condition test.

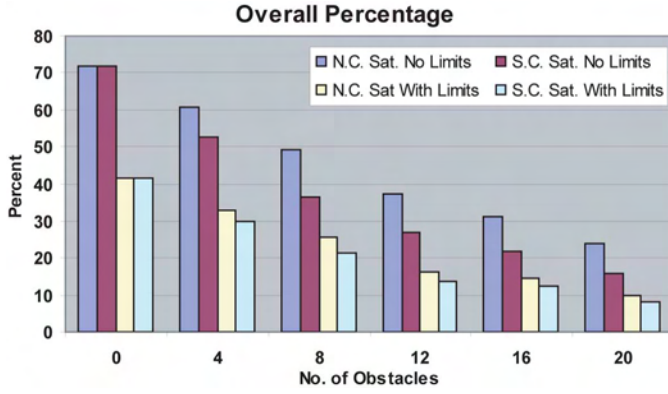


Fig. 7. Percent of total cases where the necessary condition (N.C.) is satisfied and percent of total cases where the sufficient condition (S.C.) is satisfied, i.e., where a failure surface \mathcal{S} is found. The trends are the same for cases with and without joint limits. (Color version available online at: <http://ieeexplore.ieee.org>.)

TABLE IV
COMPUTATIONS WHEN \mathcal{S} IS FOUND

No. of Obs.	Overall Time (s)			No. of Path Evaluations			Diff.
	L+Q	(L+Q)*	L	L+Q	(L+Q)*	L	
0	0.04	0.04	0.04	246	246	246	0
2	0.35	0.34	0.41	658	651	755	5
4	0.78	0.75	0.75	818	793	800	4
6	1.16	1.10	1.07	844	793	752	4
8	1.49	1.42	1.32	818	778	718	2
10	1.77	1.61	1.35	775	698	569	5
12	2.19	2.21	1.78	815	823	630	8
14	2.28	2.26	1.62	718	709	481	2
16	2.68	2.49	1.90	743	682	496	5
18	2.15	2.16	1.72	503	505	379	4
20	1.89	1.87	1.40	381	376	257	1

Because monotonic path generation represents the most time consuming portion of the algorithm, an additional analysis was performed to determine the number and computational cost of linear paths versus quadratic paths. The data from this analysis is presented in Table IV where “L” denotes that only linear paths were tried by the algorithm, “L+Q” denotes that both linear and quadratic paths were tried, and “(L+Q)*” represents the subset of “L+Q” scenarios that correspond to cases where the “L” algorithm was also able to compute a failure surface. It is interesting to note that nearly all (99.6%) of the paths in failure surfaces are linear. Furthermore, the number of additional failure surfaces that are identified when trying quadratic paths is minimal, i.e., always less than 1% (see the last column in Table IV). Given that the use of quadratic paths results in higher execution times (this is true for all cases except for four or fewer obstacles) and a minimal improvement in the number of failure surfaces being identified, the benefit of implementing higher order, monotonic paths is questionable.

E. Comparison to Previous Approaches

It is interesting to compare the results of our approach with that in [31]. Both approaches are similar in that the set of monotonic curves generated by the algorithm presented here

plays the same role as the connectivity graph in [31]. However, any workspace trajectory generated by a path through the connectivity graph will result in the same end-effector trajectory because this is required by the problem definition in [31]. While this is appropriate for tasks that must have the end-effector follow a prescribed trajectory, it limits the number of possible choices for failure-tolerant trajectories if the robot is only required to perform a pick-and-place type operation. The method proposed here will produce an infinite number of possible obstacle-free, failure-tolerant paths from the start to the goal² because it does not constrain the end-effector trajectory.

Fig. 8 illustrates the broad range of end-effector trajectories that are failure tolerant if the task is only constrained to a desired start and goal location rather than a complete trajectory. Each of the subfigures (a)–(e) show the mapping of a set of failure-tolerant, monotonic curves in the configuration space to the workspace for the same start and goal location. Clearly, relaxing the constraint on the end-effector trajectory makes it much more likely that a collision-free, failure-tolerant path will exist.

V. SEVEN DOF REDUNDANT ROBOT EXAMPLE

The proposed failure tolerant path-planning algorithm was also implemented for the Mitsubishi PA-10 seven degree-of-freedom manipulator because it is the most common commercially available redundant robot. Unfortunately, the PA-10 is not a fully kinematically failure-tolerant robot because the null space component of joint four is identically zero, i.e.,

$$\hat{n}_{J4} = 0 \quad (10)$$

throughout the entire C-space. Physically, this is due to the fact that joint four is the only joint that can alter the distance between the wrist and the shoulder, which is why the PA-10 is intolerant to a failure in this joint.³ Therefore, for this example we will assume that there will be no failure in joint four and consider planning a failure-tolerant path for the remaining six joints. For this example, we do not consider joint limits or self-collisions.

A total of 12 000 randomly generated scenarios were performed on the PA-10 where spherical obstacles with a diameter of 0.254 m (10 in) are randomly placed in the robot’s workspace. The number of obstacles was varied from zero to ten such that 2000 experiments were performed for each number of obstacles. The range of desired workspace locations is constrained in x and y to $[-0.8, 0.8]$ m and in z to $[0, 0.8]$ m. It is further specified that the distance of the resulting position from the base of the robot be in the range of $[0.3, 0.8]$ m. Thus, the volume where the workspace positions are randomly picked consists of a hemisphere with an inner radius of 0.3 m and outer radius of 0.8 m. It is in this range of positions where the excursion of the self-motion manifolds for the PA-10 are relatively large. For simplicity, the end-effector is considered to be at the wrist so that no restrictions on orientation are required. The results of the experiments are shown in Fig. 9. These results are very similar to the 3-DOF

²The specific trajectory that the robot follows can then be selected based on some secondary criterion.

³There are a number of different measures that can be used to quantify global fault tolerance based on the maximum excursion of a joint as it spans the self-motion manifold. See [34] for several such measures.

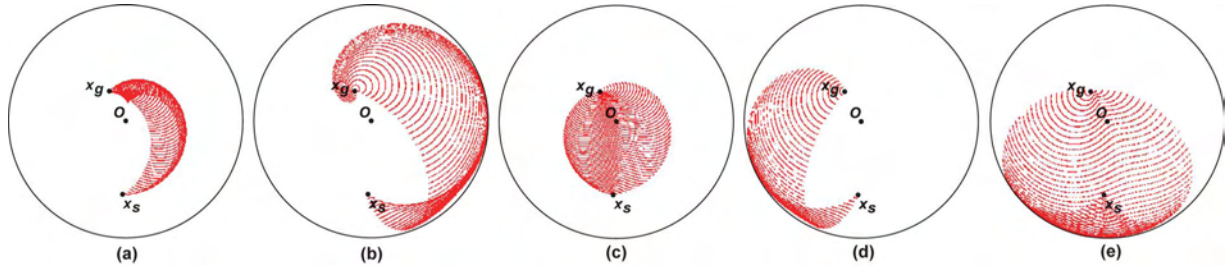


Fig. 8. Subfigures (a)–(e) have the same start and goal workspace locations where $\mathbf{x}_s = [-8.8, -18.8]^T$ and $\mathbf{x}_g = [-42.5, 76.8]^T$. The shaded regions represent the end-effector locations corresponding to different sets of monotonic curves that will take the end-effector from \mathbf{x}_s to \mathbf{x}_g . (Color version available online at: <http://ieeexplore.ieee.org>.)

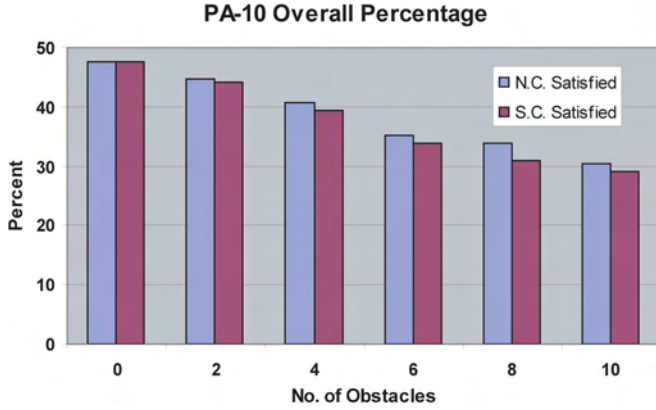


Fig. 9. Percent of 12 000 random scenarios for the PA-10 where the necessary condition (N.C.) is satisfied and where the sufficient condition (S.C.) is satisfied, i.e., where a failure surface, \mathcal{S} , is found. (Color version available online at: <http://ieeexplore.ieee.org>.)

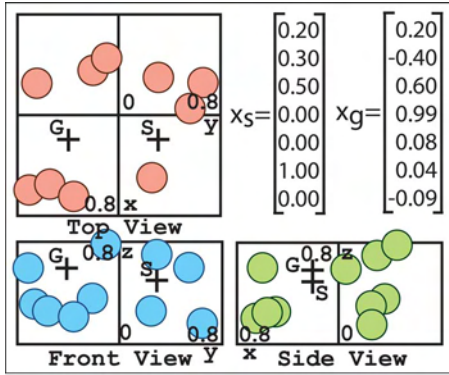


Fig. 10. A scenario within the specified range of workspace locations of the 12 000 experiments for the PA-10 robot with ten random obstacles in the workspace. Each of the obstacles has a diameter of 0.254 m (10 in). The corresponding \mathbf{x}_s and \mathbf{x}_g are shown. The first three vector components correspond to the desired position in units of meters. The last four vector components correspond to the desired orientations expressed as quaternions. (Color version available online at: <http://ieeexplore.ieee.org>.)

case, i.e., if the necessary condition is satisfied it is highly likely that the sufficient condition will also be satisfied.

A specific example from one of the 12 000 random experiments is shown in Fig. 10. The start configuration determined by the algorithm is

$$\boldsymbol{\theta}_s = [-11.5, 75.1, 43.8, -49.2, 46.8, -117.9, 27.4]^T$$

in degrees. Its corresponding failure hyperplane $\mathbf{H}_i(\boldsymbol{\theta}_s)$ intersects γ_g in the following order: $i = 7, 3, 5, 2, 6, 1$.⁴ Fig. 11

⁴The failure hyperplane $\mathbf{H}_4(\boldsymbol{\theta}_s)$ does not intersect γ_g because of the intolerance to a joint four failure.

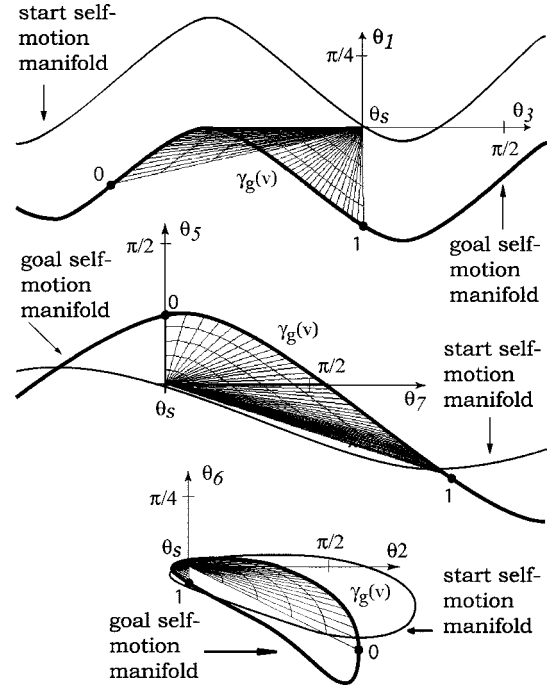


Fig. 11. Failure surface corresponding to the example in Fig. 10 shown as a web of paths in the configuration space, with projections from joint axes 1 and 3, 5 and 7, and 2 and 6. The projections are shown in the same scale with units of radians. The bold curves represent portions of \mathcal{M}_g , while the less thick curves represent portions of \mathcal{M}_s . The axes shown are translated from the origin to the feasible $\boldsymbol{\theta}_s$. Its corresponding $\gamma_g(v)$ is the curve between the points labeled “0” and “1”.

shows the corresponding failure surface \mathcal{S} for the example in Fig. 10.

VI. SUMMARY AND CONCLUSION

This work considered the problem of guaranteeing failure tolerance when obstacles are present in the environment and the desired task is of the pick-and-place type. Conditions were formulated that guarantee the existence of a solution to this problem. An algorithm was presented that searches for a simply-connected, obstacle-free surface with no internal local minimum or maximum in the configuration space, called a failure surface, whose existence guarantees a solution. Numerous examples were presented using both a 3-DOF planar robot and a 7-DOF spatial robot to illustrate the efficacy of the algorithm.

REFERENCES

- [1] E. C. Wu, J. C. Hwang, and J. T. Chladek, “Fault-tolerant joint development for the space shuttle remote manipulator system: analysis and experiment,” *IEEE Trans. Robot. Automat.*, vol. 9, no. 5, pp. 675–684, Oct. 1993.

- [2] G. Visentin and F. Didot, "Testing Space Robotics on the Japanese ETS-VII Satellite," ESA Bulletin. European Space Agency, Paris, France, Sep. 1999, pp. 61–65.
- [3] P. S. Babcock and J. J. Zinchuk, "Fault-tolerant design optimization: application to an autonomous underwater vehicle navigation system," in *Proc. Symp. Autom. Underwater Vehicle Technol.*, Washington, D.C., Jun. 5–6, 1990, pp. 34–43.
- [4] R. Colbaugh and M. Jamshidi, "Robot manipulator control for hazardous waste-handling applications," *J. Robot. Syst.*, vol. 9, no. 2, pp. 215–250, 1992.
- [5] W. H. McCulloch, "Safety analysis requirements for robotic systems in DOE nuclear facilities," in *Proc. 2nd Specialty Conf. Robot. Challenging Environ.*, Albuquerque, NM, Jun. 1–6, 1996, pp. 235–240.
- [6] M. L. Leuschen, I. D. Walker, and J. R. Cavallaro, "Investigation of reliability of hydraulic robots for hazardous environment using analytic redundancy," in *Proc. Annu. Rel. Maintain. Symp.*, Washington, D.C., Jan. 18–21, 1999, pp. 122–128.
- [7] S. Tosunoglu and V. Monteverde, "Kinematic and structural design assessment of fault-tolerant manipulators," *Intell. Automat. Soft Comput.*, vol. 4, no. 3, pp. 261–268, 1998.
- [8] D. L. Schneider, D. Tesar, and J. W. Barnes, "Development and testing of a reliability performance index for modular robotic systems," in *Proc. Annu. Rel. Maintain. Symp.*, Anaheim, CA, Jan. 24–27, 1994, pp. 263–271.
- [9] B. S. Dhillon, *Robot Reliability and Safety*. New York: Springer-Verlag, 1991.
- [10] K. Khodabandehloo, "Analysis of robot systems using fault and event trees: Case studies," *Rel. Eng. Syst. Safety*, vol. 53, no. 3, pp. 247–264, Sep. 1996.
- [11] B. S. Dhillon and A. R. M. Fashandi, "Safety and reliability assessment techniques in robotics," *Robotica*, vol. 15, no. 6, pp. 701–708, Nov.–Dec. 1997.
- [12] C. Carreras and I. D. Walker, "Interval methods for fault-tree analysis in robotics," *IEEE Trans. Robot. Automat.*, vol. 50, no. 1, pp. 3–11, Mar. 2001.
- [13] W. S. Ng and C. K. Tan, "On safety enhancements for medical robots," *Rel. Eng. Syst. Safety*, vol. 54, no. 1, pp. 35–35, Oct. 1996.
- [14] J. Trevelyan, "Simplifying robotics—a challenge for research," *Robot. Autom. Syst.*, vol. 21, no. 3, pp. 207–220, Sep. 1997.
- [15] I. D. Walker and J. R. Cavallaro, "The use of fault trees for the design of robots for hazardous environments," in *Proc. Annu. Rel. Maintain. Symp.*, Las Vegas, NV, Jan. 22–25, 1996, pp. 229–235.
- [16] A. A. Maciejewski, "Fault tolerant properties of kinematically redundant manipulators," in *Proc. IEEE Int. Conf. Robot. Automat.*, Cincinnati, OH, May 13–18, 1990, pp. 638–642.
- [17] R. G. Roberts and A. A. Maciejewski, "A local measure of fault tolerance for kinematically redundant manipulators," *IEEE Trans. Robot. Automat.*, vol. 12, no. 4, pp. 543–552, Aug. 1996.
- [18] C. L. Lewis and A. A. Maciejewski, "Fault tolerant operation of kinematically redundant manipulators for locked joint failures," *IEEE Trans. Robot. Automat.*, vol. 13, no. 4, pp. 622–629, Aug. 1997.
- [19] K. N. Groom, A. A. Maciejewski, and V. Balakrishnan, "Real-time failure-tolerant control of kinematically redundant manipulators," *IEEE Trans. Robot. Automat.*, vol. 15, no. 6, pp. 1109–1116, Dec. 1999.
- [20] J. D. English and A. A. Maciejewski, "Fault tolerance for kinematically redundant manipulators: anticipating free-swinging joint failures," *IEEE Trans. Robot. Automat.*, vol. 14, no. 4, pp. 566–575, Aug. 1998.
- [21] M. L. Visinsky, I. D. Walker, and J. R. Cavallaro, "New dynamic model-based fault detection threshold for robot manipulators," in *Proc. IEEE Int. Conf. Robot. Automat.*, San Diego, CA, May 8–13, 1994, pp. 1388–1395.
- [22] L. S. Lopes and L. M. Camarinha-Matos, "A machine learning approach to error detection and recovery in assembly," in *Proc. Int. Conf. Intell. Robots Syst.*, Pittsburgh, PA, Aug. 5–9, 1995, pp. 197–203.
- [23] H. Schneider and P. M. Frank, "Fuzzy logic based threshold adaption for fault detection in robots," in *Proc. 3rd IEEE Conf. Contr. Applicat.*, Glasgow, U.K., Aug. 24–26, 1994, pp. 1127–1132.
- [24] T. S. Wikman, M. S. Branicky, and W. S. Newman, "Reflexive collision avoidance: a generalized approach," in *Proc. IEEE Int. Conf. Robot. Automat.*, Atlanta, GA, May 2–6, 1993, pp. 31–36.
- [25] Y. Ting, S. Tosunoglu, and R. Freeman, "Actuator saturation avoidance for fault-tolerant robots," in *Proc. 32nd Conf. Decision Contr.*, San Antonio, TX, Dec. 1993, pp. 2125–2130.
- [26] Y. Ting, S. Tosunoglu, and D. Tesar, "A control structure for fault-tolerant operation of robotic manipulators," in *Proc. IEEE Int. Conf. Robot. Automat.*, Atlanta, GA, May 2–6, 1993, pp. 684–690.
- [27] K. S. Tso, M. Hecht, and N. I. Marzwell, "Fault-tolerant robotic system for critical applications," in *Proc. IEEE Int. Conf. Robot. Automat.*, Atlanta, GA, May 2–6, 1993, pp. 691–696.
- [28] M. L. Visinsky, J. R. Cavallaro, and I. D. Walker, "A dynamic fault tolerance framework for remote robots," *IEEE Trans. Robot. Automat.*, vol. 11, no. 4, pp. 477–490, Aug. 1995.
- [29] S. K. Ralph and D. K. Pai, "Computing fault tolerant motions for a robot manipulator," in *Proc. IEEE Int. Conf. Robot. Automat.*, Detroit, MI, May 10–15, 1999, pp. 486–493.
- [30] J. Park, W.-K. Chung, and Y. Youm, "Failure recovery by exploiting kinematic redundancy," in *Proc. 5th Int. Workshop Robot Human Commun.*, Tsukuba, Japan, Nov. 11–14, 1996, pp. 298–305.
- [31] C. J. J. Paredis and P. K. Khosla, "Fault tolerant task execution through global trajectory planning," *Rel. Eng. Syst. Safety*, vol. 53, pp. 225–235, 1996.
- [32] J. W. Burdick, "On the inverse kinematics of redundant manipulators: characterization of the self-motion manifolds," in *Proc. IEEE Int. Conf. Robot. Automat.*, Scottsdale, AZ, May 14–19, 1989, pp. 264–270.
- [33] —, "Kinematic analysis and design of redundant robot manipulators," Ph.D. dissertation, Stanford Univ., Stanford, CA, Mar. 1988.
- [34] R. S. Jamisola, Jr., A. A. Maciejewski, and R. G. Roberts, "Failure-tolerant path planning for the PA-10 robot operating amongst obstacles," in *Proc. IEEE Int. Conf. Robot. Automat.*, New Orleans, LA, Apr. 26–May 1 2004, vol. 5, pp. 4995–5000.



Rodrigo S. Jamisola, Jr. (S'97) received the B.S. degree in mechanical engineering from the University of the Philippines, Diliman, in 1993. From 1997 to 1999, he worked toward the M.E. degree in mechanical engineering at the National University of Singapore and received the degree in 2001. He is currently working toward the Ph.D. degree in electrical and computer engineering at Colorado State University, Fort Collins.

He joined the industry in the Philippines and later in Singapore from 1994 to 1997. He was with the Singapore Institute of Manufacturing Technology from 1999 to 2001.

His research interests include force control, motion planning, and virtual environments.



Anthony A. Maciejewski (M'87–SM'00–F'05) received the B.S.E.E., M.S., and Ph.D. degrees from Ohio State University, Columbus, in 1982, 1984, and 1987, respectively.

From 1988 to 2001, he was a Professor of electrical and computer engineering at Purdue University, West Lafayette, IN. He is currently the Department Head of Electrical and Computer Engineering at Colorado State University, Fort Collins.



Rodney G. Roberts (M'92–SM'02) received the B.S. degrees in electrical engineering and mathematics from Rose-Hulman Institute of Technology, Terre Haute, IN, in 1987 and the M.S.E.E. and Ph.D. degrees in electrical engineering from Purdue University, West Lafayette, IN, in 1988 and 1992, respectively.

From 1992 to 1994, he was a National Research Council Fellow at Wright Patterson Air Force Base, Dayton, OH. Since 1994, he has been with the Florida A&M University—Florida State University College of Engineering, Tallahassee, where he is currently a Professor of electrical and computer engineering. His research interests are in the areas of robotics and image processing.

Compliant motion using a mobile manipulator: an operational space formulation approach to aircraft canopy polishing

RODRIGO S. JAMISOLA, JR.¹, DENNY N. OETOMO²,
MARCELO H. ANG, JR.^{2,*}, OUSSAMA KHATIB³, TAO MING LIM⁴
and SER YONG LIM⁴

¹ *Department of Electrical Engineering, Colorado State University, Fort Collins, CO, USA*

² *Department of Mechanical Engineering, National University of Singapore, Singapore*

³ *Computer Science Department, Stanford University, Stanford, CA, USA*

⁴ *Singapore Institute of Manufacturing Technology, Singapore*

Received 30 July 2004; accepted 23 December 2004

Abstract—The operational space formulation provides a framework for the analysis and control of robotic systems with respect to interactions with their environments. In this paper, we discuss its implementation on a mobile manipulator programmed to polish an aircraft canopy with a curved surface of unknown geometry. The polishing task requires the robot to apply a specified normal force on the canopy surface while simultaneously performing a compliant motion keeping the surface of the grinding tool tangentially in contact with the workpiece. A human operator controls the mobile base via a joystick to guide the polishing tool to desired areas on the canopy surface, effectively increasing the mobile manipulator's reachable workspace. The results demonstrate the efficacy of compliant motion and force regulation based on the operational space formulation for robots performing tasks in unknown environments with robustness towards base motion disturbances. The mobile manipulator consists of a PUMA 560 arm mounted on top of a Nomad XR4000 mobile base. Implementation issues are discussed and experimental results are shown.

Keywords: Operational space formulation; canopy polishing; simultaneous force and motion control; mobile manipulator; compliant motion.

1. INTRODUCTION

Robust interaction between a robot and its environment is one of the most important goals of robotic systems. This is dependent on the robot's dexterity to simultaneously execute a desired motion and apply a desired force to its environment. The

*To whom correspondence should be addressed. E-mail: mpeangh@nus.edu.sg



Figure 1. A mobile manipulator consisting of a PUMA 560 mounted on a Nomad XR4000 polishing an aircraft canopy with a curved surface geometry that is unknown to the mobile manipulator. The polishing tool attached to the arm end-effector moves in a compliant scrubbing motion while maintaining a desired normal force on the aircraft canopy. The mobile base is guided by the human operator to polish the to desired areas on the canopy surface.

environment could be known to the robot, or completely unknown and unstructured, or it could even be dynamically changing. The robustness of a robot in a dynamically changing environment remains a challenge to this day.

A significant number of studies have been dedicated to the simultaneous force and motion control strategies. These studies can be divided into two categories [1]. The first category is characterized by a force control along the direction constrained by the environment and a motion control along the direction of free motion [2–4] where compliance can be achieved as shown in Refs [5–7]. The second category is characterized by achieving a desired force through a robot end-effector position control [8–11].

Among the many known algorithms, the operational space formulation by Khatib [3, 12] provides a complete treatment of the force and motion control of a robot end-effector along orthogonal directions. In this paper, an interesting application of the operational space formulation in the maintenance of aircraft canopies is shown. The aircraft canopies are polished to remove scratches and other imperfections. This task is typically done manually by human operators and is a very tedious process. In this work, attempts are made to assist human operators, through a mobile manipulator, in the aircraft canopy polishing task in order to achieve increased accuracy and productivity. The curved surface geometry of the aircraft canopy is unknown to the mobile manipulator. The tool, in the form of a polishing (or grinding) tool is attached to the end-effector of the manipulator. The tool is programmed to move in a scrubbing motion compliant to the canopy surface while maintaining a desired normal force. A human operator moves the base of the mobile manipulator, *via* a joystick, while the robot arm is autonomously performing the polishing task, thereby increasing its workspace and allowing the mobile manipulator to polish the entire surface of the canopy. Figure 1 shows the mobile manipulator used in this

work. It consists of a PUMA 560 articulated arm mounted on a Nomad XR4000 omni-directional mobile base.

This paper demonstrates the robustness of the operational space formulation to achieve simultaneous force and motion control tasks, despite the motion of the mobile base (that is treated as disturbance) and the unknown contact geometries. A method of handling robot arm singularities is also integrated into the algorithm, allowing smooth motion through singular configurations while doing the required polishing motion and maintaining the desired normal force. This is necessary as the wrist singularity of PUMA 560 is located at the position when the wrist is straightened, which is an easily reached configuration, resulting in a considerable loss of usable workspace. Impact control achieves a stable transition from free to constrained motion as the robot end-effector approaches and comes into contact with the canopy surface. Throughout the polishing task, instantaneous normal force exerted on the aircraft canopy was maintained at 10 ± 4 N with the base moving at approximately 0.5 m/s, and with the robot arm going in and out of singular configurations.

While the system can autonomously perform the force and motion control of the polishing tool on the surface of the canopy, a human operator is placed in the loop to provide the high-level commands such as which part of the workpiece needs more polishing or the polishing trajectory the tool should follow due to the irregular shape of the canopy. Placing the human operator in the loop can be done with a joystick, or even with a haptic device, as described in Ref. [13]. This is an example of an emerging paradigm for robotic applications where man-robot systems operate together with ‘divided intelligence’: humans provide high-level commands such as deciding which part of the workpiece needs more polishing or choosing the trajectory that the polishing tool should follow without providing details of intricate motions, the robot autonomously does the polishing using compliant motion. Here, the human operator and the robot do their respective tasks by exploiting their individual strengths and capabilities. The skill required for manual polishing is removed from experienced human operators and transferred to the robot, hence we also refer to this as ‘de-skilling’.

This paper is organized as follows. Section 2 provides a review of the operational space formulation. Singularity handling, impact control and friction are also discussed in this section. Implementation details including choosing the operational space control point and frame is discussed in Section 3. Section 4 presents the implementation results. Section 5 summarizes this work and discusses some issues for future implementation.

2. THE OPERATIONAL SPACE FORMULATION

The operational space formulation [3, 12] describes the dynamics of the robot as seen at the end-effector. Motion of the end-effector is generated as the necessary force vector from the current position and orientation to the desired. This establishes

a unified approach to force and motion control and is a direct and natural way of expressing a manipulator's dynamic interaction with its environment. However, knowledge of the robot dynamics is required to fully realize the benefits.

The operational space is defined by a Cartesian coordinate frame attached to the end-effector where a direct interaction between the robot and its environment takes place. Motion of the end-effector and forces acting on it, including forces induced by the mobile manipulator's dynamics, are expressed in the operational space.

The motion of the end-effector in the operational space can be expressed as

$$\mathbf{F}_{\text{motion}} = \hat{\mathbf{\Lambda}}(\mathbf{x})\mathbf{F}_{\text{motion}}^* + \hat{\boldsymbol{\mu}}(\mathbf{x}, \dot{\mathbf{x}}) + \hat{\mathbf{p}}(\mathbf{x}). \quad (1)$$

The symbol $\hat{\mathbf{\Lambda}}(\mathbf{x})$ denotes the inertia matrix, $\hat{\boldsymbol{\mu}}(\mathbf{x}, \dot{\mathbf{x}})$ denotes the Coriolis and centrifugal forces, $\hat{\mathbf{p}}(\mathbf{x})$ denotes the gravitational forces, \mathbf{x} denotes displacement and $\dot{\mathbf{x}}$ denotes velocity. All these parameters are expressed in the operational space. A physical parameter with a caret symbol ($\hat{}$) above it indicates that an estimate of this parameter is used. The symbol $\mathbf{F}_{\text{motion}}^*$ denotes the operational space motion control law and can be expressed as

$$\mathbf{F}_{\text{motion}}^* = \ddot{\mathbf{x}}_d - \mathbf{k}_{v_motion}(\dot{\mathbf{x}} - \dot{\mathbf{x}}_d) - \mathbf{k}_{p_motion}(\mathbf{x} - \mathbf{x}_d), \quad (2)$$

where $\ddot{\mathbf{x}}_d$, $\dot{\mathbf{x}}_d$ and \mathbf{x}_d denote the desired acceleration, velocity and displacement of the end-effector, respectively; and \mathbf{k}_{p_motion} and \mathbf{k}_{v_motion} denote proportional and derivative gains for motion control, respectively.

The physical parameters in the operational space are derived from the joint space parameters using:

$$\begin{aligned} \hat{\mathbf{\Lambda}}(\mathbf{x}) &= [\mathbf{J}(\mathbf{q})\hat{\mathbf{A}}^{-1}(\mathbf{q})\mathbf{J}^T(\mathbf{q})]^{-1}, \\ \hat{\boldsymbol{\mu}}(\mathbf{x}, \dot{\mathbf{x}}) &= \mathbf{J}^{-T}(\mathbf{q})\hat{\mathbf{c}}(\mathbf{q}, \dot{\mathbf{q}}) - \hat{\mathbf{\Lambda}}(\mathbf{x})\dot{\mathbf{J}}(\mathbf{q})\dot{\mathbf{q}}, \\ \hat{\mathbf{p}}(\mathbf{x}) &= \mathbf{J}^{-T}(\mathbf{q})\hat{\mathbf{g}}(\mathbf{q}), \end{aligned} \quad (3)$$

where $\mathbf{J}(\mathbf{q})$ denotes the manipulator Jacobian matrix, $\hat{\mathbf{A}}(\mathbf{q})$ denotes the inertia matrix, $\hat{\mathbf{c}}(\mathbf{q}, \dot{\mathbf{q}})$ denotes the Coriolis and centrifugal forces, $\hat{\mathbf{g}}(\mathbf{q})$ denotes the gravitational forces, \mathbf{q} denotes joint displacement and $\dot{\mathbf{q}}$ denotes joint velocity. All these are expressed in the joint space.

The force experienced at the end-effector as it interacts with its environment in the operational space can be expressed as

$$\mathbf{F}_{\text{force}} = \hat{\mathbf{\Lambda}}(\mathbf{x})\mathbf{F}_{\text{force}}^* + \hat{\boldsymbol{\mu}}(\mathbf{x}, \dot{\mathbf{x}}) + \hat{\mathbf{p}}(\mathbf{x}) + \mathbf{f}_d, \quad (4)$$

where \mathbf{f}_d is the desired force applied by the end-effector on the environment. Of equal magnitude and in the opposite direction is the desired force applied by the environment on the operational point. The symbol $\mathbf{F}_{\text{force}}^*$ denotes the operational space force control law and can be expressed as

$$\mathbf{F}_{\text{force}}^* = \mathbf{k}_{p_force}(\mathbf{f}_d - \mathbf{f}) + \mathbf{k}_{i_force} \int (\mathbf{f}_d - \mathbf{f}). \quad (5)$$

The actual force exerted by the end-effector on its environment, denoted \mathbf{f} , is derived from the force/torque sensor reading by taking the negative of the force that is read from the sensor. The direct force sensor feedback is the actual force exerted by the environment on the end-effector. The proportional and integrals gains for force control are denoted by \mathbf{k}_{p_force} and \mathbf{k}_{i_force} , respectively.

In the operational space formulation, the axes assigned to force control are orthogonal to those in motion control. To specify the orthogonal directions of motion and force control tasks, the following generalized task specification matrices are used:

$$\mathbf{\Omega} = \begin{pmatrix} \mathbf{R}_{\mathcal{F}}^T \mathbf{\Sigma}_{\mathcal{F}} \mathbf{R}_{\mathcal{F}} & \mathbf{0} \\ \mathbf{0} & \mathbf{R}_{\mathcal{M}}^T \mathbf{\Sigma}_{\mathcal{M}} \mathbf{R}_{\mathcal{M}} \end{pmatrix}, \quad (6)$$

and

$$\bar{\mathbf{\Omega}} = \begin{pmatrix} \mathbf{R}_{\mathcal{F}}^T \bar{\mathbf{\Sigma}}_{\mathcal{F}} \mathbf{R}_{\mathcal{F}} & \mathbf{0} \\ \mathbf{0} & \mathbf{R}_{\mathcal{M}}^T \bar{\mathbf{\Sigma}}_{\mathcal{M}} \mathbf{R}_{\mathcal{M}} \end{pmatrix}. \quad (7)$$

$\mathbf{R}_{\mathcal{F}}$ represents the rotation matrix associated with translation/force and $\mathbf{R}_{\mathcal{M}}$ represents the rotation matrix associated with rotation/moment. These rotation matrices are needed when the desired task is specified in a frame different from the operational space frame. The selection matrix associated with translation/force at the end-effector frame is denoted $\mathbf{\Sigma}_{\mathcal{F}}$ and that associated with rotation/moment is denoted $\mathbf{\Sigma}_{\mathcal{M}}$. These selection matrices ($\mathbf{\Sigma}_{\mathcal{F}}$ and $\mathbf{\Sigma}_{\mathcal{M}}$) are 3×3 diagonal matrices whose diagonal elements are composed of 0's and 1's. A value of 1 indicates that the corresponding direction is motion controlled, while a value of 0 indicates force control. The symbol ($\bar{}$) above a parameter indicates a binary complement of that parameter.

Thus, the combined manipulator end-effector motion and force can be expressed as

$$\mathbf{F}_{\text{total}} = \mathbf{F}_{\text{motion}} + \mathbf{F}_{\text{force}}, \quad (8)$$

where the generalized selection matrix for motion is the binary complement of the generalized selection matrix for force as used in the respective motion and force equations,

$$\mathbf{F}_{\text{motion}} = \hat{\mathbf{\Lambda}}(\mathbf{x}) \mathbf{\Omega} \mathbf{F}_{\text{motion}}^* + \hat{\boldsymbol{\mu}}(\mathbf{x}, \dot{\mathbf{x}}) + \hat{\mathbf{p}}(\mathbf{x}), \quad (9)$$

$$\mathbf{F}_{\text{force}} = \hat{\mathbf{\Lambda}}(\mathbf{x}) \bar{\mathbf{\Omega}} \mathbf{F}_{\text{force}}^* + \bar{\mathbf{\Omega}} \mathbf{f}_d. \quad (10)$$

The torque sent to the joint motors is the combined manipulator end-effector motion and force multiplied by the transpose of the manipulator Jacobian matrix

$$\boldsymbol{\Gamma} = \mathbf{J}^T(\mathbf{q}) \mathbf{F}_{\text{total}}. \quad (11)$$

The accuracy of the dynamics model is one of the most important requirements that needs to be satisfied to be able to successfully implement the operational space formulation. A number of methods have been described to identify the dynamics

parameters of a robot which include direct measurement of the dynamic parameters [14–17], a sequential identification of these parameters [18–20], moving through trajectories that excite identifiable parameters [21–23] and rule-based approach to dynamics identification [24–27]. Treatment of the robot dynamics parameters at the object-level framework is shown in Ref. [28]. In this work, the dynamics of the PUMA 560 was derived symbolically and simplified using MATHEMATICA software programmed to run the Lagrange–Euler Formulation [29]. The accuracy of the algorithm for deriving the symbolic model of the full dynamics was verified against the Matlab Robot Toolbox [30].

2.1. Singularity handling

Singularity, if not properly addressed, reduces a manipulator's usable workspace. In our application, singularity has to be addressed in both motion and force control. Usable workspace is also to be maximized. For this reason, the methods of avoiding singular configurations are not adopted. Instead we employ a singularity handling method by taking into account the lost degrees of freedom when in the singular region. A singular region is a region defined in the vicinity of a singular configuration in which a singularity robust algorithm is applied. At the exact point of singularity, the Jacobian matrix will be degenerate (or singular) and its inverse non-existent. While inside the singular region, the inverse of the Jacobian matrix is unbounded and results in an infinite joint rate for a finite task space velocities. In these configurations, the Jacobian matrix is rank-deficient and will not be able to operate in its full dofs — in the case of our robot (PUMA 560) it now possesses less than its usual 6 dofs.

We employ a method that eliminates the degenerate row of the Jacobian matrix [31], thereby reducing the dof of the task and making the robot redundant with respect to the reduced task. We first identify the singular configurations of a manipulator. When the end-effector enters a singular region, the singular configuration associated with the region is identified and the task space is transformed onto the frame of singularity $\mathbf{S}_{\mathbf{Sg}}(\mathbf{Sg}, x_{\mathbf{Sg}}, y_{\mathbf{Sg}}, z_{\mathbf{Sg}})$ with origin \mathbf{Sg} and axes $x_{\mathbf{Sg}}$, $y_{\mathbf{Sg}}$ and $z_{\mathbf{Sg}}$. This includes transforming the Jacobian matrix and the generalized forces $\mathbf{F}_{\text{total}}$, $\mathbf{F}_{\text{motion}}$ and $\mathbf{F}_{\text{force}}$ to the frame of singularity. The frame of singularity is the frame in which one of the axes is aligned with the direction of singularity. This represents the direction of mobility that the manipulator loses. There are several ways to identify the singular directions. We choose the Singular Value Decomposition because of its generality and completeness. In brief, the Singular Value Decomposition of the Jacobian matrix is expressed as:

$$SVD(\mathbf{J}(\mathbf{q})) = \mathbf{U}\mathbf{\Sigma}\mathbf{V}^T. \quad (12)$$

$\mathbf{U} \in \mathbb{R}^{m \times m}$ and $\mathbf{V} \in \mathbb{R}^{n \times n}$ are proper orthogonal matrices and $\mathbf{\Sigma} \in \mathbb{R}^{m \times n}$ is a diagonal matrix with values $(\sigma_1, \sigma_2, \dots, \sigma_m)$ [32], where $\sigma_1 \geq \sigma_2 \geq \dots \geq \sigma_m \geq 0$ are the singular values of the matrix.

When singularity occurs, the smallest value(s) of σ_k is zero. This causes $\Sigma \mathbf{V}^T$ to be an $m \times n$ matrix (of the same dimension of the Jacobian matrix) with a row of zero, representing the direction of singularity of the manipulator. Treating \mathbf{U} as a rotational matrix, then it can be used to transform the task space into the frame of singularity:

$${}^S \mathbf{J} = \mathbf{U}^T \mathbf{J} = \Sigma \mathbf{V}^T. \quad (13)$$

After the Jacobian matrix is expressed in the frame of singularity, the direction of singularity will be reflected as a row of zeros. The degenerate component of the task is therefore eliminated by removing the zero row from the Jacobian matrix and the associated element from the generalized force vectors. The result is a Jacobian matrix that is full rank but of smaller number of rows and generalized force vectors with a reduced number of elements. The dynamics of the manipulator (which requires the inverse of the Jacobian matrix) is then calculated with the reduced Jacobian matrix but with full rank.

While inside the singular region, motion in the direction of singularity is eliminated. If motion is required in the singular direction, the end-effector can be assisted to move in such direction by the application of null space motion. Null space motion is possible inside the singular region, because one or more of the rows in the Jacobian matrix have been eliminated, which results in fewer dofs in the task space than in the joint space.

As a different control algorithm is applied inside the singular region, there is a discontinuity at the boundary of the region. This is particularly evident as the end-effector exits the singular region. Methods to smoothen out the discontinuities exist and are elaborated in Ref. [33].

2.2. Joint friction

Friction plays a significant role in robot control. When accurately modeled and used in the robot control, it could contribute to a significant improvement. The friction parameters modeled in this work are: static, kinetic or Coulomb, and fluid friction.

For each joint component of the manipulator, the friction model that is used in the force and motion control is,

$$\tau_{\text{friction}} = f_s \left(\frac{\text{sgn}(\dot{q})}{1 + \left(\frac{\dot{q}}{x_s} \right)^2} \right) + f_k \tanh(\dot{q}) + k_{vn} \dot{q}, \quad (14)$$

where f_s denotes static friction, x_s denotes a constant to correct static friction due to the Stribeck effect, f_k denotes kinetic friction, k_{vn} denotes fluid friction and \dot{q} is the joint velocity. All the friction parameters have to be identified for each manipulator joint.

The total torque sent to the joint motors from equation (11) is added with the friction model to compensate for friction at each manipulator joint, that is,

$$\mathbf{\Gamma} = \mathbf{J}^T(\mathbf{q})\mathbf{F}_{\text{total}} + \boldsymbol{\tau}_{\text{friction}}. \quad (15)$$

2.3. Impact control

Another issue needed to be addressed in this work is the transition from contact to non-contact state between the end-effector of the manipulator and its environment. We employ impact loading control [34] to create a smooth transition between the two states. The key idea is to quickly dissipate the impact force using a motion command:

$$\mathbf{F}_{\text{motion}}^* = -\mathbf{k}_{v_motion}\dot{\mathbf{x}}. \quad (16)$$

Note that the $\mathbf{F}_{\text{motion}}^*$ is different from equation (2).

3. IMPLEMENTATION

After the derivation of the full dynamics model and the identification of its parameters, the operational space formulation is ready for implementation. Several stages of implementation were performed before finally arriving at simultaneous force and motion control.

3.1. Gravity compensation on force/torque sensor reading

For the purpose of cancelling the gravity effect on the manipulator arm, the mass and center of mass model of the manipulator is fed forward. This stage verifies the accuracy of the mass and center of mass for each link of the manipulator. With a ‘floating’ manipulator, the human operator can move the manipulator links to anywhere within its workspace with minimal effort. This has a direct application in walk-through programming for welding robots [35].

Gravity compensation in the force reading is important in the polishing task, as one would like to decouple the weight of the polishing tool from the contact forces with the environment. The force sensor frame is denoted by $\mathbf{S}_S(\mathcal{S}, x_s, y_s, z_s)$ with origin \mathcal{S} and axes x_s , y_s and z_s (see Fig. 2). A force/torque sensor provides readings of forces/torques acting on the sensor frame, with respect to the sensor frame itself. A sensor reading of the force/torque applied by the manipulator on its environment, with the weight of the tool removed, is denoted ${}^s\mathbf{f}_s$. It can be expressed as

$${}^s\mathbf{f}_s = {}^s\mathbf{f}_{\text{raw}} + {}^s\mathbf{f}_{\text{gravity}} - {}^s\mathbf{f}_{\text{offset}}, \quad (17)$$

where ${}^s\mathbf{f}_{\text{raw}}$ is the negative of the total force/torque applied by the environment on the manipulator’s end-effector (including gravitational effects), ${}^s\mathbf{f}_{\text{gravity}}$ is the model

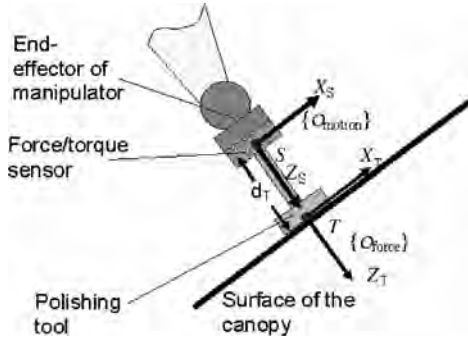


Figure 2. The choice of operational point for simultaneous force and motion control. The motion control operational point (O_{motion}) was specified to be at the center of the force/torque sensor (point S), while the force control operational point (O_{force}) was placed at the center of the face of the polishing tool tip (point T). The orientation of frames S and T are the same.

of the gravitational force/torque that is added in order to correct the gravitational forces acting on the force/torque sensor and ${}^s\mathbf{f}_{\text{offset}}$ is the force/torque offset used by most sensors to automatically zero out the current sensor reading upon activation.

To model the gravitational term, ${}^s\mathbf{f}_{\text{gravity}}$, the manipulator's end-effector is assumed to be at initialization when the necessary corrections were made, that is, facing upward. The gravitational model is computed by expressing the gravitational force at the polishing tool's center of mass, ${}^0\mathbf{f}_m$, with respect to the base frame (0) and changing its reference frame to that of the force sensor frame (S), that is,

$${}^s\mathbf{f}_{\text{gravity}} = {}^s\mathbf{J}_m^* {}^m\mathbf{J}_0^* {}^0\mathbf{f}_m, \quad (18)$$

where ${}^0\mathbf{f}_m$ is the gravitational force at the center of mass of the polishing tool expressed with respect to the base frame and is computed as ${}^0\mathbf{f}_m = [0 \ 0 \ m_{\text{tool}}g \ 0 \ 0 \ 0]^T$. The total mass of the polishing tool $m_{\text{tool}} = 1.8$ kg and the gravitational constant $g = 9.81$ m/s². The orientation of the tool frame is coincident with the orientation of the sensor frame. Thus the transformation matrix ${}^s\mathbf{J}_m^*$ changes the reference frame from the tool to the sensor by taking into account only the distance between the origin of the two frames,

$${}^s\mathbf{J}_m^* = \begin{pmatrix} \mathbf{I} & \mathbf{0} \\ [{}^s\mathbf{p}_m \times] & \mathbf{I} \end{pmatrix}, \quad (19)$$

where ${}^s\mathbf{p}_m$ is the position vector of the tool's center of mass with respect to the sensor frame such that

$$[{}^s\mathbf{p}_m \times] = \begin{bmatrix} 0 & -{}^s p_{mz} & {}^s p_{my} \\ {}^s p_{mz} & 0 & -{}^s p_{mx} \\ -{}^s p_{my} & {}^s p_{mx} & 0 \end{bmatrix}, \quad (20)$$

where ${}^s p_{mx}$, ${}^s p_{my}$ and ${}^s p_{mz}$ are the x , y and z components of the vector ${}^s \mathbf{p}_m$, respectively. The transformation matrix ${}^m \mathbf{J}_0^*$ can be derived from the transformation matrix ${}^s \mathbf{J}_0^*$

$${}^s \mathbf{J}_0^* = \begin{bmatrix} {}^s \mathbf{R}_0 & \mathbf{0} \\ \mathbf{0} & {}^s \mathbf{R}_0 \end{bmatrix}, \quad (21)$$

since the sensor frame orientation is the identical to the tool frame orientation. ${}^s \mathbf{R}_0$ is the orientation of the base frame, $\mathbf{S}_0(\mathbf{0}, x_0, y_0, z_0)$, with respect to the sensor frame, $\mathbf{S}_S(\mathcal{S}, x_s, y_s, z_s)$. The orientation of the sensor frame is identical to the orientation of the end-effector frame which makes ${}^s \mathbf{R}_0 = {}^0 \mathbf{R}_e^T$.

3.2. Motion and force control

The operational point for motion control ($\mathcal{O}_{\text{motion}}$) was chosen to be at the center of the force/torque sensor (see Fig. 2). Due to the higher degree of flexibility of the polishing tool compared to the links of the PUMA manipulator, choosing the operational point for motion control closer to the wrist point helps keep the compliant motion robust, as less effort is needed in controlling the posture of the manipulator. The desired motion at the wrist is transformed to $\mathcal{O}_{\text{motion}}$ through the appropriate transformation matrix and motion control is performed by tracking the desired trajectory at this point. The robot control is based on the dynamics of rigid bodies and the higher degree of flexibility of the polishing tool create higher penalty on the motion control.

A PI controller is set up to regulate force control (equations (4) and (5)). The compliant motion of the manipulator, adjusting its pose such that its end-effector is always normal to the surface of the workpiece being polished, is created by setting the desired moment to zero around the x_t and y_t axes of the end-effector frame $\mathbf{S}_T(T, x_t, y_t, z_t)$ (see Fig. 2). Due to the high frequency noise of the force/torque sensor reading, a derivative controller was found to introduce too much instability. A PI controller was chosen instead.

The operational point of the force controller ($\mathcal{O}_{\text{force}}$) was placed at the center of polishing tool tip, in contact with the surface of the workpiece/environment (point T , see Fig. 2). One advantage of this choice is that it allows compliance of the whole robot structure as a response to the interaction force and moment with the environment at the end-effector. Another advantage is that it eliminates the ambiguity of the moment reading which is present if the operational point was placed at the center of the force/torque sensor itself (point S). By ambiguity, we mean that a reading for moments at the force/torque sensor (around x_s and y_s axes of the sensor frame), could mean two things. The first is the moment created by the polishing tool's friction with the surface of the workpiece, as it moves along the surface (a moment reading around x_s axis of the end-effector frame is created by motion in the y_s direction and *vice versa*). The second is due to the need for compliant motion, as the curvature of the workpiece surface changes. Placing the operational point at the center of the polishing tool, in contact with the surface of

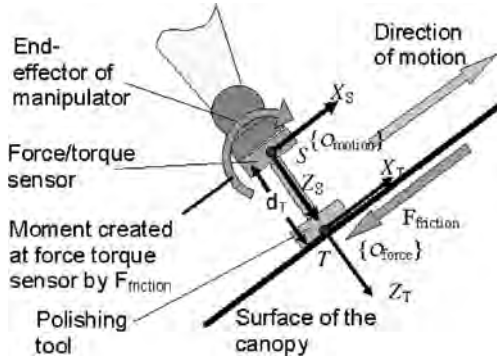


Figure 3. Friction force $\mathbf{F}_{\text{friction}}$ causes a moment reading to be registered at the force/torque sensor (point S), but creates no moment at point T ($\mathcal{O}_{\text{force}}$).

the workpiece means that the frictional forces between the surfaces ($\mathbf{f}_{\text{friction}}$) would generate no resultant moment around the operational point ($\mathcal{O}_{\text{force}}$) (see Fig. 3).

The forces at the tooltip can be computed from the force sensor reading using the following transformation:

$${}^T\mathbf{f}_T^* = \begin{pmatrix} \mathbf{I} & \mathbf{0} \\ [{}^S\mathbf{p}_T \times] & \mathbf{I} \end{pmatrix} {}^S\mathbf{f}_S, \quad (22)$$

where ${}^S\mathbf{p}_T$ is the position vector of the operational point T with respect to the sensor frame. The term $[{}^S\mathbf{p}_T \times]$ is a skew symmetric matrix as defined in equation (20).

3.3. Specifying direction for motion and force control

Following the explanation in Section 3.2, in the polishing task, the operational point for motion control is set to be the center of the force/torque sensor ($\mathcal{O}_{\text{motion}}$), while that for force control is at the center of the polishing tool surface which is in contact with the workpiece ($\mathcal{O}_{\text{force}}$, see Figs 2 and 3). Although the origins of the two reference frames are not coincident, the directions of their respective axes are the same. Thus, by specifying a direction to be under force control, the corresponding motion control in the same direction is disabled.

Force is controlled in the direction of the z_T -axis (see Fig. 3). In the polishing task, the z_T -axis is the instantaneous normal to the canopy surface as the robot end-effector moves along the surface. The desired normal force to be exerted on the surface of the environment is specified along the z_T -axis. Moment is controlled about the x_T - and y_T -axes. Motion control is specified along the remaining axes that are not under force/moment control: position control along the x_T - and y_T -axes and orientation control about the z_T -axis. This results in the following selection matrices ($\Sigma_{\mathcal{F}}$ and $\Sigma_{\mathcal{M}}$):

$$\Sigma_{\mathcal{F}} = \begin{pmatrix} 1 & 0 & 0 \\ 0 & 1 & 0 \\ 0 & 0 & 0 \end{pmatrix}, \quad (23)$$

$$\Sigma_{\mathcal{M}} = \begin{pmatrix} 0 & 0 & 0 \\ 0 & 0 & 0 \\ 0 & 0 & 1 \end{pmatrix}. \tag{24}$$

3.4. Singularity handling

In our application, where a PUMA 560 robot was used, there are three singularity configurations: head, elbow and wrist singularities. The most critical one is the wrist singularity, as it happens when the wrist is straightened and it is a frequently occurring configuration. Elbow and head singularities never occur in our polishing application.

For the example of wrist singularity of PUMA 560 used in our application, the singular configuration is identified by taking the determinant of the Jacobian matrix as the configuration where the wrist is straightened ($q_5 = 0$). The singular region is defined as:

$$|q_5| \leq q_{5l}, \tag{25}$$

where q_{5l} is the threshold value of the joint.

In the case of the wrist singularity, null space motion is utilized to smooth out the discontinuity by keeping the singular direction away from the desired trajectory. The null space motion creates internal joint motion that shifts the direction of singularity. While inside the singular region, a potential function is defined so that the direction of singular is perpendicular to the desired path. This also has the additional effect of ensuring that the end-effector moves along, and exits the singular region through, a controllable axis of motion, which is orthogonal to the direction of singularity. Hence, no discontinuity occurs at the boundary of the singular region. Details are given in Ref. [33].

3.5. Joint friction

The fluid friction parameters are identified together with the manipulator dynamics as discussed in [20]. On the other hand, static and kinetic friction parameters were derived using the methods discussed in [36]. The values of the friction parameters that were derived are shown in Table 1.

Table 1.
Friction parameters of PUMA 560

Link	f_s	f_k	k_{vn}	x_s
1	5	2	1	0.1
2	5	2	1	0.1
3	2.5	1	1	0.1
4	0.3	0.1	0.05	0.1
5	0.2	0.1	0.05	0.1
6	0.2	0.1	0.05	0.1

3.6. Impact control

In the overall canopy polishing task, the mobile manipulator undergoes three stages:

- the end-effector approaches the canopy using motion control;
- then it establishes contact with the canopy surface and dissipates the force of impact using impact loading and control;
- and lastly, it performs the polishing task using unified force and motion control.

At stage 1, the operator roughly guides the mobile manipulator to a location so that it faces the workpiece (the canopy to be polished) and a command to move the end-effector forward towards the surface is given in order to establish a contact between the polishing tool and the canopy surface. Since this stage uses motion control, the selection matrices $\Sigma_{\mathcal{F}}$ and $\Sigma_{\mathcal{M}}$ are set to identity and the motion control law in equation (2) is used. Throughout this motion, force is monitored along the z_t -axis of the end-effector frame $\mathbf{S}_{\mathcal{T}}(T, x_t, y_t, z_t)$ with a threshold of 10 N. When the polishing tool collides with the canopy, a force along z_t -axis that is way above the threshold is sensed. The manipulator would then enter into the second stage using impact loading and control. Here, equation (16) is used instead of equation (2), in order to dissipate the impact of collision between the tool and the aircraft canopy. After the impact has been dissipated and the force along z_t -axis goes below the threshold value of 10 N, the manipulator commences the polishing algorithm (stage 3).

4. IMPLEMENTATION RESULTS

Data of the mobile manipulator responses at the different stages of the aircraft canopy polishing task are presented in this section. Graphs are shown for the following robot responses during motion control, during simultaneous force and motion control while performing the polishing task, variation in force reading while polishing within the singularity region, force profile measured during impact and force dissipation, and the effect of friction modeling on the performance of the system in the polishing task.

In this work, although the PUMA 560 is physically attached to the XR4000 mobile base, the controller of the manipulator arm is not integrated with the controller of the mobile base. Thus, the manipulator arm and the mobile base are independently controlled. Throughout this work, the operational space formulation applies only to the manipulator arm while the mobile base is controlled *via* a joystick. Thus the human operator's random motion of the mobile base is considered purely as disturbance to the polishing task.

A JR3 six-axes force/torque sensor is attached on the face of the sixth link of the arm. Then on the other end of the force/torque sensor, a grinder tool with a rated speed of 10 000 rpm is attached. The grinder tool, which weighs about 1.8 kg, has been accurately compensated for gravity on the force/torque sensor reading. The end-effector exerts the required instantaneous normal force of 10 N on the

canopy surface. During canopy polishing, the mobile base was randomly moved by the human operator *via* a joystick at an average speed of 0.5 m/s. Emphasis on the implementation results is focused on how well the manipulator arm’s end-effector achieved the desired normal force on the canopy surface while moving in a compliant behavior with base disturbances created by the random motion of the mobile base and the end-effector disturbances created by the running grinder.

4.1. Motion control in operational space

After the verification of a correct robot response on gravitational force compensation where the manipulator arm floats against forces of gravity, the motion control verifies the correctness of the inertial parameters of the full dynamics model. Motion control is admittedly less sensitive to errors in the model and control of a manipulator compared to a combined force and motion control. However, by specifying a higher precision in the robot response in motion control with the robot running at higher speeds, a manipulator can be determined to have achieved the desired level of accuracy. To this end, the PUMA was put to an extreme test. Shown in Fig. 4 is the error in the PUMA response as it moved with motion control in all six degrees-of-freedom operational space. The PUMA is tasked to move 1 m in 1 s along the base frame axis y_0 (horizontal) with fixed end-effector orientation facing downward. To achieve these goal parameters, the PUMA end-effector reached a maximum speed of 1.9 m/s.

Position errors are shown as X_{err} , Y_{err} , and Z_{err} in units of meters, while orientation errors are shown as $DPhi[1]$, $DPhi[2]$, and $DPhi[3]$ in units of radians.

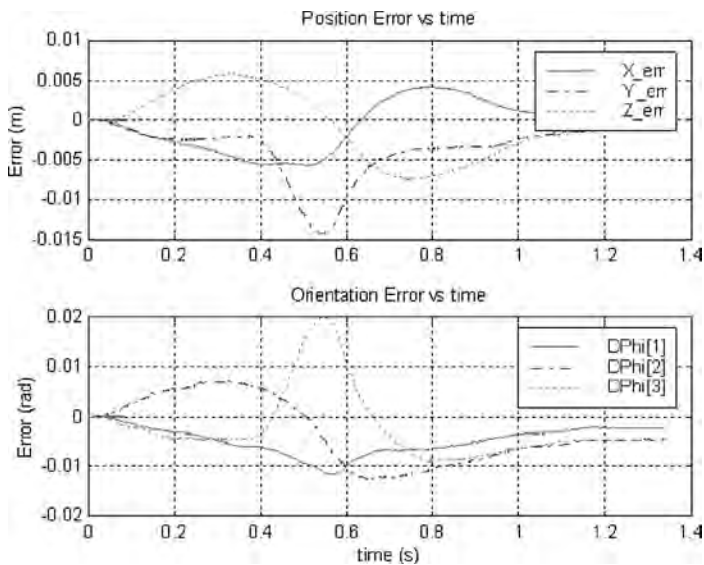


Figure 4. Error response of the PUMA arm in motion control with its end-effector running at a maximum speed of 1.9 m/s.

Maximum position error is along the y_0 -axis, being 0.014 m. One possible cause of this relatively significant error could be the saturation of the joint motors at the maximum end-effector speed. The orientation error is derived from the cross product of the actual and desired orientation vectors \mathbf{n} , \mathbf{o} and \mathbf{a} as stated in Ref. [37], that is,

$$\delta\Phi = \frac{1}{2}((\mathbf{n}_a \times \mathbf{n}_d) + (\mathbf{o}_a \times \mathbf{o}_d) + (\mathbf{a}_a \times \mathbf{a}_d)), \quad (26)$$

where \mathbf{n} , \mathbf{o} and \mathbf{a} are columns of an orientation matrix expressing the orientation of the end-effector with respect to the base, that is, ${}^0\mathbf{R}_e = [\mathbf{n} \ \mathbf{o} \ \mathbf{a}]$ and the subscripts a and d refer to actual and desired parameters. Maximum orientation error is around the z_0 -axis which is 0.02 radians.

4.2. Simultaneous force and motion control

The PUMA end-effector was specified to run a non-terminating sinusoidal path along the y_t -axis of the end-effector frame $\mathbf{S}_T(T, x_t, y_t, z_t)$, with respect to the base frame, with an amplitude of 0.15 m and a period of 5 s.

An inherent disturbance to the PUMA is the motion of the grinder attached to its end-effector (rated at 10 000 rpm). The other disturbance is at the PUMA's base where the independently controlled XR4000 is randomly moved by the human operator *via* a joystick in order to move the whole mobile manipulator to give its end-effector access to desired areas on the canopy. The PUMA response for simultaneous force and motion control with the given disturbances is shown in Fig. 5.

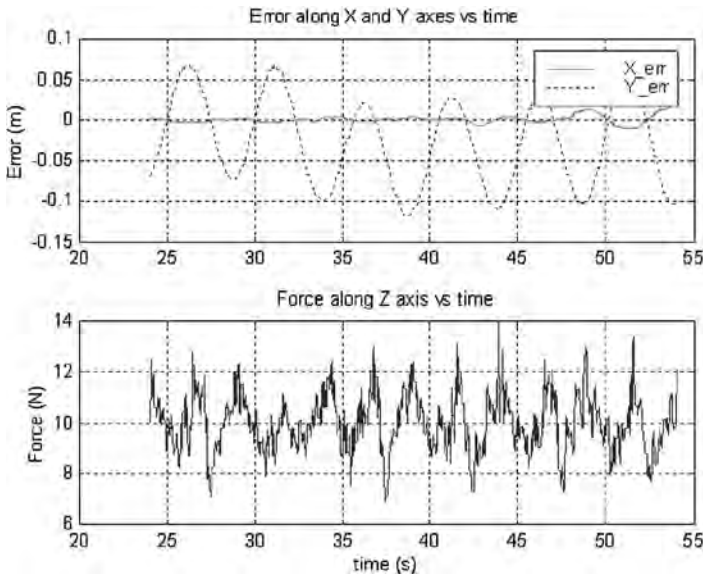


Figure 5. Error response of the PUMA doing polishing on the aircraft canopy with 10 N desired normal force and with Nomad base moving.

The maximum position error along the direction of motion (y_t -axis of the frame $S_T(T, x_t, y_t, z_t)$) and is at 0.12 m, compared to 0.07 m when the polishing was done with a stationary base. The maximum force error along the z_t -axis of the frame $S_T(T, x_t, y_t, z_t)$ is 4 N, compared to about 3.2 N when the base is stationary. The main source of error in the tracking performance is the unmodeled friction between the polishing tool and the surface of the canopy. This causes a lag in the end-effector's tracking of the desired trajectory. This lag is not critical in our application as we only need to polish around the area.

4.3. Force reading around the region of singularity

Compared to position errors, force errors in a robot response are more sensitive to non-smooth transitions in the robot control. Thus, the robustness of the singularity handling algorithm presented in this work is tested by the letting the PUMA polish the aircraft canopy as it goes in and out of the wrist singularity region (Fig. 6) and the normal force exerted on the canopy is observed. The results are shown in Fig. 7.

The PUMA is set to move along the x_t -axis of the end-effector frame $S_T(T, x_t, y_t, z_t)$ with respect to the stationary base frame. As the PUMA performed its polishing task in a sinusoidal path, it crosses the singular configuration every time the wrist is straightened (see Fig. 6), the determinant of the Jacobian is recorded to monitor its proximity with respect to singularity (Fig. 7). A value of zero for the determinant of the Jacobian is a point of singularity. The desired normal force on the canopy surface is set to the same value of 10 N. Around the region of singularity, the

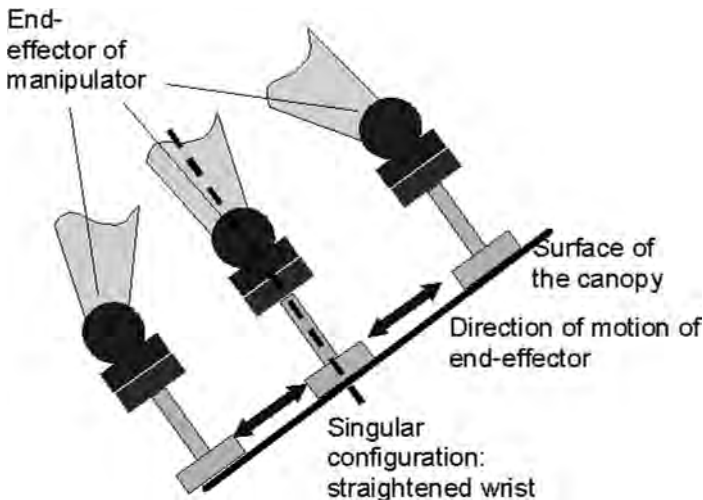


Figure 6. The experimental setup where PUMA is to move sinusoidally about the wrist singularity, while performing motion and force control. The singular configuration is when the wrist is straightened.

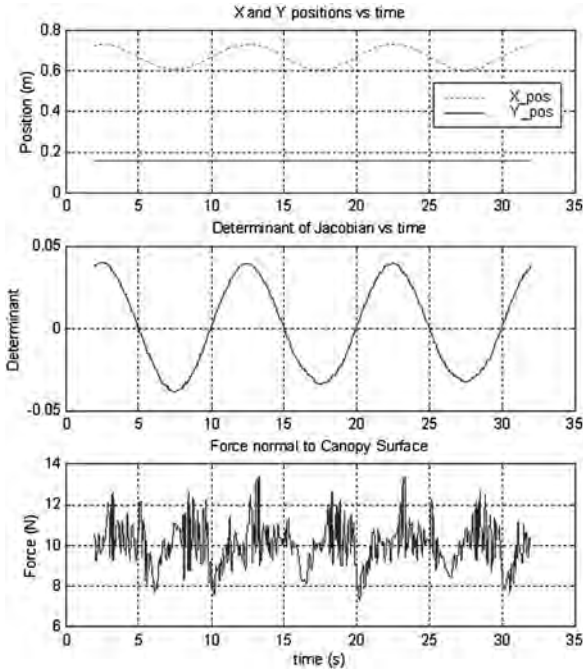


Figure 7. Force reading exerted by PUMA normal to the aircraft canopy surface at it moves in and out of wrist singularity region.

maximum force error reading is 3.7 N, without any significant difference from the maximum of 3.2 N when polishing was done with a stationary base without going through singular configuration.

4.4. Force dissipation on impact

Figure 8 shows the results for impact loading and control. As the PUMA end-effector approached the canopy surface, force was monitored along the z_T -axis of the end-effector frame $S_T(T, x_t, y_t, z_t)$ with respect to the same frame. A threshold of 10 N was used to determine the instance of impact and the dissipation of impact forces. As soon as impact was detected, impact loading control was performed using equation (16). As the impact forces were dissipated, the PUMA then started its polishing task.

4.5. Manipulator response with and without friction compensation

The comparison of the end-effector force exerted normal to the canopy surface with and without compensating friction parameters while the manipulator is performing its polishing task is shown in Fig. 9. Notice the difference in time when the force data were taken. This is because the data was taken on exactly the same experimental setup noting the fact that friction parameters are dependent on ambient condition. On the first set of data, the PUMA polished the canopy without friction

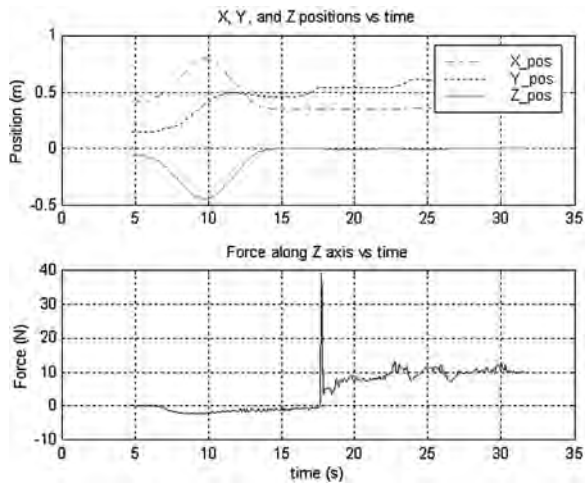


Figure 8. Force reading exerted by PUMA normal to the aircraft canopy surface before, during and immediately after impact loading.

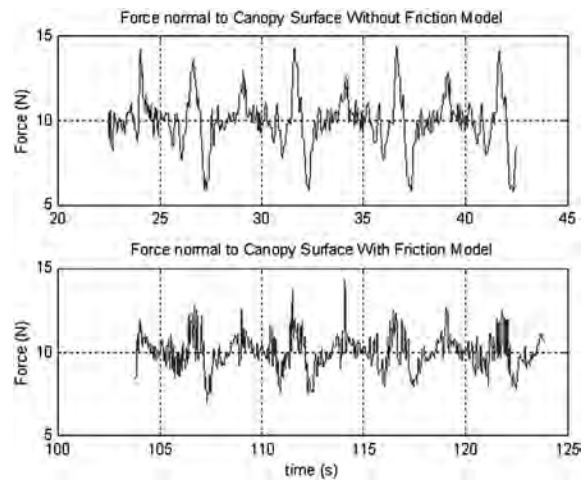


Figure 9. Comparison on the force reading exerted by PUMA normal to the aircraft canopy surface with and without friction model.

model and the force response was recorded. Then, as it continued to perform the polishing task the friction model was introduced, after which the next set of force responses were recorded. It was observed that friction compensation was able to reduce maximum force tracking error by up to 32%.

5. CONCLUSIONS

It has been shown in this implementation that robust simultaneous force and motion control is possible for a mobile manipulator set-up where the manipulator arm,

a PUMA 560, is controlled independent of the mobile base, a Nomad XR4000. The full dynamics of the PUMA are modeled and it is controlled using the operational space formulation. The PUMA performed the polishing task subject to end-effector disturbances due to the attached grinder running at a rated speed of 10 000 rpm plus base disturbances due to the human operator randomly moving the mobile base at an average speed of 0.5 m/s. The polishing task was performed with the end-effector exerting a normal force of 10 ± 4 N on the canopy surface and moving in a compliant motion on the curved canopy surface that is of unknown geometry. Further work would be focused in implementing a fully integrated mobile manipulator with it a full dynamic model of the combined mobile manipulator system.

Acknowledgements

The financial support of Singapore Institute of Manufacturing Technology in this collaborative research project is gratefully acknowledged.

REFERENCES

1. D. E. Whitney, Historical perspective and state of the art in robot force control, *Int. J. Robot. Res.* **6** (1), 3–14 (1987).
2. M. H. Raibert and J. J. Craig, Hybrid position/force control of manipulators, *ASME J. Dyn. Syst., Meas., Contr.* **103** (2), 126–133 (1981).
3. O. Khatib, A unified approach for motion and force control of robot manipulators: The operational space formulation, *IEEE J. Robot. Automat.* **RA-3** (1), 43–53 (1987).
4. J. K. Mills and A. A. Goldenberg, Force and position control of manipulators during constrained motion and tasks, *IEEE Trans. Robot. Automat.* **5** (1), 30–46 (1989).
5. R. P. C. Paul and B. Shimano, Compliance and control, in: *Proc. Joint Automat. Contr. Conf.*, San Francisco, CA, pp. 694–699 (1976).
6. M. T. Mason, Compliance and force control for computer controlled manipulators, *IEEE Trans. Syst., Man, Cybern.* **SMC-11** (6), 418–432 (1981).
7. L. L. Whitcomb, S. Arimoto, T. Naniwa and F. Ozaki, Adaptive model-based hybrid control of geometrically constrained robot arms, *IEEE Trans. Robot. Automat.* **13** (1), 105–116 (1997).
8. N. Hogan, Impedance control: An approach to manipulation, *ASME J. Dyn. Syst., Meas., Contr.* **107** (1), 1–24 (1985).
9. H. Kazerouni, On the robot compliant motion control, *ASME J. Dyn. Syst., Meas., Contr.* **111** (3), 416–425 (1989).
10. J. K. Salisbury, Active stiffness control of a manipulator in cartesian coordinates, in: *Proc. 19th IEEE Conf. Decision Contr.*, Albuquerque, NM, Vol. 1, pp. 95–100 (1980).
11. M. Pelletier and L. K. Daneshmend, An approach to compliant motion planning using uncertain impedance models, in: *Proc. IASTED Int. Conf. Contr. Robot.*, Vancouver, pp. 58–61 (1992).
12. O. Khatib, Commande dynamique dans l'espace operationnel des robots manipulateurs en presence d'obstacles, PhD dissertation, Ecole Nationale Superieure de l'Aeronautique et de l'Espace, Toulouse (1980) (in French).
13. D. Oetomo, M. H. Ang, Jr. and T. M. Lim, Haptic interface for force/motion controlled mobile manipulator, in: *Proceedings of the 2nd IFAC Conference on Mechatronic Systems*, Berkeley, CA, pp. 566–571 (2002).
14. A. K. Bejczy, Robot arm dynamics and control, *Technical Memo* **33** (669) (1974).

15. R. Paul, M. Rong and H. Zhang, Dynamics of puma manipulator, in: *Proc. Am. Control Conf.*, San Francisco, CA, pp. 491–496 (1983).
16. T. J. Tarn, A. K. Bejczy, S. Han and X. Yun, Inertia parameters of PUMA 560 robot arm, Technical Report, Volume SSM-RL-85-01 (1985).
17. B. Armstrong, O. Khatib and J. Burdick, The explicit dynamic model and inertial parameters of the PUMA 560 arm, in: *Proc. IEEE Int. Conf. Robot. Automat.*, San Francisco, CA, pp. 510–518 (1986).
18. M. Renaud, An efficient iterative analytic procedure for obtaining a robot manipulator dynamic model, *Int. J. Robot. Res.* **3**, 749–764 (1984).
19. J. J. Curtelin, Sequential identification of the dynamic parameters of a robot, in: *Proc. 5th Int. Conf. Adv. Robot.*, Pisa, Italy, pp. 1513–1516 (1991).
20. R. Jamisola, M. H. Ang, Jr., T. M. Lim, O. Khatib and S. Y. Lim, Dynamics identification and control of an industrial robot, in: *Proc. 9th Int. Conf. Adv. Robot.*, Tokyo, Japan, pp. 323–328 (1999).
21. B. Armstrong-Hélouvry, On finding ‘exciting’ trajectories for identification experiments involving systems with non-linear dynamics, *Int. J. Robot. Res.* **8** (6), 28–48 (1989).
22. P. K. Khosla, Categorization of parameters in the dynamic robot model, *IEEE J. Robot. Automat.* **5** (3), 261–268 (1989).
23. J. Swevers, C. Ganseman, D. B. Tukel, J. D. Schutter and H. V. Brussel, Optimal robot excitation and identification, *IEEE Trans. Robot. Automat.* **13** (5), 730–740 (1997).
24. R. Lucyshyn and J. Angeles, A rule-based framework for parameter estimation of robot dynamic models, in: *Proc. Int. Conf. Intell. Robots Syst.*, Osaka, Vol. 2, pp. 745–750 (1991).
25. K. Yuan, C. Wang and L. Yan, A new approach to parameter identification of robot manipulators, in: *Proc. IEEE Int. Conf. Ind. Tech.*, pp. 92–96 (1994).
26. A. Y. Zomaya, Extraction and computation of identifiable parameters in robot dynamic models: theory and application, in: *IEEE Proc. Contr. Theory Appl.* **141**, 48–56 (1994).
27. P. O. Vandajon, M. Gautier and P. Desbats, Identification of robots inertial parameters by means of spectrum analysis, in: *Proc. IEEE Int. Conf. Robot. Automat.*, Nagoya, Aichi, Vol. 3, pp. 3033–3038 (1995).
28. O. Khatib, Inertial properties in robotic manipulation: An object-level framework, *Int. J. Robot. Res.* **14** (1), 19–36 (1995).
29. K. Fu, R. Gonzales and C. Lee, *Robotics: Control, Sensing, Vision, and Intelligence*. McGraw-Hill, Singapore (1987).
30. P. Corke, A robotics toolbox for matlab, *IEEE Robot. Automat. Magn.* **3** (1), 24–32 (1996).
31. D. Oetomo, M. H. Ang, Jr. and S. Y. Lim, Singularity handling on puma in operational space formulation, in: *Lecture Notes Control Inform. Sci.* **271**, 491–501 (2001).
32. T. Yoshikawa, Analysis and control of robot manipulators with redundancy, in: *Robotics Research*, M. Brady and R. Paul (Eds), pp. 735–747. MIT Press, Cambridge, MA (1984).
33. D. Oetomo and M. H. Ang, Jr., Singularity handling method with division in workspace and discontinuity issue, in: *Proc. Int. Symp. Dynam. Control*, Hanoi (2003).
34. O. Khatib and J. Burdick, Motion and force control of robot manipulators, in: *Proc. IEEE Int. Conf. Robot. Automat.*, San Francisco, CA, pp. 1381–1386 (1986).
35. M. H. Ang, Jr., W. Lin and S. Y. Lim, A walk-through programmed robot for welding in shipyards, *Ind. Robot* **26** (5), 377–388 (1999).
36. B. Armstrong-Hélouvry, *Control of Machines with Friction*. Kluwer, Boston, MA (1991).
37. J. Luh, M. Walker and R. Paul, Resolved-acceleration control of mechanical manipulators, *IEEE Trans. Automat. Contr.* **AC-25** (3), 468–474 (1980).

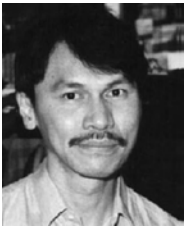
ABOUT THE AUTHORS



Rodrigo S. Jamisola, Jr. received the BS in Mechanical Engineering from the University of the Philippines, Diliman, in 1993. He received his Master of Engineering from National University of Singapore in 2001 and is currently a PhD student at Colorado State University. His research interests include force and motion control, and failure-tolerant motion planning for redundant robots.



Denny Oetomo received the BEng from the Australian National University in 1997 and PhD from National University of Singapore (NUS) in 2004. He worked as photolithography engineer for Hewlett Packard Singapore in 1998–1999 and as research engineer to NUS and the Singapore Institute of Manufacturing Technology in 2002–2004. He joined the Robotics and Mechatronics Research Laboratory (RMRL) at Monash University in November 2004 where he is currently a Research Fellow. His research interests include force and motion control of mechanisms, haptics and micro/nano-manipulation with flexure joints.



Marcelo H. Ang, Jr. received the BS degrees (cum laude) in Mechanical Engineering and Industrial Management Engineering from the De La Salle University, Manila, Philippines, in 1981; the MS degree in Mechanical Engineering from the University of Hawaii at Manoa, Honolulu, HI, in 1985; and the MS and PhD degrees in Electrical Engineering from the University of Rochester, Rochester, NY, in 1986 and 1988, respectively. His work experience include heading the Technical Training Division of Intel's Assembly and Test Facility in the Philippines, research positions at the East West Center in Hawaii and at the Massachusetts Institute of Technology, and a faculty position as an Assistant Professor of Electrical Engineering at the University of Rochester, NY. In 1989, Dr. Ang joined the Department of Mechanical Engineering of the National University of Singapore, where he is currently an Associate Professor. In addition to academic and research activities, he is actively involved in the Singapore Robotic Games as its founding chairman. His research interests span the areas of robotics, mechatronics, automation, computer control and applications of intelligent systems methodologies.



Oussama Khatib is Professor of Computer Science at Stanford University. He received his PhD in 1980 from Sup'Aero, Toulouse, France. His current research is in human-centered robotics, human motion synthesis, humanoid robots, dynamic simulations, haptic interactions and human-friendly robot design. His exploration in this research ranges from the autonomous ability of a robot to cooperate with a human to the haptic interaction of a user with an animated character or a surgical instrument. His research in these emerging areas builds on a large body of studies he pursued over the past 25 years and published in over 200 contributions in the field. He was Program Chair of ICRA2000 (San Francisco) and Editor of *The Robotics Review*, MIT Press. He has served as the Director of the Stanford Computer Forum, an industry affiliate program. He is currently the President of the International Foundation of Robotics Research, IFRR, and Editor of *STAR, Springer Tracts in Advanced Robotics*. He is an IEEE Fellow, a Distinguished Lecturer of IEEE and a recipient of the JARA Award.



Tao Ming Lim received his BEng degree (Hons) in Mechanical Engineering from National University of Singapore (NUS) in 1998. He continued to pursue his Master degree with NUS and worked as a research student in Singapore Institute of Manufacturing Technology (SIMTech). His Master research project was in Software Architecture for Real-Time Robotic Control. He joined SIMTech in 2001 after completing his Master Degree. His current research projects include the NUS-SIMTech collaborative research project in developing a robust mobile manipulator for unstructured environment and nano precision stage for 2D/3D wafer inspection system.



Ser Yong Lim received his BEng, 1st Class Honours, from the National University of Singapore in 1984, and his MSc, and PhD from Clemson University (Clemson, SC, USA), in 1988 and 1994, respectively. He has many years of working experience in the industry. In 1994, Dr. Lim joined Singapore Institute of Manufacturing Technology where he is now a Senior Scientist and Deputy Executive Director on Research. His main research interests are in nonlinear control of robotic manipulators, ultra-precision systems, force-controlled robots and real-time systems. He is now leading two research projects, one on robot dynamic control and the other on ultra-precision positioning systems.

Copyright of Advanced Robotics is the property of VSP International Science Publishers and its content may not be copied or emailed to multiple sites or posted to a listserv without the copyright holder's express written permission. However, users may print, download, or email articles for individual use.

Optimization of Failure-Tolerant Workspaces for Redundant Manipulators

Rodrigo S. Jamisola, Jr.

Electronics and Communications Engineering Dept. De La Salle University – Manila 201 Taft Ave.,
1004 Manila

For a redundant manipulator a region in its workspace that is guaranteed failure tolerant, called the failure-tolerant workspace, promises completion of critical tasks placed within it. By judiciously choosing a set of artificial joint limits which constrain the acceptable robot configurations prior to a failure, a failure-tolerant workspace can possibly exist even for manipulators with a single degree of redundancy. This work identifies the candidate boundaries of failure-tolerant workspaces, and presents justification on their validity and completeness. Based on the identified boundaries, optimization results for a 3-degree-of-freedom (dof) planar manipulator, as well as for a 4-dof planar manipulator, are presented. It assumed that the manipulator has the ability to lock a joint that has failed, and that the manipulator's workspace degree of freedom remains the same before and after a joint failure.

KEYWORDS

robotics, robot motion planning, kinematics failure tolerance, reachable workspace, optimization

I. INTRODUCTION

An extra joint in kinematically redundant manipulators creates greater dexterity in task execution. For the end-effector location of a kinematically redundant manipulator, an infinite

number of postures (called configurations) correspond to the same workspace location. With the extra joint, the redundant manipulator can perform the required workspace task and, at the same time, vary its posture to perform obstacle avoidance, manipulability optimization, failure tolerance, and other desired posture optimization criteria.

In this work, the posture optimization criterion would be that of tolerance to joint failure, such that the manipulator would be able to perform the required workspace task before and after the occurrence of a joint failure. The manipulator joints are allowed to be locked in failure such that the workspace degree of freedom remains constant.

Tolerance to joint failure has gained popularity among robot researches because, when addressed properly, the robot manipulator can be guaranteed to complete critical tasks despite one or more of its joints failing. This is especially applicable when the robot is tasked to perform work in remote or hazardous environments where direct human intervention, in the case of joint failures, is not possible. For example, robots working in nuclear waste disposal or robots that perform deep underwater explorations, or robots that are sent to space. In these cases, robot repair during joint failures could mean additional cost due to the delay, or could possibly pose danger to human life.

When a failure-tolerant workspace for a given robot is already identified, the robot user will only have to specify locations of critical tasks to be within this region in order to guarantee completion despite one or more of the robot's joints failing. Further, identifying the maximum possible region of such a workspace would mean more tasks that can be possibly specified at a given time for the manipulator.

Email Address: rodrigo.jamisola@dlsu.edu.ph

Submitted: August 29, 2009

Revised: March 24, 2010

Accepted: March 24, 2010

Published: April 16, 2010

Editor-in-charge: Eduardo A. Padlan

From the pioneering work on kinematic failure tolerance for redundant manipulators (Maciejewski 1990), many related studies have been performed. These include design enhancement for failure tolerance including kinematic redundancy and dual actuation (Monteverde and Tosunoglu 1997), presentation of an analysis tool to determine the fault-tolerant workspace when no joint limits are considered (Paredis and Khosla 1994), failure tolerance in the domain of mechanical systems (Sreevijayan et al. 1994), failure tolerance by considering both kinematics and dynamics of the manipulator (Li and Gruver 1998), examination of the reduced manipulability of a manipulator after one or more joint failure (Roberts and Maciejewski 1996), real-time implementation (Groom et al. 1999), and when obstacles in the environment are considered (Paredis and Khosla 1996).

Among the more recent studies in kinematic failure tolerance include failure tolerance for cooperative manipulators rigidly connected to a solid object (Tinos et al. 2002), fault detection and tolerance for static walking of rigid robots, where each leg has three revolute joints (Yang 2002), fault tolerance for parallel manipulators using task space and kinematic redundancy (Yi et al. 2006), characterization of optimally fault-tolerant manipulators based on relative manipulability index (Roberts et al. 2007), designing the nominal manipulator Jacobian for optimal fault tolerance to one or more joint failures, especially for parallel mechanisms (Roberts et al. 2008), quantification of optimal fault-tolerant manipulability for Stewart platforms (Ukidve et al. 2008), and using neural network for failure-tolerant control of redundant robots (Srinivasa and Grossberg 2007).

A new approach to obstacle avoidance with failure tolerance is shown in Jamisola et al. (2003) and Jamisola et al. (2006). The existence of an obstacle-free surface in the configuration space (C-space) with no local minimum guarantees task completion despite joint failures and obstacles in the workspace. Start and goal locations were specified and the position of the obstacles was known. A related problem to the mentioned work is to identify the workspace region that is known to be tolerant to failure, without consideration for obstacles. A previous work (Paredis and Khosla 1996) stated that one needs at least two degrees of redundancy for a failure-tolerant workspace to exist on a given redundant manipulator. This limitation was overcome by imposing artificial joint limits prior to a failure (Lewis and Maciejewski 1997). Because reachability of workspace locations after a failure is dependent on the manipulator configuration at the instance of failure, constraining the allowable joint values prior to a failure will ensure certain workspace locations to remain reachable after a joint failure.

A more recent work showed that the boundaries of the failure-tolerant workspace are identifiable (Roberts et al. 2007). This removed significant computational burden because, instead of computing for the entire failure-tolerant region, only its boundaries are identified. However, for much higher degrees of redundancy this may not be necessarily true.

This work will try to build on the results of Roberts et al. (2007) and will present justifications on the validity and completeness in identifying the candidate boundaries of the failure-tolerant workspace. In addition, optimal results and analysis for a 3-dof planar manipulator with constant and variable link lengths, as well as for a planar 4-dof manipulator with constant link lengths, will be presented. Planar manipulators are chosen as implementation platforms for simplicity and clearer presentation of results. The 3-dof planar manipulator (both constant and variable link lengths) is used to illustrate the case where only a single joint failure is allowed, while the 4-dof planar manipulator (with equal link lengths) is shown for the case where one or two joints can fail at any given time. Higher degrees of freedom workspaces will be considered in future implementations.

II. AN OVERVIEW OF THE PROPOSED APPROACH

Before proceeding with the gradient method of identifying the optimal failure-tolerant workspace, a global brute-force computation of the 3-dof robot with equal link lengths was performed. The value of the artificial joint limits was varied and the corresponding failure-tolerant workspaces are computed. The results shown in Fig. 1, which approximately agrees with the optimal results found in Lewis and Maciejewski (1997), gave a global perspective on the extent of the failure-tolerant workspace region as the artificial joint limits were varied. For redundant manipulators, a workspace location $\mathbf{x} \in \mathbb{R}^m$ and a manipulator configuration $\mathbf{q} \in \mathbb{R}^n$ such that $n > m$. The Jacobian matrix relates the incremental change in the manipulator configuration, $\delta\mathbf{q}$, to that of the incremental change in the manipulator end-effector location, $\delta\mathbf{x}$,

$$\delta\mathbf{x} = \mathbf{J} \delta\mathbf{q} \quad (1)$$

where $\mathbf{J} \in \mathbb{R}^{m \times n}$. A given manipulator's reachable workspace, without consideration to joint failures, will be called a normal workspace and labeled \mathbf{W} . When joint failures are considered, the resulting reachable workspace after a failure is dependent on the manipulator configuration at the instance of failure. Thus the resulting failure-tolerant workspace is dependent on the allowable range of joint values imposed on the manipulator prior to a failure. For a given manipulator, the problem becomes that of searching for a set of artificial joint limits that will maximize the failure-tolerant workspace. In the event of a joint failure, the artificial joint limits are released and the physical limits become the new joint limits. The failure-tolerant workspace is labeled \mathbf{W}_S (S for "safe"). A reachable workspace location is tolerant to a joint failure if it remains reachable after a failure. This location is labeled as \mathbf{x}_S such that $\mathbf{x}_S \in \mathbf{W}_S$. Because the manipulator configuration at the instance of failure is not known, one has to consider all the possible \mathbf{W} 's for every possible joint failure to be able to identify \mathbf{W}_S . The intersection of all the possible workspaces corresponding to every possible joint failure(s) is labeled \mathbf{W}_F (F for "failed"). This workspace can also be interpreted as the workspace that is guaranteed reachable after

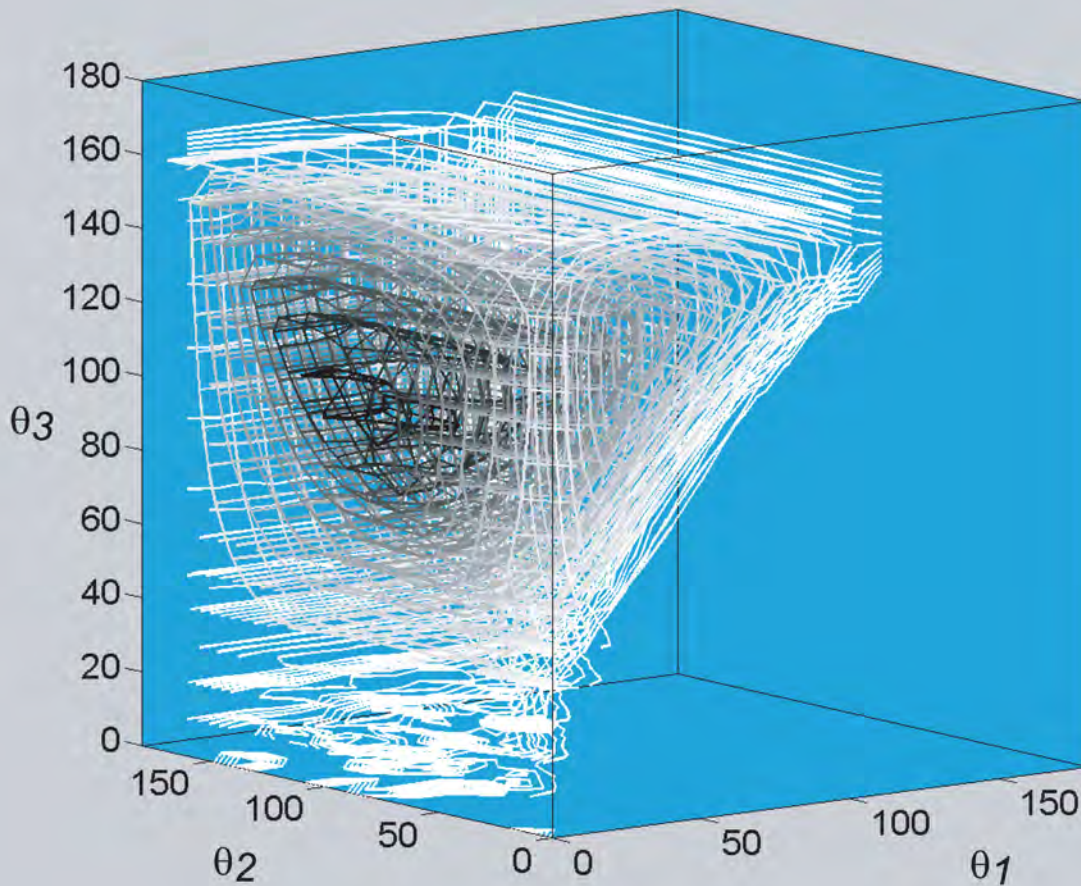


Figure 1. A global plot of the failure-tolerant workspace for a 3-dof planar manipulator with equal link lengths. The plot has a resolution of 10 degrees such that the black contours are approximately 4000 sq. units, the gray contours are approximately 2000 sq. units, and the white contours are approximately 1 sq. unit. It is shown that the maximum area lies around the range of $\theta_1 = [0, 50]$, $\theta_2 = [50, 150]$, and $\theta_3 = [80, 120]$ degrees.

any joint failure. The reachable workspace prior to a joint failure is labeled W_O (O for “original”). The resulting W_S is the intersection of W_F and W_O ,

$$W_S = W_O \cap W_F. \quad (2)$$

Techniques will be discussed on how to identify the boundaries of W_S to ease the burden of computation.

III. CANDIDATE BOUNDARIES OF THE FAILURE-TOLERANT WORKSPACE

For a normal workspace W , a reachable workspace location \mathbf{x} lies at the boundary if there exists a small incremental displacement $\delta\mathbf{x}$ such that $\mathbf{x} + \delta\mathbf{x}$ is not reachable. It is

characterized by either a manipulator singularity or a joint limit singularity, also called semi-singularity (Luck 1995). This

is formally stated below.

Definition 1. *The boundaries of a normal workspace are characterized by either manipulator singularities or joint limit singularities.*

When a joint failure occurs, the resulting failed manipulator will have a corresponding new reachable workspace W' whose boundaries now correspond to the singularities of the resulting failed manipulator and singularities of the new joint limits. From Eqn. 2 and assuming W_S exists, the boundaries of W_S are characterized by the singularities of the original manipulator, the singularities of the failed manipulator, and the joint limit singularities. At this point, we have sufficiently described the candidate boundaries of W_S . Let us formally present this statement below.

The boundaries of a failure-tolerant workspace can be characterized by three types of manipulator singularities:

- Singularity of the original manipulator
- Singularity of the failed manipulator
- Joint limit singularity

Justification for their validity will be presented. Because the workspaces consisting W_F are infinitely many, further discussion will be given on how to identify the boundaries of W_F by considering only a number of workspaces that make up its boundaries. The true boundaries of W_S can be determined by checking the tolerance to failure of every candidate boundary.

A. Singularity of the Original Manipulator

Given a configuration \mathbf{q} such that $\det(\mathbf{J}\mathbf{J}^T)=0$. At $\mathbf{x} = \mathbf{f}(\mathbf{q})$ the manipulator loses at least one degree of freedom such that there exists an $\mathbf{x}+\delta\mathbf{x}$ that is not reachable. The location \mathbf{x} is said to correspond to an escapable singularity if there exists a different configuration \mathbf{q}' such that $\mathbf{x} = \mathbf{f}(\mathbf{q}')$ and $\mathbf{x}+\delta\mathbf{x}$ becomes reachable for all $\delta\mathbf{x}$'s. In this case, \mathbf{x} does not lie on a true boundary of W .

On the other hand, a different location \mathbf{x} is said to correspond to an inescapable singularity if $\mathbf{x}=\mathbf{f}(\mathbf{q})$ and $\det(\mathbf{J}\mathbf{J}^T)=0$ for all \mathbf{q} 's corresponding to \mathbf{x} . In this case, \mathbf{x} lies at a workspace boundary. In equation form,

$$\mathbf{x} \in \partial W \text{ if } \mathbf{x} = \mathbf{f}(\mathbf{q}) \text{ and } \det(\mathbf{J}\mathbf{J}^T)=0 \quad \forall \mathbf{q} = \mathbf{f}^{-1}(\mathbf{x}) \quad (3)$$

where ∂W is the boundary of the workspace W . We are now ready to characterize the singularity of the original manipulator as a candidate boundary of W_S .

Lemma 1: Singularity of original manipulator characterizes a candidate boundary of the failure-tolerant workspace.

Proof: From Def. 1, the singularity of the original manipulator characterizes the boundaries of W_O , such that a workspace location \mathbf{x} corresponding to an inescapable singularity lies exactly at the boundary of W_O from Eqn. 3. By Eqn. 2, a boundary of W_O may lie at the boundary of W_S which makes the singularity of the original manipulator a candidate boundary of W_S .

In an event of a failure, an escapable singularity of the original manipulator may become an inescapable singularity of the resulting failed manipulator. This will correspond to the second candidate boundary of W_S .

B. Singularity of the Failed Manipulator

Let \mathbf{J}_F be the Jacobian of the resulting manipulator after a failure where the corresponding column(s) of the failed joint(s) is truncated, such that $\mathbf{J}_F \in \mathbb{R}^{m \times p}$ and $p=n-1, \dots, m$. To search for the singularity of the every possible failed manipulator is to search for every possible \mathbf{J}_F and its corresponding $\det(\mathbf{J}_F\mathbf{J}_F^T) = 0$.

Lemma 2: Singularity of the failed manipulator characterizes a candidate boundary of the failure-tolerant workspace.

Proof: Let us consider that the failed manipulator is a different manipulator that is independent from the original one. By Def. 1, the new workspace boundaries can be characterized by the singularities of its corresponding new manipulator, such that the inescapable singularities exactly lie at its boundaries. Because W_F results from the intersection of all these possible new workspaces, from Eqn. 2 the boundaries of each new workspace are possible boundaries of W_F as well as of W_S .

Not all new workspaces resulting from a failure will define the boundaries of W_F . It is imperative to be able to characterize the boundaries of W_F to lessen the computational burden.

C. Joint Limit Singularity

Joint limit singularity is further subdivided into two types: tangent and edge singularities. A tangent singularity is equivalent to the singularity of the failed manipulator when the joint failed at the limit. An edge singularity corresponds to a configuration at the edge (or corner) of the C-space.

Lemma 3: Joint limit singularity characterizes a candidate boundary of the failure-tolerant workspace.

Proof: By Definition 1, joint limit singularities characterize the boundaries of W_O . For every possible joint failure, a new set of joint limits will characterize each resulting manipulator's workspace, and are candidate boundaries of W_F as well as of W_S .

As in the failed manipulator singularity, the joint limit singularity also considers every possible failed manipulator's workspace. This section sufficiently identifies all the candidate boundaries of W_S .

IV. CHARACTERIZING THE CANDIDATE BOUNDARIES OF W_F

To present justification for the candidate boundaries of W_F , we first introduce the concept of *self-motion manifolds*. The self-motion manifolds of workspace location $\mathbf{x} = \mathbf{f}(\mathbf{q})$ are disjoint connected subsets of the pre-image $\mathbf{f}^{-1}(\mathbf{x})$. Given a manipulator with r -degree of redundancy,

$$\mathbf{f}^{-1}(\mathbf{x}) = \bigcup_{i=1}^N M_i \quad (4)$$

where M_i is the r -th dimensional self-motion manifold and N is the number of self-motion manifolds, such that when $i \neq j$, $M_i \cap M_j = \emptyset$ (Burdick 89).

From Eqn. 2 and given a failure-tolerant workspace location \mathbf{x} we can state that

$$\mathbf{x} \in W_S \Leftrightarrow \mathbf{x} \in W_O \text{ and } \mathbf{x} \in W_F. \quad (5)$$

The first term can be satisfied if there exists at least one configuration \mathbf{q} such that $\mathbf{x} = \mathbf{f}(\mathbf{q})$ is reachable before a joint failure. The second term is trickier by the fact that for a given workspace location \mathbf{x} , there must exist a connected portion of the self-motion manifold, within the joint limits, that can maintain reachability of \mathbf{x} after a joint failure. This will guarantee reachability of \mathbf{x} for any joint failures within the set limits.

Definition 2. A workspace location is guaranteed reachable after a joint failure if there exists a connected portion of the self-motion manifold that spans the entire range of values within the joint limits.

We are now ready to identify the candidate boundaries of W_F . This is stated as a theorem below.

Theorem 1: The changes in the topology of the C-space characterize the candidate boundaries of W_F .

Proof: The satisfaction of the failure-tolerance test, i.e., reachability of \mathbf{x} for any joint failure, is dependent on the connectedness of the corresponding self-motion manifold within the set limits. A topological change in the C-space results in a characteristic change of the self-motion manifolds and their connectedness. As a manipulator configuration passes through a topological change in the C-space, the satisfaction of the failure-tolerance test can vary. Such possible variation in the satisfaction of the failure-tolerance test characterizes the candidate boundaries of W_F .

The changes in the C-space topology can be internal or at a C-space boundary. An internal C-space topological change occurs at the original manipulator's singularity, while the topological change at the C-space boundary occurs at a joint limit singularity.

The self-motion manifold corresponding to an escapable singularity of the original manipulator may span an entire range of a set of joint values in the configuration space.

When this set of joint values corresponds to the possible joint failures, failure tolerance is guaranteed. Its adjacent self-motion manifolds may not be connected within the limit.

The self-motion manifold that is tangent at a joint limit has the possibility of satisfying the failure-tolerance test for the corresponding joint. Close to it, there exists another self-motion manifold that fell short of touching the joint limit and therefore cannot satisfy the connectedness within the limit.

At the edge of the C-space, a self-motion manifold intersects more than one joint limit. This self-motion manifold may satisfy the failure-tolerance test for the corresponding joint limit. At its

vicinity, another self-motion manifold that intersects only one joint limit cannot satisfy the failure-tolerance test of the other joint limit.

Now that the candidate boundaries of W_F are identified, the candidate boundaries of W_S are modified as follows:

- Singularity of the original manipulator
- Tangent singularity
- Edge singularity

The next subsection will be a step-by-step approach of finding the candidate boundaries of W_S .

V. ALGORITHM OF THE PROPOSED APPROACH

Consider that a failure-tolerant workspace exists for a given manipulator and a set of artificial joint limits. The boundaries of W_S are identified through the following steps:

- 1) Search for the singularities of the original manipulator, $\det(\mathbf{J}\mathbf{J}^T) = 0$, and compute their corresponding workspace locations.
- 2) Search for the tangent singularities such that $\det(\mathbf{J}_F\mathbf{J}_F^T) = 0$ for $p = n - 1, \dots, m$, and compute for their corresponding workspace locations.
- 3) Search for the edge singularities and compute for their corresponding workspace locations.
- 4) Determine the intersections between the candidate boundaries.
- 5) Test each segment of the candidate boundaries for tolerance to joint failures.

VI. OPTIMAL FAILURE-TOLERANT WORKSPACES

The optimal results shown in this work used planar workspaces. The joint limits are symmetric and so are the resulting W_S 's thus the area computation is performed on one side of W_S and is multiplied by two. Symmetry of the joints limits are commonly used by industrial robots. The area of the failure-tolerant workspace was computed by taking the integral for each true boundary over a free joint, that is,

$$A_{WS} = 2 \sum_{i=1}^{n_B} \int_{q_{ia}}^{q_{ib}} \mathbf{B} dq_i \quad (6)$$

where A_{WS} is the area of W_S , \mathbf{B} is a segment of the true boundary, q_{ia} and q_{ib} are the limits of the free joint q_i , and n_B is the number of segments of the true boundary. Optimization computation was performed using the gradient ascent method such that at every computational cycle t ,

$$\mathbf{v}^{(t+1)} = \mathbf{v}^{(t)} + \left[\gamma \frac{\partial A_{WS}}{\partial \mathbf{v}} \right]^{(t)} \quad (7)$$

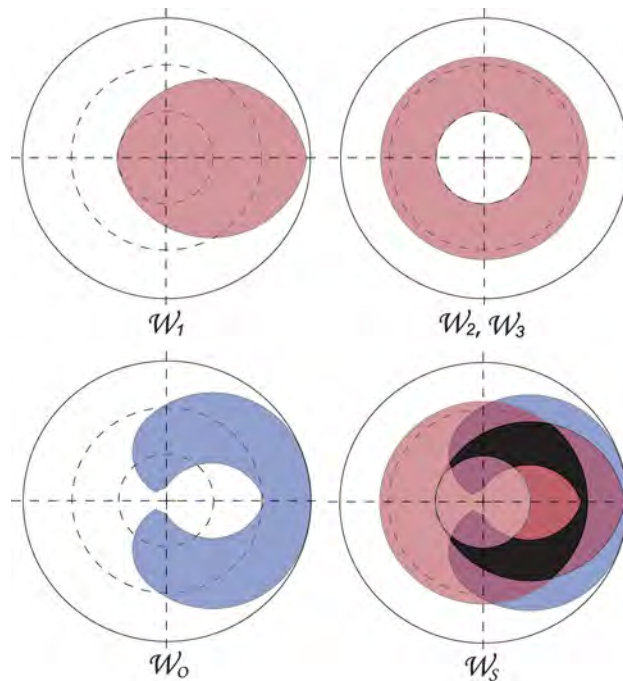


Figure 2. The optimal W_s for a 3-dof robot with equal link lengths is shown. The workspaces W_1 , W_2 , and W_3 are the W_F 's for the corresponding joint failure. The symmetric artificial joint limits are $[(+/-)18, (+/-)111, (+/-)111]^T$ degrees, and W_s has an area of 3.56 sq. units where each link has 1 unit length.

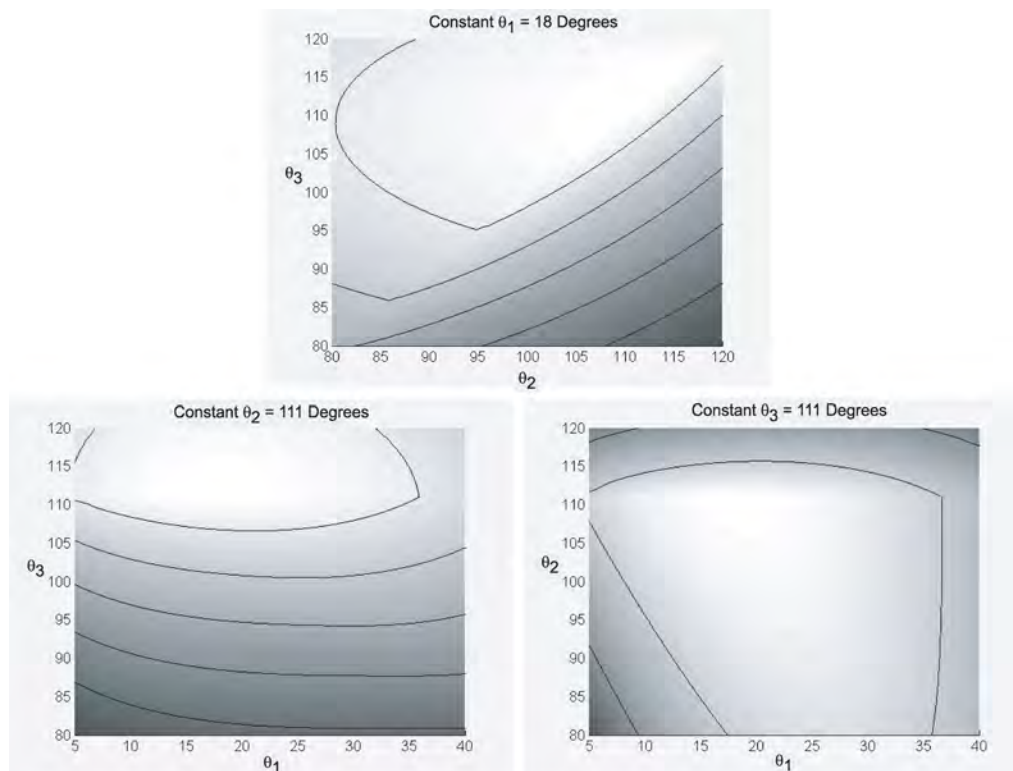


Figure 3. The figure shows the plots of A_{ws} at the slices of the optimal artificial joint limits of $[(+/-)18, (+/-)111, (+/-)111]^T$ degrees for the 3-DOF planar robot with equal link lengths. The contour lines are at 0.313 sq. units apart. The white portion shows the vicinity of the optimal A_{ws} .

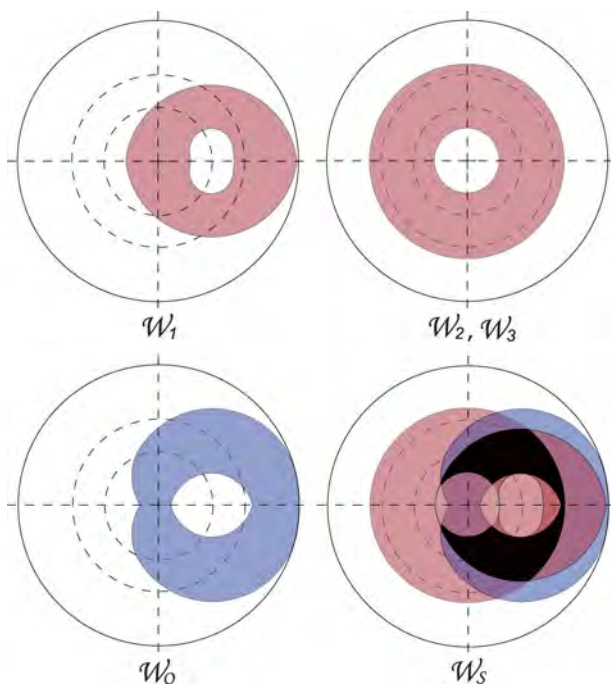


Figure 4. The figure shows the optimal W_s of a 3-dof robot that is kinematically designed to maximize $A_{ws} = 3.71$ sq. units. The optimal W_s is shown as the black region. The link lengths are $[1.2, 0.6, 1.2]^T$ units with symmetric artificial joint limits of $[(+/-)11, (+/-)128, (+/-)128]$ degrees

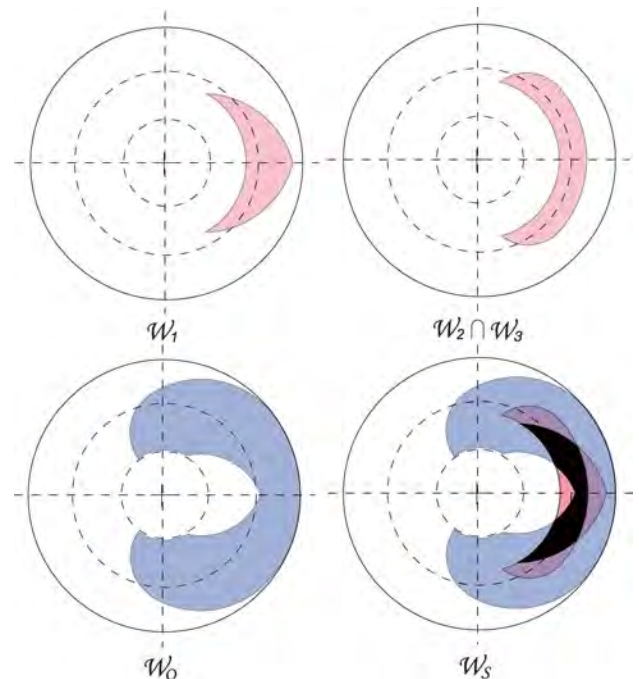


Figure 6. Optimized $A_{ws} = 0.3380 \text{ m}^2$ for the PA-10 that is used as a 3-dof planar robot is shown. The link lengths are $[0.45, 0.5, 0.45]^T \text{ m}$, the artificial joint limits are $[(+/-)32, (+/-)92, (+/-)92]^T$ degrees, and the physical limits are $[(+/-)90, (+/-)135, (+/-)160]^T$ degrees.

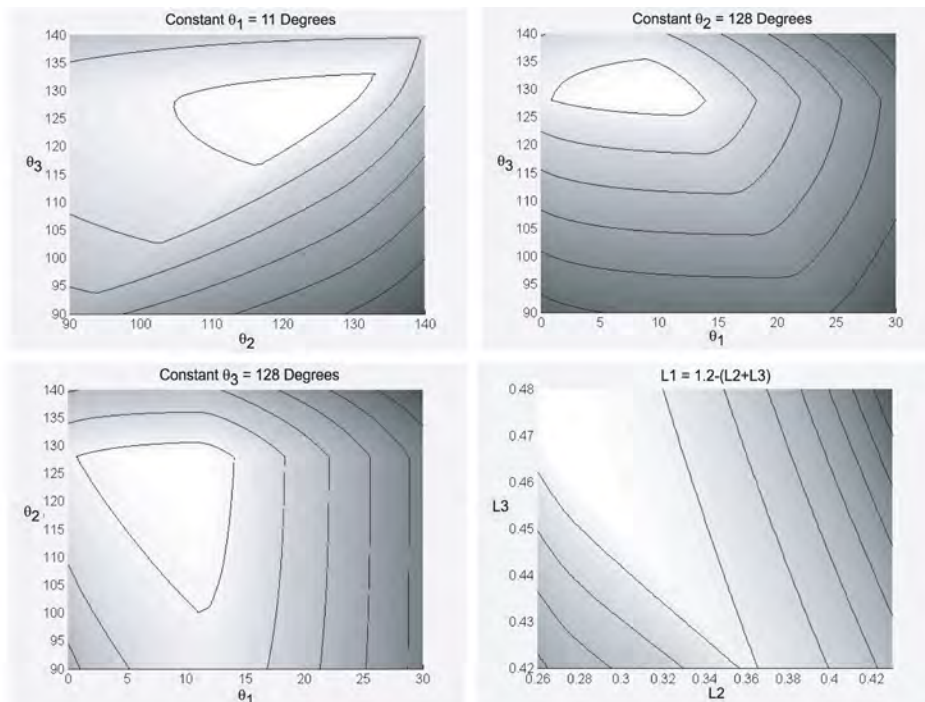


Figure 5. The figure shows slices at the optimal A_{ws} in Fig. 4. The contour lines are at 0.313 sq. units apart. The white portion shows the vicinity of the optimal A_{ws} . Three subfigures show the slices where one of the optimal artificial joint limits and the optimal link lengths are held constant. The fourth subfigure showed $L1 = 1.2 - (L2 + L3)$, and all optimal artificial limits are constant.

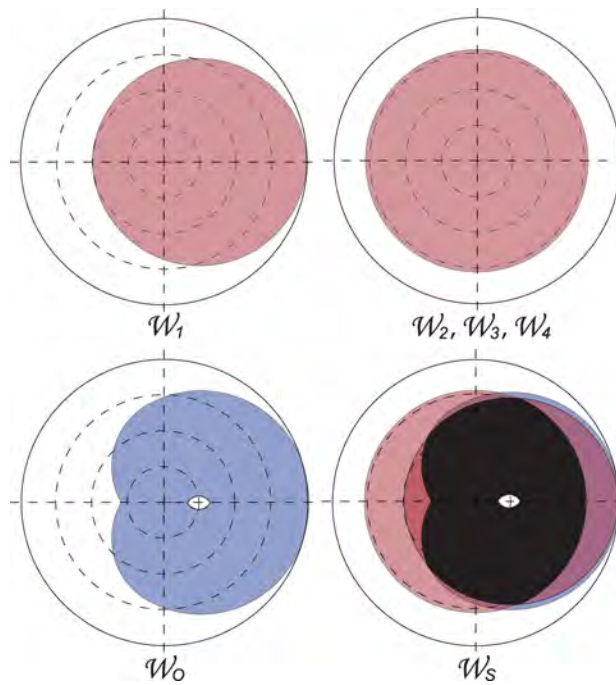


Figure 7. The figure shows the corresponding workspaces for a 4-dof planar robot with equal link lengths $[0.3, 0.3, 0.3, 0.3]^T$ units and the optimal artificial limits $[(+/-)7, (+/-)110, (+/-)110, (+/-)110]^T$ degrees such that its workspace is identical to that of the 3-dof planar robot.

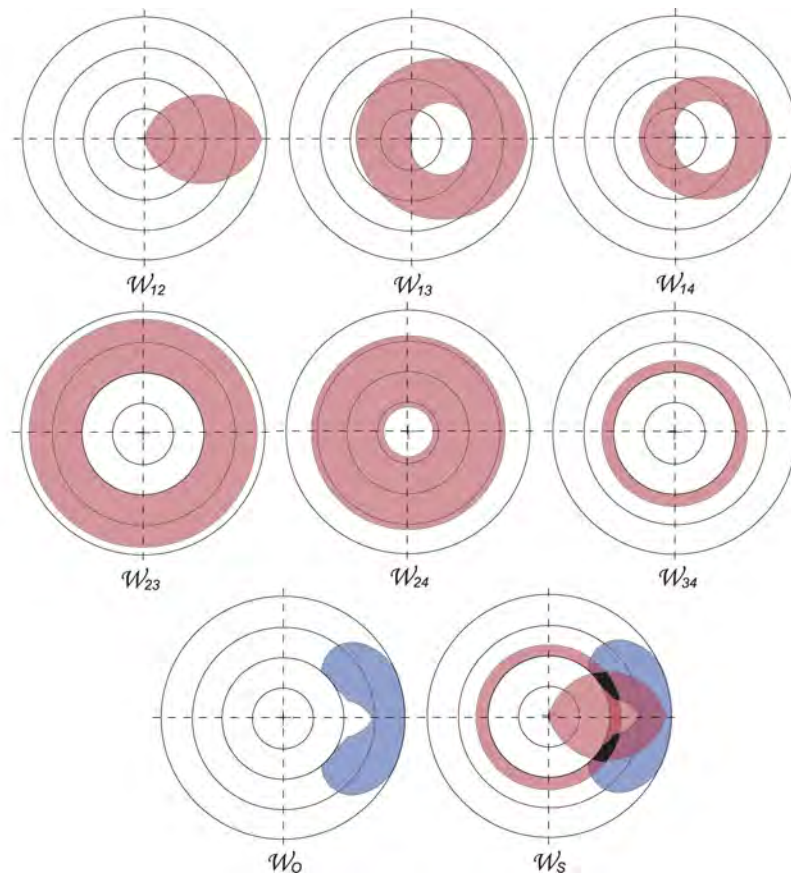


Figure 8. An optimal case for a 4-dof planar with two joints failing is shown in the figure that has an area of $A_{ws} = 0.0581$ sq. units. The link lengths are equal at $[0.3, 0.3, 0.3, 0.3]^T$ units and the artificial joint limits are $[(+/-)11, (+/-)11, (+/-)48, (+/-)107]^T$.

where \mathbf{v} can be a function of both artificial joint limits and link lengths when manipulator design is considered, and γ is the step size. Because the computation is local in nature, random starting values for the variable \mathbf{v} were used, and random steps around the vicinity of a local maximum were taken until the maximum allowable computational cycle is reached. The vicinity of the optimal value for the 3-dof equal link length case has been previously known from the brute-force computation, so the starting configuration for this case was easily chosen.

Optimization results for 3-dof planar robot with equal link lengths, and of a 3-dof planar robot with variable link lengths will be presented. To support the validity of these results, the information regarding the C-space slices at the optimal failure-tolerant workspace value is shown. In addition, optimal results of the PA-10 robot that is used as a 3-dof planar robot, of a 4-dof planar robot with single joint failure, and of a 4-dof planar robot with 2-joint failure are presented.

Optimal results of a 3-dof planar robot with equal link lengths are shown in Fig. 2. The workspaces \mathbf{W}_i 's are the \mathbf{W}_F 's for the corresponding joint i . Slices at the optimal value of A_{ws} corresponding to a symmetric artificial joint limits of $[(+/-)18, (+/-)111, (+/-)11]^T$ are shown in Fig. 3. The white portion is the vicinity of the optimal value. At each slice, an artificial joint limit value is held constant while the other two artificial joint limits are linearly varied. The contour lines are at 0.313 sq. units apart. This optimal value is a 13% increase to that found in Lewis and Maciejewski (1997).

The ridge for each subfigure in Fig. 3 corresponds to the switching of the candidate boundary (due to tangent singularity) between \mathbf{W}_2 and \mathbf{W}_3 , depending on which one is a true boundary. The artificial joint limits for joints 2 and 3 have to be equal to maximize the region of intersection between \mathbf{W}_2 and \mathbf{W}_3 . Its outer boundary is the most influential boundary of \mathbf{W}_s such that a change in the joint 2 or 3 value can significantly decrease the area of \mathbf{W}_s , as shown in Fig. 3.

The second case considers a 3-dof planar robot such that its links are allowed to vary in lengths. The resulting \mathbf{W}_O is identical to the equal link length case. The optimal result has a link lengths of $[1.2, 0.6, 1.2]^T$, and the artificial joint limits are $[(+/-)11, (+/-)128, (+/-)128]^T$ degrees. Due to the links not being equal, \mathbf{W}_1 has an inner boundary as shown in Fig. 4. Intuitively, one may think that the optimal value of A_{ws} compared to the equal link case is lesser because of this. However in the resulting optimal \mathbf{W}_s , the hole did not have any contribution when all its corresponding boundaries were intersected. In addition, the location of the inner boundary of \mathbf{W}_2 and \mathbf{W}_3 is closer to the origin compared to the equal link length case. The resulting A_{ws} has a 4.2% increase from the equal link length case.

Slices at the optimal A_{ws} for the 3-dof with variable link lengths are shown in Fig. 5. For the first three subfigures, two joint limits values are varied and the other joint limit and the link lengths are held constant at the optimal value. The fourth

subfigure held the optimal artificial joint limits constant while the L_2 and L_3 link lengths are varied, such that $L_1 = 1.2 - (L_2 + L_3)$. Ridges on the topology have similar characteristics as those of the equal link length case, for the subfigures where the link lengths are held constant and the joint values are changing. An additional ridge that is less sharp is due to the hole in the workspace created by the inner boundary of \mathbf{W}_1 . The ridge in fourth subfigure is caused by the switching of the boundaries of \mathbf{W}_2 and \mathbf{W}_3 , whichever becomes the true boundary.

Optimization of A_{ws} for the PA-10 that is used as a 3-dof planar robot is shown in Fig. 6. Links 2, 4, and 6 with link lengths $[0.45, 0.5, 0.45]^T$ m and physical limits $[(+/-)90, (+/-)135, (+/-)160]^T$ degrees were used. The rest of the links were locked. At the optimal $A_{ws} = 0.3380 \text{ m}^2$ the artificial joint limits are $[32, 92, 92]^T$ degrees. This example shows the case when physical limits were present. It upholds the fact that present industrial robots with a single degree of redundancy have the ability to become failure tolerant by judiciously constraining the joint values prior to a failure.

In considering the 4-dof planar robot, the link lengths were chosen to be equal to each other at $[0.3, 0.3, 0.3, 0.3]^T$ units such that its \mathbf{W}_O is identical to that of the 3-dof equal link length case. For a single locked-joint failure, the problem becomes that of a 3-dof planar robot where one of its link lengths is derived from the configuration of the locked joint. The optimal results are shown in Fig. 7. The optimal $A_{ws} = 1.9115$ sq. units and the corresponding set of artificial joint limits are $[(+/-)7, (+/-)110, (+/-)110, (+/-)110]^T$ degrees. The shown optimal A_{ws} is 3.2 times that for the kinematically designed.

When two joints are allowed to fail in the 4-dof planar robot, the optimal \mathbf{W}_s area is reduced significantly as shown in Fig. 8. The workspaces \mathbf{W}_{ij} 's are the \mathbf{W}_F 's for the corresponding joints i and j . Not all \mathbf{W}_F 's from two joints failing define the boundaries of \mathbf{W}_s . It is shown that the boundaries are defined by \mathbf{W}_O , \mathbf{W}_{12} , and \mathbf{W}_{34} .

VII. SUMMARY AND CONCLUSION

This work has characterized the candidate boundaries of failure-tolerant workspaces, and has presented justifications on their validity and completeness. Optimal results for planar manipulators with single as well as double joint failures were presented. This work further supported the claim that failure-tolerant workspaces exists, even for present industrial robots with a single degree of redundancy. Future research work is geared towards optimizing failure-tolerant workspaces for full-spatial redundant manipulators.

VIII. ACKNOWLEDGEMENTS

The author gratefully acknowledges the contributions of Prof. Anthony A. Maciejewski and Prof. Rodney G. Roberts.

REFERENCES

- Burdick JW. On the inverse kinematics of redundant manipulators: Characterization of the self-motion manifolds. In *IEEE Int Conf Robot Automat*, pages 264–270, Scotsdale, AZ, May 14-19, 1989.
- Groom KN, Maciejewski AA, Balakrishnan V. Real-time failure-tolerant control of kinematically redundant manipulators. *IEEE Trans Robot Automat* 1999; 15:1109–1116.
- Jamisola RS Jr, Maciejewski AA, Roberts RG. A path planning strategy for kinematically redundant manipulators anticipating joint failures in the presence of obstacles. In *IEEE/RSJ Int Conf Intell Robots Syst*, pages 142–148, Las Vegas, NV, Oct 27-31, 2003.
- Jamisola RS Jr, Maciejewski AA, Roberts RG. Failure-tolerant path planning for kinematically redundant manipulators anticipating locked-joint failures. *IEEE Trans Robot* 2006; 22:603–612.
- Li L, Gruver WA. Fault-tolerant control of redundant robots by dual-optimization. In *IEEE/RSJ Int Conf Intell Robots Syst*, pages 336–341, Victoria, Canada, Oct 13-17, 1998.
- Lewis CL, Maciejewski AA. Fault tolerant operation of kinematically redundant manipulators for locked joint failures. *IEEE Trans Robot Automat* 1997; 13:622–629.
- Luck CL. Robot Cartography: A Topology-Based Representation for the Global Kinematic Control of Redundant Manipulators under Constraints. PhD thesis, Univ. of South. California, 1995.
- Maciejewski AA. Fault tolerant properties of kinematically redundant manipulators. In *IEEE Int Conf Robot Automat*, pages 638–642, Cincinnati, OH, May 13-18, 1990.
- Monteverde V, Tosunoglu S. Effect of kinematic structure and dual actuation on fault tolerance of robot manipulators. In *IEEE Int Conf Robot Automat*, pages 2902–2907, Albuquerque, NM, April 20-25, 1997.
- Paredis CJJ, Khosla PK. Mapping task into fault tolerant manipulators. In *IEEE Int Conf Robot Automat*, pages 696–703, San Diego, CA, 1994.
- Paredis CJJ, Khosla PK. Designing fault-tolerant manipulators: How many degrees of freedom? *Int J Robot Res* 1996; 15:611–628.
- Roberts RG, Jamisola RS Jr, Maciejewski AA. Identifying the failure-tolerant workspace boundaries of a kinematically redundant manipulators. In *IEEE Int Conf Robot Automat*, pages 4517–4523, Roma, Italy, April 10-14, 2007.
- Roberts RG, Maciejewski AA. A local measure of fault tolerance for kinematically redundant manipulators. *IEEE Trans Robot Automat* 1996; 12:543–552.
- Roberts RG, Yu HG, Maciejewski AA. Characterizing optimally fault-tolerant manipulators based on relative manipulability indices. In *IEEE/RSJ Int Conf Intell Robots Syst*, pages 3925–3930, San Diego, CA, Oct 29-Nov 2, 2007.
- Roberts RG, Yu HG, Maciejewski AA. Fundamental limitations on designing optimally fault-tolerant redundant manipulators. *IEEE Trans Robot* 2008; 24:1224–1237.
- Srinivasa N, Grossberg S. A self-organizing neural model for fault-tolerant control of redundant robots. In *Int. Joint Conf Neural Networks*, pages 483–488, Orlando, FL, Aug 12-17, 2007.
- Sreevijayan D, Tosunoglu S, Tesar D. Architectures for fault-tolerant mechanical systems. In *Medit Electrotech Conf*, pages 1029–1033, Antalya, Turkey, Apr 12-14, 1994.
- Tinos R, Terra MH, Bergerman M. Fault tolerance in cooperative manipulators. In *IEEE Int Conf Robot Automat*, pages 470–475, Washington, D.C., May 11-15, 2002.
- Ukideve CS, McInroy JE, Jafari F. Using redundancy to optimize manipulability of stewart platforms. *IEEE/ASME Trans Mechatron* 2008; 13:475–479.
- Yang JM. Fault-tolerant gaits of quadruped robot for locked joint failures. *IEEE Trans Syst Man Cybern C* 2002; 32:507–516.
- Yi Y, McInroy JE, Chen Y. Fault tolerance of parallel manipulators using task space and kinematic redundancy. *IEEE Trans Robot* 2006; 22:1017–1021.

Unibersidad ng Pilipinas

OFFICE OF THE

Alinsunod sa autoridad na ikinatawag ng Republika ng Pilipinas at batay sa rekomendasyon ng Komite ng Unibersidad, ipinagkakat ng Lupon ng mga Rehenste kay

Roberto S. Jamisola, Jr.
na nakatupad sa mga pangangailangan ng itinakdang kurso, ang titulong
Bachelor of Science in Mechanical Engineering

kasama ang lahat ng mga karapatan, karangalan at pribilehiyo, gayundin ang mga obligasyon at pananagutang nangangailangan.

Bilang Paggpapatunay nararito ang sagisag ng Unibersidad at ang mga lagda ng Pangulo, ng Chancellor, ng Dekano at ng Klathim ng Unibersidad. Ipinagkakat sa Lungsod Quezon, Pilipinas, sa ika 2, ng Nobyembre ng taong labing-wiyam siyamnapu't tatlo

Ernesto

Chancellor ng UP Diliman

Agustín A. V.

Dekano ng College of Engineering

Li Q. Jan

Pangulo ng Unibersidad

Olivia C. Carli

Klathim ng Unibersidad



THE NATIONAL UNIVERSITY
OF SINGAPORE



DEGREE OF
MASTER OF ENGINEERING

It is hereby certified that

Jamisola Rodrigo Jr Sarmiento

having satisfied the requirements prescribed by
Statute, was admitted to the Degree of Master
of Engineering on 25 June 2001

Vice-Chancellor

CFS



Colorado State University

The Board of Governors of the Colorado State University System
on recommendation of the Faculty has conferred upon

Rodrigo Sarmiento Jamizola Jr.
the Degree of

Master of Science
Electrical Engineering

Given under the seal of Colorado State University at Fort Collins, Colorado
this sixteenth day of December, two thousand and six.

Paul D. Biele
President of the University

[Signature]
Vice Provost for Graduate Studies



[Signature]
Chair of the Board

Ang Pangulo at mga Guro ng
The President and Faculty of



De La Salle University
Manila

Maynila, Republika ng Pilipinas
Manila, Republic of the Philippines

Sa lahat ng makakatunghay ng kasulatang ito, Mapitagang Bari sa Ngalan ng Maykapal
To all whom this diploma comes to view greetings in the Lord.

*Ipinababatid ng mga titik na ito na si
This diploma makes known that*

Rodrigo Sarmiento Jamisola Jr.

*ay nakatupad sa itinakdang kurso at nakasult nang maluwatati.
has faithfully complied with the prescribed course of study with diligence*

Ipinmaalam samakatuwid na kami, sa paggamit ng kapangyarihang kaloob ng Komisyon ng Lalong Mataas
be it therefore declared that by virtue of the authority granted to us by the Commission on Higher
na Edukasyon, Republika ng Pilipinas ay nagkaloob sa naturang mag-aaral ng titulong
Education, Republic of the Philippines, we confer upon the said student the degree of

Doktor ng Pilosopiya sa Inhinyeriyang Elektroniks at Komunikasyon
Doctor of Philosophy in Electronics and Communications Engineering

At aming inihahayag na siya'y mag-aangkin ng lahat ng karapatan at pribilehiyong nauukol dito.
And we declare that he/she is entitled to enjoy all the rights and privileges pertaining thereto.

Bilang katunayan ay taglay nito ang tatak ng aming Pamantasan at ang mga lagda namin.
In testimony whereof, we have caused to be affixed hereto the seal of our University and our signatures.
Inilagda sa Maynila, Pilipinas ngayong ika - 19 ng Disyembre
Done at Manila, Philippines on **DECEMBER 19**
taon ng ating Panginoon, dalawang libo at siyam.
in the year of our Lord, two thousand and nine.



www.dlsu.edu.ph

Julius B. Maridable
Dr. Julius B. Maridable

Vice Chancellor for Academics and Research

Armin A. Luistro
Br. Armin A. Luistro FSC
President and Chancellor

OFFICIAL TRANSCRIPT OF RECORD
(Revised March 1986)

UNIVERSITY OF THE PHILIPPINES, DILIMAN
OFFICE OF THE UNIVERSITY REGISTRAR

Name RODRIGO SARMIENTO JAMISOLA, JR.

Student No. 88-37932

COLLEGIATE RECORD				Course Number		DESCRIPTIVE TITLE OF THE COURSE		Final	Reexamination/Completion	Credits
				Summer, 1990		Physics 73		1.75		4
				1st Semester, 1990-1991		Nat Science II		1		3
				1st Semester, 1991-1992		Foundations of Natural Science II		1		3
						Introduction to Industrial Engineering		1.5		3
						Elements of Materials Science		1.5		3
						Dynamics of Rigid Bodies		1.75		3
						Mechanics of Deformable Bodies I		2		3
						Thermodynamics		2.75		3
				1st Semester, 1991-1992		Mechanics of Fluids		1		3
						Machine Elements I		1.75		3
						Heat Transfer		1.75		3
						Mechanical Measurement and Instrumentation		1.75		3
						Computer Programming		2.5		3
						Elementary Physics III Laboratory		1.75		1
				2nd Semester, 1991-1992		Principles of Geology		1.75		3
						Manufacturing Processes		2.25		4
						Machine Elements II		1.5		3
						Combustion Engines		1.75		3
						Mathematical Methods in Engineering		2.25		3
						Machine Design I		4	3	3
				1st Semester, 1992-1993		The Life and Works of Jose Rizal		1		3
						Mechanical Vibrations		1.75		2
						Machine Design II		2.75		3
						Power Plant Engineering I		2.25		3
						Essentials of Electrical Engineering I		2		4
						Fluid Machinery		3		3
				2nd Semester, 1992-1993		Engineering Economy		1		3
						Refrigeration Engineering		1		3
						Air Conditioning		1.5		3
						Machine Tool Operations		1.5		3
						Introduction to Control Engineering		2.25		3
						Power Plant Engineering II		3		2
						Physical Education 2		1.25		(2)
				1st Semester, 1993-1994		Science, Technology and Society		1.5		3
						Elementary Statistics		1.75		3

(cont'd on page 3)

Remarks

COLLEGIATE RECORD			Credits	
Course Number		DESCRIPTIVE TITLE OF THE COURSE	Final	Reexamination/Completion
1st Semester, 1983-1994		(cont'n) / Mechanical Engineering Laboratory Machine Design III Essentials of Electrical Engineering II	1.5 / 2.25 / 2.5 / 1.5 /	3 / 2 / 3 / (2) /
M E 174 M E 155 E E 7 Physical Education 2		NO ENTRY FOLLOWS		

Cleared - October 3, 1994 /

Remarks



THE NATIONAL UNIVERSITY of SINGAPORE

TRANSCRIPT OF ACADEMIC RECORD

10 Kent Ridge Crescent • Singapore 119260 • Telephone 775 6666 • Facsimile 778 6371

NAME: JAMISOLA RODRIGO JR SARMIENTO (MR) DATE OF BIRTH: 16.11.1971
DATE OF ADMISSION: 17.01.1997 FACULTY: ENGINEERING/DEPT OF MECH ENGG
DATE OF GRADUATION: ----- DEGREE REGISTERED: MASTER OF ENGINEERING (by research)
DATE OF MAX. CANDIDATURE: 30.08.2000
NUS RESEARCH SCHOLARSHIP/STUDENTSHIP: From 06.09.1997 to 09.08.1999

Session	Courses of Study	Grade
Semester 1 1997/1998	ME5402 ADVANCED ROBOTICS	C+
Semester 2 1997/1998	ME5404 INTRODUCTION TO NEURAL NETWORKS	D+

THESIS TITLE: Full dynamics identification and control of Puma 560 and mitsubitshi PA-10 robots

STAGE OF STUDY: Submitted thesis for examination on 03.08.2000. Amending thesis for final submission.

Remarks:

1. In addition to the thesis, M.Eng. and Ph.D. candidates in the Faculty of Engineering (except those in Dept of Chemical & Environmental Engineering) admitted with effect from July 1992 are required to read and pass courses as prescribed by the Faculty unless they have been granted exemptions. For candidates in Dept of Chemical & Environmental Engineering, the coursework requirement applies to those who are admitted with effect from July 1994. Candidates admitted with effect from July 1999 must obtain a minimum average grade as given below:

- M.Eng. : B- for two courses from among the prescribed courses
- Ph.D. : B for four courses from among the prescribed courses

2. The grading system is as follows:

Prior to 1998/1999	1998/1999	With effect from 1999/2000	Prior to Sem 2, 1998/1999 (For English Course only)
A+ or A : Excellent	A+ or A : Excellent	A+	HS : Highly Satisfactory
B+ or B : Very Good	B+ or B : Very Good	A	S : Satisfactory
C+ or C : Good	C+ : Good	A-	US : Unsatisfactory
D+ or D : Pass	C : Satisfactory	B+	
F : Fail	D+ or D : Pass	B	
	F : Fail	B-	
		C+	
		C	
		D+) Probationary Grade	
		D)	
		F : Fail	

Note : Effective from academic year 1994/1995, Distinction awarded for outstanding merit is indicated by the symbol (*) in addition to the grade.

3. No grade is given for thesis.

----- END -----

DATE: 20.04.2001




for REGISTRAR
THE NATIONAL UNIVERSITY of SINGAPORE

STUDENT NAME: Rodrigo Sarmiento Jamisola
ID NUMBER : 650-20-7450
BIRTHDATE : 11/16/71

P

DATE AND TIME PRINTED: 01/20/06 10:59 A
PAGE: 01

Colorado State University
Office of Records and Registration
Ft. Collins, Colorado 80523-8021
(970-491-7148)

OFFICIAL TRANSCRIPT

When Printed on Green Background

See back for details on
grading and validation

STUDENT LEVEL: Graduate

-----PREVIOUS INSTITUTIONS-----

National University of Singapore

TOTAL TRANSFER CREDIT ACCEPTED: 30.00

-----COURSE INFORMATION-----

Fall Sem 2001 PHD - Level 1

EE	580	Robot Motion Planning	3.00	A
EE	799	V Dissertation	12.00	S
TERM CREDITS PASSED			: 15.00	
TERM GRADE POINTS			: 12.00	TERM GPA : 4.00

Spring Sem 2002 PHD - Level 2

EE	799	V Dissertation	8.00	S
M	561	Numerical Analysis I	4.00	A+
ME	514	Manufacturing&Robotic Systems	3.00	A-
TERM CREDITS PASSED			: 15.00	
TERM GRADE POINTS			: 27.01	TERM GPA : 3.85

Summer Ses 2002 PHD - Level 2

EE	799	V Dissertation	1.00	S
TERM CREDITS PASSED			: 1.00	
TERM GRADE POINTS			: .00	TERM GPA : .00

Fall Sem 2002 PHD - Level 2

EE	799	V Dissertation	1.00	S
M	651	Numerical Analysis II	4.00	A
TERM CREDITS PASSED			: 5.00	
TERM GRADE POINTS			: 16.00	TERM GPA : 4.00

Spring Sem 2003 PHD - Level 2

EE	520	Optimization-Control & Comm	3.00	B-
EE	666	Topics in Robotics	3.00	A
EE	799	V Dissertation	2.00	S
TERM CREDITS PASSED			: 8.00	
TERM GRADE POINTS			: 20.01	TERM GPA : 3.33

Summer Ses 2003 PHD - Level 2

CR	ON	Continuous Regstrtn-On Campus	.00	
TERM CREDITS PASSED			: .00	
TERM GRADE POINTS			: .00	TERM GPA : .00

Fall Sem 2003 PHD - Level 2

CR	CONRG	Continuous Registration	.00	
TERM CREDITS PASSED			: .00	
TERM GRADE POINTS			: .00	TERM GPA : .00

Spring Sem 2004 PHD - Level 2

CR	CONRG	Continuous Registration	.00	
TERM CREDITS PASSED			: .00	
TERM GRADE POINTS			: .00	TERM GPA : .00

Fall Sem 2004 PHD - Level 2

CR	CONRG	Continuous Registration	.00	
TERM CREDITS PASSED			: .00	
TERM GRADE POINTS			: .00	TERM GPA : .00

-----END OF COLUMN-----

Spring Sem 2005 PHD - Level 2

CR	CONRG	Continuous Registration	.00	
TERM CREDITS PASSED			: .00	
TERM GRADE POINTS			: .00	TERM GPA : .00

Fall Sem 2005 PHD - Level 2

CR	CONRG	Continuous Registration	.00	
TERM CREDITS PASSED			: .00	
TERM GRADE POINTS			: .00	TERM GPA : .00

Spring Sem 2006 PHD - Level 2

CR	CONRG	Continuous Registration	.00	
TERM CREDITS PASSED			: .00	
TERM GRADE POINTS			: .00	TERM GPA : .00

-----SUMMARY-----

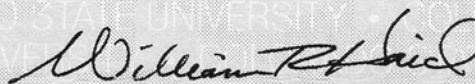
CREDITS PASSED	: 44.00	GPA CREDITS	: 20.00
GRADE POINTS	: 75.02	* GRADE POINT AVERAGE:	3.75

-----END OF STUDENT LEVEL-----

-----END OF TRANSCRIPT-----

RAISED SEAL NOT REQUIRED

This official transcript is printed on secured paper and does not require a raised seal. The word COPY will appear when photocopied. The name of the University appears in the background.



University Registrar



OFFICE OF THE UNIVERSITY REGISTRAR
Transcript of Records

PERSONAL DATA			
Student Name (Last, First, Middle)	JAMISOLA, RODRIGO JR, SARMIENTO		
ID Number	10880445	Date of Birth	16 November 1971
Citizenship	Filipino	Gender	Male
Place of Birth	Mabini, Bohol, Philippines		

EDUCATIONAL DATA			
Degree	Doctor of Philosophy in Electronics and Communications Engineering		
Admission Credentials	Transcript of Records (Masters)		
Date of Admission	10 September 2008	Date of Graduation	19 December 2009
Cumulative GPA	4.000 out of 4.000	Special Order No. (C)	Exempted
Academic Honors	Not applicable		

LAST SCHOOL ATTENDED	
Graduate Studies	Master of Science in Electrical Engineering (2006) Colorado State University United States
NOTHING FOLLOWS	

Academic Year/ Term	Course Code	Course Title	Grade	Unit/s
2008-2009, Term 2	ENG500M	ADVANCED TECHNICAL READING AND WRITING 1 & 2	EXEMPTED	(-)
	ECE661D	FUZZY LOGIC (FOR PHD STUDENTS)	4.0	3
	ECE820D	SEMINAR IN PH.D. - ECE	4.0	3
	ECE811D	SPECIAL TOPICS IN COMMUNICATION	4.0	3
2008-2009, Term 3	COE572D	ADVANCED ENERGY SYSTEMS MODELLING (FOR PHD STUDENTS)	4.0	3
	ECE620D	NEURAL NETWORKS	4.0	3
	COE559D	PHILOSOPHY OF TECHNOLOGY	4.0	3
		DISSERTATION: "Identifying Mass, Center of Mass, and Moment of Inertia Through Natural Oscillations for Full-Dynamics Control of Robot Manipulators"		12
		Total Units Earned		30.0
		Non-Academic/Remedial Units		(0.0)
NOTHING FOLLOWS				

Remarks : For Evaluation Purposes - Not Valid for School Transfer	
This document is considered official only if without erasures/alterations and affixed with original signature in ink, the University seal, barcode and documentary stamp (at the back).	I hereby certify that the foregoing entries are true and correct and that the official records substantiating the same are kept in the electronic and physical files of the school.